UNIVERSITA' DI PISA

Facoltá di Scienze Matematiche, Fisiche e Naturali

Corso di Laurea Magistrale in Fisica
Curriculum di Astronomia e Astrofisica

Titolo Tesi

Toward Understanding the B[e] Phenomenon:
The curious case of IRAS 17449+2320

Candidato
Federico Sestito

Relatore
Professor Steven Neil Shore

Anno Accademico 2015/16

Abstract

The existence of classical Be stars, stars that show emission lines due to a disk-like structure around the central object, has been recognize for more than one century ([88]). In contrast the history of the B[e] stars is much shorter. Conti ([1]) suggested calling B-type stars that show low ionization forbidden emission lines as B[e]. Nowadays, we know that B[e] stars are an inhomogeneous group of objects so it is uncorrect to speak about a class of stars but it is better to talk about the B[e] phenomenon.

The B[e] phenomenon appears in early-type emission lines stars with low-excitation lines, forbidden lines, and hot dust detected by an IR excess. The phenomenon is important because appears in very different evolutionary stages of stars (in the intermediate mass pre-main sequence stars HAeB[e], in the main sequence stars MSB[e], in the evolved high-mass stars sgB[e], evolved low-mass stars cPNB[e], symbiotic stars symB[e] etc. [88]). Studying this phenomenon we can better understand the physical mechanisms that appear during the life of a star and correlations between dynamical mechanisms (wind, rotation, eruptions, non radial pulsations, binarity etc.) and evolution.

It is important that B[e] objects harbor dust in a circumstellar disk and may be responsible for at least few percent of the Galactic circumstellar dust. Dust forming B[e] stars exist in the lower metallicity environments of LMC and SMC so it is reasonable to suggest that they might have been important dust producers in the earlier Universe.

It is difficult to study these stars beacause they are embedded in a geometrically and optically thick circumstellar envelope, but, we can try to infer the physical properties by studying the interaction between the star and its environment.

The object of my analysis is IRAS $17449 + 2320$ (also called BD $+23$ 3183, 2MASS J17470327 $+ 2319454$ and StHA 145), a V= 10 mag B[e] object situated in the Hercules constellation at a distance of 700 pc from the Sun. IRAS $17449 + 2320$ is catalogued as a A0V star and a possible FS CMa object ([52]), a subclass of the B[e] phenomenon. There are observational and physical criteria for the identification of a FS CMa star ([51]).

- Observational criteria:

  - Emission line spectra contain H lines stronger than in Be, HAeBe, and normal supergiants; Fe II and [O I]; sometimes [Fe II] and weak [O III] lines.
  - Large IR excess that peaks at $10 - 30$ μm and sharply decreases longward.
  - Location outside of star forming regions.
  - When presents, a secondary companion (i) is typically fainter and cooler (if it is a normal star) than the primary or (ii) is degenerate.

- Physical criteria:

  - T_{eff} of the hot star/companion of about $9000 - 30000$ K (O9 - A2 type stars).
  - Luminosity of the hot star/companion $\log{(L/L_{\odot})} \approx 2.5 - 4.5$
  - $\Delta V_{pri-sec} \geq 2$ mag

This is an observational thesis, so a special focus is on the data analysis. I will explain how to reduce spectral data, both slit and échelle, with IRAF software, then I will analyze the spectra taken from the Ondřejov Observatory, the Observatorio Astronomico Nacional San Pedro Martir , McDonald Observatory and the Canada France Hawaii Telescope. In particular, I will describe the line profile variations, expecially for the Balmer lines. Then, theoretical chapters follow, trying to describe the phenomenology behind the physical mechanisms inferred by the spectroscopic studies.

The Balmer lines have broad wings in absorption wide 3600 km s^{-1} (FWZI) but the core is composite by emission and absorption features. The variation of Balmer lines is only in the core and in the range of velocity of $[-300, 300]$ km s^{-1}, this means that the dynamical phenomena that are affecting these lines are playing at a distance lesser than an AU. The wings of Fe II, Na I D, O I and Ca II are broad as the range of velocity where the dynamical phenomena are affecting the Balmer lines. This can suggest that these lines are forming in the

same region of the perturbations. Instead the width of [O I] emission lines suggest that [O I] are forming in a wider low density region and it is possible to use the doppler shift of these lines as an indicator of the radial velocity of the system that is RV$= -16 \pm 2$ km s^{-1}. I found in the Balmer lines, the presence of composite absorption features moving from the blue to the red side with a time scale of few days, changing their velocity of 200 km s^{-1}. This behaviour be explained by the presence of coherent but temporary structures that are orbiting around the star at about 0.2 AU where the radiation has a temperature of about ≈ 2900 K. The origin of this structure is not known, but some scenarios are the presence of global one-armed (i.e. azimuthal wave number $m = 1$) oscillations in the equatorial discs ([33], [57], [58]) and the evaporation of a planet forming a multi-cometary tail ([42].

Line variations are found on a range of timescales: few days for Balmer lines, and month or years for the other lines. The presence of He I lines suggests that the star is earlier than thought by Miroshnichenko but not earlier than a B8V. The wings of Balmer lines compared with the ones obtained rotating the spectrum of Vega gives an estimation of the projected rotational velocity. The best match is assuming $v_{eq} \sin(\theta) \approx 200$ km s^{-1}, hence the star is a fast rotator.

FS CMa objects sometimes show binarity, in this case there is no clear evidence of a companion but binarity cannot be ruled out since a brown dwarf or a white dwarf do not produce detectable spectra.

"Ma allora," ardii
commentare,"siete ancora lontano
dalla soluzione"
"Ci sono vicinissimo," disse
Guglielmo, "ma non so a quale."
"Quindi non avete una sola
risposta alle vostre domande?"
"Adso, se l'avessi insegnerei
teologia a Parigi."
"A Parigi hanno sempre la
risposta vera?"
"Mai," disse Guglielmo, "ma sono
molto sicuri dei loro errori."
"E voi," dissi con infantile
impertinenza, "non commettete
mai errori?"
"Spesso," rispose. "Ma invece di
concepirne uno solo ne immagino
molti, cosí non divento schiavo di
nessuno."

Il nome della rosa

We choose to go to the moon. We
choose to go to the moon...we
choose to go to the moon in this
decade and do the other things,
not because they are easy, but
because they are hard, because
that goal will serve to organize
and measure the best of our
energies and skills, because that
challenge is one that we are
willing to accept, one we are
unwilling to postpone, and one
which we intend to win, and the
others, too.

[J.F.K.]

You raise up your head
and you ask, "Is this where it is?"
and somebody points to you and
says "It's his"
and you say, "What's mine?"
and somebody else says,
"Where what is?"
and you say, "Oh my God
am I here all alone?"
Because something is happening
here but you don't know what it
is, do you, Mister Jones?

[Bob Dylan]

Contents

List of Figures

List of Tables

Chapter 1

Introduction to B[e] Phenomenon

Stars exhibiting an excess of IR radiation above their expected photospheric level were first detected in 1970s, most being associated with nebulosities and initially thought to be protostars. Geisel ([19]) found a correlation between the low excitation Fe II line emission and IR excess. This was interpreted as a consequence of a large-scale mass loss that leads to the formation of dust in the circumstellar (CS) environment. It was realized that about 30% of the 70 objects reported by Geisel are indeed young stars and about 40% are evolved objects like supergiants (e.g P Cyg, μ Cep), planetary nebulae (PNe, e.g. NGC 7027, NGC 6572) and symbiotic stars (e.g. R Aqr). The remaining 30% comprised classical Be stars with gaseous-only envelopes but there remained six anomalous objects (MWC 17, FS CMa, RY Sct, MWC 342, MWC 349 and MWC 645), which years later would included in the group of peculiar Be stars, now known as B[e] stars ([3]).

Both early- and late-type emission-line stars with large IR excesses (Herbig Ae/Be [HAeBe] and T Tauri stars, respectively) located in star-forming regions are pre-main sequence stars of different initial masses. *IRAS* (InfraRed Astronomical Satellite) discovered in 1983 young main-sequence Vega-Type stars with dusty debris disks ([7]) and proto-planetary nebulae (PPNe) at an intermediate evolutionary stage between AGB and PN stage. Both of these objects were found to inherit CS dust from their precursors. Even earlier, it was shown that CS dust can be formed in the chromospheres and winds of cool stars. Also, studies of hot luminous dusty objects, i.e. Wolf-Rayet (WR) stars and Luminous Blue Variable (LBV), resulted in understanding that CS dust can be formed even in much harsher, but special conditions (e.g. high matter density due to strong mass loss and or clumping).

This progress in understanding dust formation and evolution around various objects became possible due to long-term studies of groups of objects. The picture for the B[e] stars has progressed slowly. Although in literature it is possible to find the nomenclature of B[e] star, it is better to speak about stars that show the *B[e] phenomenon* or *B[e] objects*. A star or a system can be included in the B[e] group if it is an emission-line B-type star with large infrared excesses due to hot CS dust and optical spectrum that contain forbidden lines (e.g. [O I], [Fe II], [N II] etc.) and permitted lines like Balmer and Fe II lines, so this group is an heterogeneous ensemble of objects. This means that the mechanism for the CS dust formation is not unique. Three main mechanisms have been discussed: direct ejection from a massive Be or Oe star, the interaction between an OB star with a late companion or the formation of PNe as a single event. An observational feature is that B[e] objects are often optically reddened, $E(B-V) \geq 1$mag, but it is not clear how much is the contribution of CS dust irelative to the interstellar extinction. Photospheric lines are not detected in the B[e] spectra so their luminosity and the spectral types are uncertain. Hence, the location in the Hertzsprung-Russel diagram (HRD) and the evolutionary phase cannot be well constrained.

Lamers et al. ([41]) suggested a classification based on the evolutionary phase of B[e] stars by recognizing five subgroups:

1. pre-main-sequence HAeB[e] stars

2. symbiotic binaries symbB[e]

3. compact PPNe/PNe cPNB[e]

4. supergiant sgB[e]

5. unclassified unclB[e]

The simililar conditions of these five subgroups regard their gaseous and dusty envelopes:

a) The strong Balmer lines imply very large emission measures (EM) of the singly ionized gas above the stellar continuum forming region (for a sgB[e] with Hα luminosity of 10^{37-38} erg s^{-1}, the EM are of order of 10^{62-63} cm^{-3}).

b) CS gas temperature of $\sim 10^4$ K to account for the presence of low-excitation permitted emission lines of both neutral and ionized species, e.g. Fe II.

c) Large geometrical extension of the CS material that provides a sufficient amount of low density gas to account for the presence of forbidden emission lines (e.g. [Fe II], [O I]) and a sufficient column density in its outermost regions to account for the presence of CS dust.

d) According to Bjorkman ([9]), IR excesses from cool dust ($T \approx 500 - 1000$ K) indicate a circumstellar density of $\rho \geq 10^{-18}$ g cm^{-3} at a distance where the dust temperature can equilibriate ($d \geq 500 - 1000$ R$_\star$).

Lamers also pointed out that the CS envelope geometry is disk-like, which naturally leads to the conditions for a high density of the CS matter and a shielding of the CS dust from the ionizing radiation field.

Stars showing the B[e] phenomenon form a distinct group of objects in the (J-H)- (H-K) diagram (Zickgraf [88]) as shown in figure 1.1. Figure 1.1 shows the comparison between B[e] objects from the Galaxy (asterisks), LMC (squares) and SMC (triangles), the stars with normal colours, stars with IR excess due to free-free emission, and stars with late-type companion. MC's objects are important because they are formed in a metal-poor environment, and can reproduce the earlier star formation in the Universe. Infrared excess is too large to only originate from the free-free and free-bound emissions of a gaseous envelope and is probably due to the presence of optically thick dust in the circumstellar environment of this star. Hot dust is the defining characteristic of a B[e] object. Linear polarization measurements showed that B[e] objects are characterized by non-spherical distribution of circumstellar material (or scattering particles). There could be two main scattering mechanisms, one by dust grains and one by Rayleigh scattering.
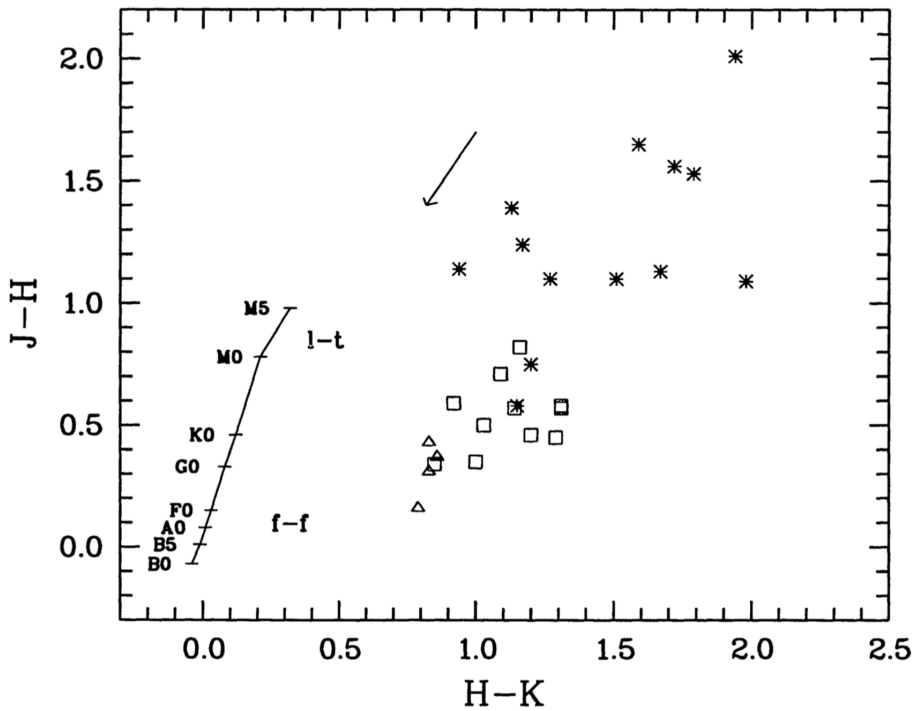
Figure 1.1: (J-H)-(H-K) diagram for B[e] objects: the Galactic B[e] objects are denoted with asterisks, the ones from LMC with squares and the ones from SMC with triangles. The location of stars with normal colours is indicated by the solid line. f-f denotes the location of stars with IR excess due to free-free emission from stellar winds. l-t, instead, the area occupied by objects with late-type companions. The arrow gives the reddening line for $A_V = 3$. Plot from Zickgraf [88].

Miroshnichenko ([51]) investigated the unclB[e]. He found that some of that resemble similar characteristics, hence he created the nomenclature for this new subclass: the FS CMa objects. The observational and physical criteria for the identification of a FS CMa star are ([51]).

- Observational criteria:

  - Emission line spectra contain H lines stronger than in Be, HAeBe, and normal supergiant stars; Fe II and [O I] lines; sometimes [Fe II] and weak [O III] lines.
  - Large IR excess that peaks at $10 - 30$ μm and sharply decreases longward.
  - Location outside of star forming regions.
  - When presents, a secondary companion (i) is typically fainter and cooler (if it is a normal star) than the primary or (ii) is degenerate.

- Physical criteria:

  - T_{eff} of the hot star/companion of about $9000 - 30000$ K (O9 - A2 type stars).
  - Luminosity of the hot star/companion $\log (L/L_\odot) \approx 2.5 - 4.5$
  - $\Delta V_{pri-sec} \geq 2$ mag

The object of my analysis is IRAS $17449 + 2320$. In other catalogues, the star is called BD +23 3183, 2MASS J17470327 + 2319454 and StHA 145. Miroshnichenko catalogued it as a $V = 10$ A0V star and a possible FS CMa object situated in the direction of Hercules constellation at about 0.7 kpc from the Sun ([52]). The coordinates (J2000) of the object are RA= $17^h 47^m 03.2769^s$ and DEC= $+23°19'45.355''$ accessible from the northern hemisphere. The Galactic coordinates (J2000) of the object are the longitude 47.9299 and the latitude +24.0258. IRAS $17449 + 2320$ is not in the disk plane and so in a region where the star formation is not present. Hence the object is not young and not in pre main sequence. This object is interesting because represents the link between low mass stars and massive stars and also between evolved (sgB[e] etc.) and pre-main-sequence (HAeB[e]) stars that show B[e] phenomenon. Understanding B[e] phenomenon in intermediate mass stars remains a challenge and open issue in astrophysics.

Chapter 2

Observatories and Spectrographs

In this chapter, I describe the characteristics of the telescopes and spectrographs used for acquiring the data of the object IRAS $17449 + 2320$, a B[e] object. The study of Be and B[e] objects involves a large spectroscopic, photometric but also interferometric and polarimetric survey all over the World. For the object of my thesis, the spectroscopic data were acquired from four different observatories:

- the 2 m Coudé telescope at the Ondřejov Observatory. The slit spectrograph, based on a grating, covers for our purposes a spectral range from 6250Å to 6750Å at a resolving power of $R \approx 12500$.

- the 2.7 m Coudé telescope at the McDonald Observatory. The échelle spectrograph covers a spectral range from 3400Å to 1μm at a resolving power of $R \approx 60000$.

- the 2.1 m Coudé telescope at the Observatorio Astronomico Nacional San Pedro Martir (SPM). The échelle spectrograph covers a spectral range from 3500Å to 7300Å at a resolving power of $R \approx 18000$.

- the 3.6 m Canada France Hawaii Telescope (CFHT) in Mauna Kea, Hawaii. The échelle spectrograph covers a spectral range from 3700Å to 10500Å at a resolving power of $R \approx 80000$.

2.1 The Ondřejov Observatory

The telescope, also called Perek telescope, is a 2 m telescope and it is used as Coudé and the focus is equipped with a slit spectrograph. The telescope is mainly used for Be stars spectroscopy, detection of binary systems, search for rapid and long term variations in spectra, search for possible relationship between non-radial pulsation of stars and their membership in the binaries with eccentric orbits etc.

The Coudé spectrograph is a standard device equipped with a slit and a second order grating ([77]). The resolving power of the spectrograph is R$\approx$ 12500, this means that at Hα ($\lambda = 6563$ AA), the resolution is $\Delta\lambda = 0.525$ AA or $\Delta v = 23.98$ km s^{-1}. When combined with the CCD, the resolving power doubles and so the resolution. The camera used for the acquisition of the spectra is a Schmidt camera with a focal length of $f = 700$ mm. To obtain the dispersion relation, the spectrograph is equipped with a ThAr lamp. For the purposes of this thesis, the spectrograph was used in the spectral range from 6250Å to 6750Å.

2.2 The McDonald Observatory

The Observatory has many telescope of different size for a wide range of instrumentation for imaging and spectroscopy. In particular, the one used for my thesis is the 2.7 m telescope Harlan J. Smith Telescope ([83]).

The spectrograph, *2dcoudé*, is a cross-dispersed échelle with a resolving power of R$\approx$ 60000, this means that at Hα ($\lambda = 6563$ Å), the resolution is $\Delta\lambda = 0.109$ Å or $\Delta v = 5$ km s^{-1}. When combined with the CCD, the resolving power doubles and so the resolution. The bandwidth is $3400 \div 10900$ Å. Because it is a cross-dispersed échelle spectrograph, the spectrum of beam is split into many orders, each of them has different range in wavelength from the others. In this case, the 2dcoudé spectrograph produces up to 62 orders.

2.3   San Pedro Martir

The San Pedro Martir Observatory has three telescopes with three different diameters. The one used for this thesis has a diameter of $2.1m$ and has a Ritchey-Chrétien design.

The échelle spectrograph at the SPM has a resolving power of R$\approx$ 18000, this means that at Hα ($\lambda = 6563$ Å), the resolution is $\Delta\lambda = 0.365$ Å or $\Delta v = 16.7$ km s^{-1}. When combined with the CCD, the resolving power doubles and so the resolution. The spectrograph covers from 3500Å to 7300Å. This échelle is also called ESPRESSO (for échelle SPectrograph form REosc for the Sierra San pedro martir Observatory).

The main échelle grating has a surface of 254mm $\times$ 128mm and has 79 lines/mm. The light beam enters in the decker and then into the slit. After, the beam is collimated and then hits the échelle. Next, a cross disperser separates the orders. Finally, each order passes through a corrector and reaches the CCD.

2.4   CFHT

The telescope of the Mauna Kea Observatory used for this thesis is the Canada-France-Hawaii Telescope (CFHT). It is a 3.6 m telescope equipped with a spectrograph called ESPaDOnS, that stands for échelle SpectroPolarimetric Device for the Observation of Stars. ESPaDOnS ([16]) is a bench-mounted high-resolution échelle spectrograph (it can work as spectropolarimeter) fiber-fed from a Cassegrain module. The working range of the spectrograph is from 3700 Å to 10500 Å with three small gaps (9224 $\div$ 9234 Å, 9608 $\div$ 9636 Å and 10026 $\div$ 10074 Å). The spectrograph has a resolving power of 68000 in the object plus sky mode or 81000 in the object only mode. In the object only mode, the resolution at Hα ($\lambda = 6563$ Å) is $\Delta\lambda = 0.081$ Å or $\Delta v = 3.7$ km s^{-1}. When combined with the CCD, the resolving power doubles and so the resolution.

2.5   Pros and cons with the spectrographs

Photons are the most precious things for investigating celestial objects. Spectrographs help us dividing the photons respect the wavelength. But this help comes with a price.

In the case of the slit spectrograph at Ondřejov, the main limitation is that we must choose a small spectral range for each observation ($\approx$ 500Å). So if we want to cover all the optical, NUV and NIR, we must repeat the observations using much more time respect to échelle spectrographs.

A positive aspect of the Ondřejov telescope is the Coudé focus. This kind of configuration gives a fixed focus point making all the system very stable.

With échelle spectrographs we can cover the optical, NUV and NIR range with one exposure saving time for other observations. The light beam that reaches the spectrograph is splitted forming different orders. It can happen that two consecutive orders have an overlapping region or that between these orders there is a gap.

In the case of échelle, the orders recorded by the CCD are not straight as a slit grating case, but they are arched and the efficiency is higher in the central region of each order (phenomenon called vignetting). This means that we must trace the path of each order for the reduction of the spectra. Basically, the reduction of échelle spectra is more complicated than slit spectra.

Because the orders are close to each others, cosmic rays and hot pixels can affect more than one order.

Chapter 3

Data Reduction with IRAF

In this Chapter I will describe the reduction method for slit and echelle spectra with IRAF software (see [46], [87], [47]and [84]).

IRAF stands for Image Reduction and Analysis Facilities and it is written and developed by the NOAO (National Optical Astronomy Observatories). IRAF is a useful software for the reduction and analysis of astronomical data both photometry and spectroscopy.

In this thesis, I used IRAF for the reduction of the spectra taken from the following observatories:

- the 2 m Coudé telescope at the Ondřejov Observatory. The slit spectrograph, based on a grating, covers for our purposes a spectral range from 6250Å to 6750Å at a resolution of $R \approx 12500$.

- the 2.7 m Coudé telescope at the McDonald Observatory. The échelle spectrograph covers a spectral range from 3400Å to 1μm at a resolution of $R \approx 60000$.

- the 2.1 m Coudé telescope at the Observatorio Astronomico Nacional San Pedro Martir (SPM). The échelle spectrograph covers a spectral range from 3500Å to 7300Å at a resolution of $R \approx 18000$.

- the 3.6 m Canada France Hawaii Telescope (CFHT) in Mauna Kea, Hawaii. The échelle spectrograph covers a spectral range from 3700Å to 10500Å at a resolution of $R \approx 80000$.

3.1 Reduction of a slit spectrum

3.1.1 Trimming

The slit occupies only a part of the CCD and so we trim the correct area of the CCD to save disk space and computational time. IRAF contains a routine called *imcopy*.

3.1.2 Bias subtraction

The Bias, also called Zero-point, is the signal taken with zero exposure and with the CCD shutter closed. To remove, we need of some Bias frames, and combine them through the median operation obtaining a MasterBias. The IRAF task called *zeroc* combines through a median all the Bias producing a MasterBias as output. We set some parameters related to the type of the CCD (e.g. 700) like the readnoise (e.g. 7), the gain (e.g. 1.07) and also the operation for creating the MasterBias (e.g. the median). The median is better than the mean because it will eliminates better the possible cosmic rays. Then we subtract the MasterBias to the fits files using the *imarith* task. It is an IRAF task that requires two operands (the list of the input fits and the MasterBias), the kind of the operation (subtraction) and the output (the fits files after the subtraction).

3.1.3 Flat

The Flat lamp frames are the exposures of a uniform continuum source placed in front the spectrograph. Because each pixel has different gain, it is important to evaluate this response pixel by pixel and to do this we must create a MasterFlat combining all the flat frames with the median. This procedure also eliminates some artifacts along the light path. IRAF has a task called *imcombine* that is similar to *zeroc*, it requires as input the Flat frames and produces a MasterFlat. To prevent the numerical overflow, we normalize the MasterFlat with *imarith* task, in this case the operands are the MasterFlat and a value that is a little bit more than the maximum signal in the MasterFlat, the operation is the division and the result is the normalized MasterFlat. Finally,we again use the *imarith* task for dividing all the fits files with the normalized MasterFlat and so we get the fits files corrected to the Flat.

3.1.4   Cosmic Rays and decay products removal

Because we are immersed ambient in a cosmic ray (cosmics), they affect the spectra. Other than cosmics, we can find in the spectra the products from the natural environmental radioactivity. Usually a cosmic ray, when hits the CCD, affects a single pixel and are easy to remove. But since the hit rate varies linearly with time , this could be a problem for long exposure. To avoid this problem, we use *dcr* code. It is developed by Wojtek Pych ([66]). The algorithm is based on a simple analysis of the histogram of the image data and does not use any modeling of the image of the object. It does not require a good signal to noise ratio in the image data. Identification of multiple pixel cosmic ray hits is achieved by running the procedure for detection and replacement iteratively. The method is very effective when applied to the images with spectroscopic data, but of course, it doesn't completely clean the cosmic rays and for this reason we must be careful if there are still some cosmics near the emission or absorption lines.

3.1.5   Tracing of the stellar spectra and Background subtraction

Using the *apall* task we can set the right upper and lower boundaries for aperture and subtract the background in the stellar spectrum. This is an interactive task to trace the spectra, find the boundaries of the aperture and the boundaries of the background, then fit the background with a polynomial function where it is possible to change the function and the order for having the best fit. It is possible to change some parameters to avoid the use of optimal extraction because this can create or modify some absorption or emission lines. The optimal extraction is simply an iterative algorithm in which the pixels have a weight, so the ones that are most important prevail in case of low signal to noise ratio.

3.1.6   Tracing of the comparison spectra

Using *apall*, we trace the comparison spectra without background subtraction just modifying some parameters and using the stellar spectrum as a template. It is better to use two comparison spectra, taken before and after each target exposure.

3.1.7   Wavelength identification and application of the dispersion relation

The wavelength dispersion relation is obtained using the IRAF task called *identify*. This is an interactive task, it requires the list of the comparison spectra and the setting of the line list parameter (in this case a ThAr lamp). The routine works with stored line lists and, manually, we identify emission lines (order of ten lines) for the first comparison spectrum, and then fit the points with a Chebyshev function with appropriate order. The task then automatically identifies other emission lines, we eliminate the bad lines are identified by the task, and the fit is performed again. When we are sure that the fit is good, we can go to the second comparison. In the second comparison spectrum it is not necessary to identify the line, just to go to a good line in the middle of the spectrum, find the center of this line, and then fit again. The *dispcor* task applies the dispersion relation to the target spectrum.

3.1.8   Julian Date and Airmass

IRAF has two tasks that calculate the Julian Date (*setjd*), write it into the header and set the airmass. The *setairmass* task requires the observatory geographic location. We have to do this because the next passage is the heliocentric correction that needs the julian date.

3.1.9   Heliocentric correction

The spectrograph is situated on an orbiting platform (the Earth) and its radial velocity depends on the direction of the target and the Earth's orbital phase, so on the Julian date. The shift due to this motion can reach magnitude of $30km/s$, which means a wavelength of 6000Å the shift is order of 0.6Å. IRAF has two tasks for the heliocentric correction, one that calculates the shift and one that applies the shift to the spectra. The first is called *rvcor* and it requires the target coordinates and the name of the observatory, it reads from the header the date and the coordinates of the observatory for calculating the shift due to the motion of the Sun respect to the Earth. The last task is called *dopcor*, it requires the input image and it applies the shift calculated before.

3.1.10   Continuum fitting

The fluxes of the spectra are not in physical units but in ADU (Analog to Digital Units) and so we must take a point as a reference value, the continuum, for the comparison of the spectra. This means that we need to find the continuum in a spectrum by fitting all the continuum intervals. In this way, we get a normalized spectrum. To do this, IRAF has an interactive task called *continuum*. We choose the intervals for the continuum, the number of bins for discretizing each interval, the type of operation (in our case the median) to apply to each bin interval and the order and the type of the fitting function (a Chebyshev) for continuum intervals. The intervals are chosen in parts of the spectrum where there are no emission or absorption lines and also avoiding the cosmic rays and the large wings of the Hα line due to the Stark effect.

3.1.11   Example of Ondřejov spectrum

After the reduction of the spectrum, it is possible to analyze and to plot the relative flux as a function of the wavelength. The figure 3.1 shows the entire spectrum of IRAS 17449 + 2320 taken on 2014/08/08 at the Ondřejov Observatory. The figure 3.2 shows a portion of the same spectrum showing the [O I] $\lambda\lambda$ 6300.304, 6363.776Å emission and Si II $\lambda\lambda$ 6347.11, 6371.37Å absorption lines. It is also two cosmic rays around 6320Å and 6380Å, but because these cosmic rays do not alter the lines it is not necessary to clean the spectrum. Figure 3.3 shows the range of the spectrum including the Hα line. As we can see, the Hα line is in emission with two peaks.

Because we are observing from the Earth, we are also observing through our atmosphere so atmospheric absorption lines (e.g. molecular oxygen, water vapour, molecular nitrogen etc.) are present in the spectra. The atmosphere has zero radial velocity respect to the telescope and hence these lines too. But with the heliocentric correction, these lines has exactly the radial velocity of the Earth respect to the Sun. Figures 3.2 and 3.3 also contain the atmospheric lines in the region around [O I] 6300.304Å and from 6450Å to 6600Å around Hα line. Other types of contamination due to the observation from the ground is the auroral emission lines, i.e. [O I] and [N II], but also the Na I D emission from street lamp. These contaminations do not appear in my spectra.
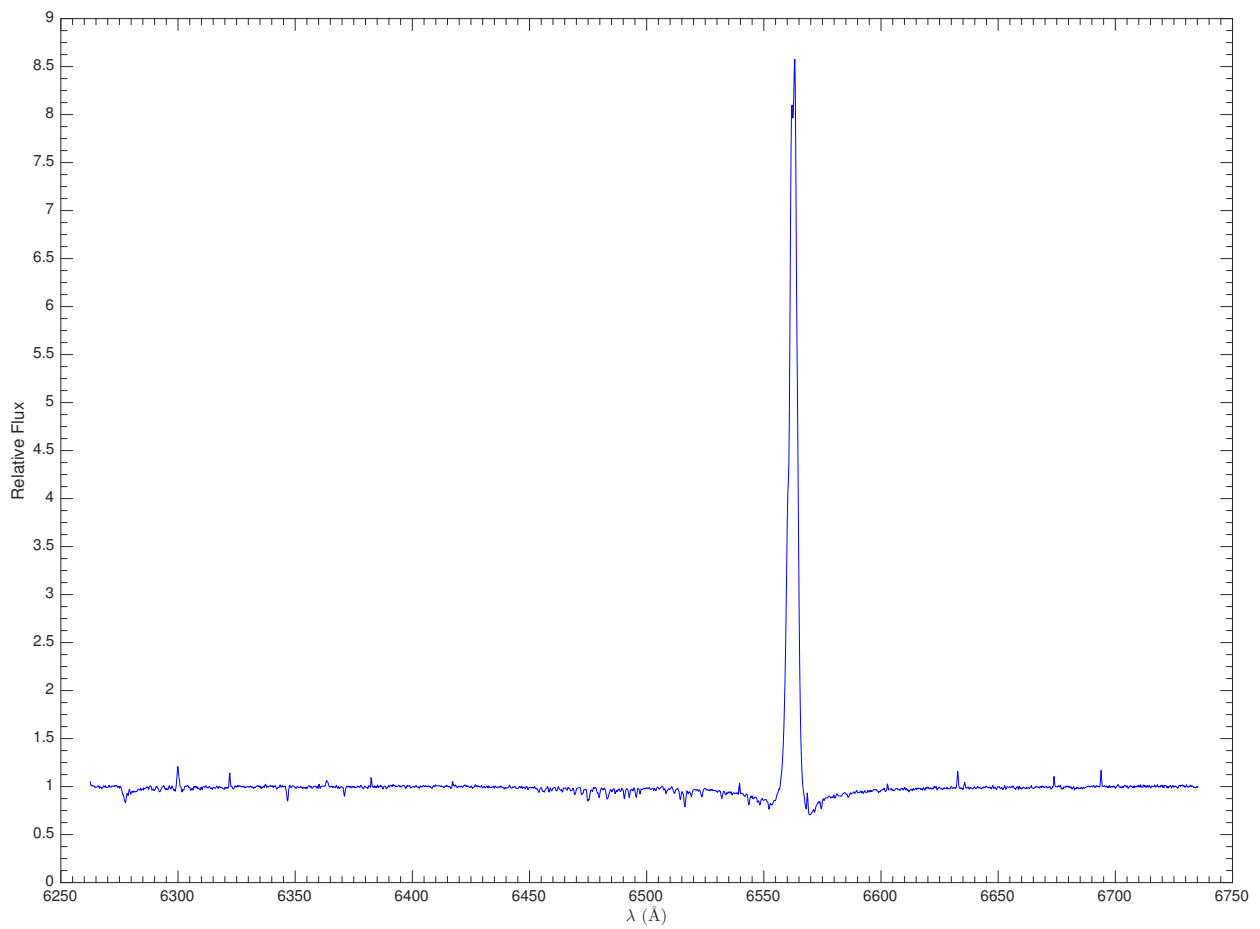
Figure 3.1: Example of the IRAS 17449 + 2320 spectrum taken at Ondřejov on 2014/08/08.
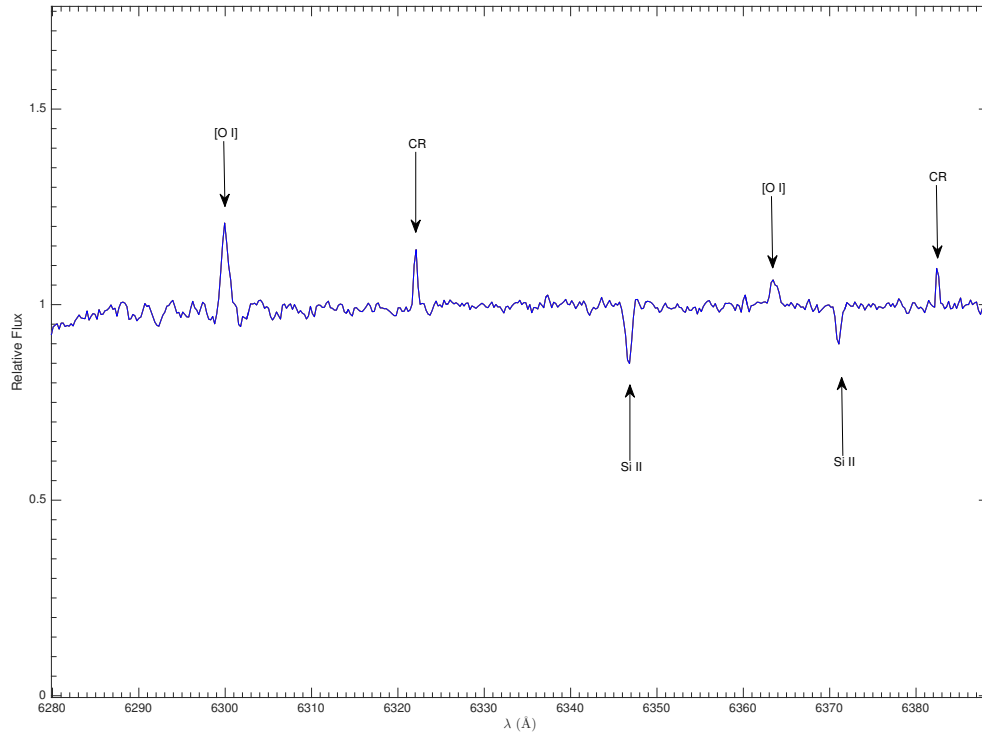
Figure 3.2: Zoom of IRAS 17449 + 2320 spectrum. It shows [O I] $\lambda\lambda$ 6300, 6364Å, Si II $\lambda\lambda$ 6347.11, 6371.37Å and two cosmic rays (CR) remained from the cleanig. Because the cosmic rays are far from the lines, they do not alter the analysis of these lines.
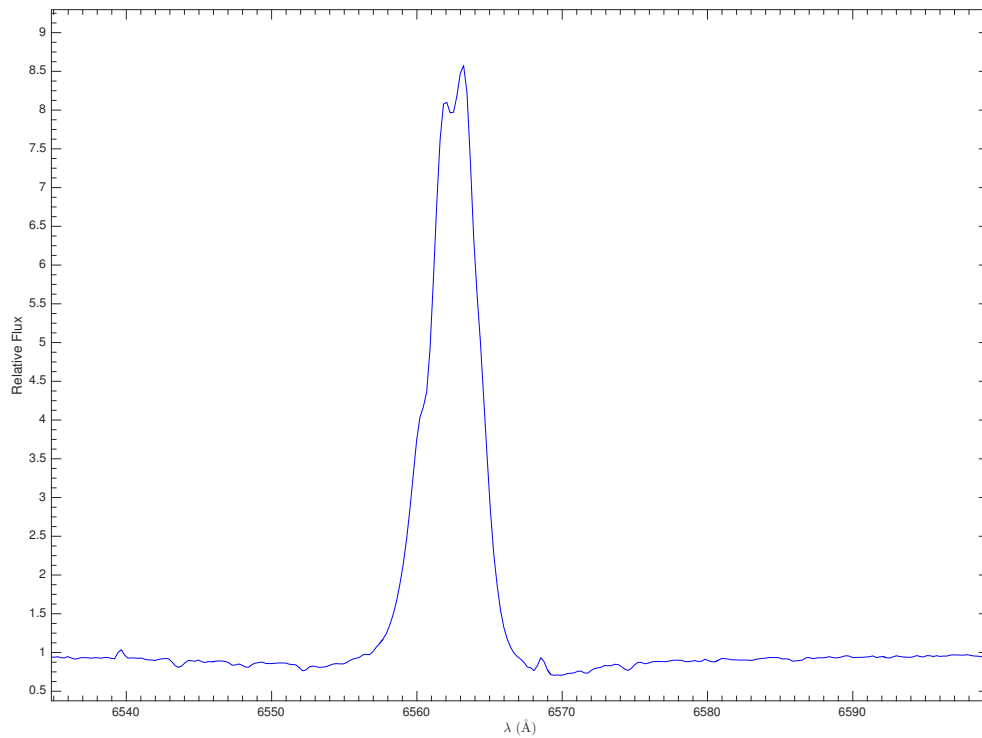
Figure 3.3: Another zoom of IRAS 17449 + 2320 spectrum in the region of the Hα line.

3.2 Échelle Reduction

Échelle spectra were taken at the McDonald Observatory during the night of 2009 September 5 and 6, at the San Pedro Martir Observatory from 2015 May 29 to June 3 and from 2016 March 22 to 27, and at the CFHT in the 2006 June 6, 2007 July 2 and 2008 July 24. The McDonald spectrum contains 62 orders in the range $[3696, 10472]$Å, the San Pedro Martir spectra 31 orders covering the range $[3575, 7323]$Å. For McDonald data, the Bias field has already been subtracted from the echelle spectrum and it has been cleaned for cosmic rays. The San Pedro Martir and CFHT spectra were reduced by the pipeline of the observatories where they are taken.

Generally, the procedure for échelle reduction is different that for single order gratings spectra because all the orders are acquired together in the same CCD image.

3.2.1 MasterFlat creation and correction

We need to create a MasterFlat field in the same fashion as before, but we can not apply the MasterFlat directly for two reasons. First, the Flat field image includes the shape of the Flat field spectrum and the echelle blaze function. Applying the Flat field directly will distort the object spectra and, in particular, the pixel values will no longer be related to the actual observed signal. This means that it would not be possible to use algorithms that depend on using the detector gain and readout noise to estimate the uncertainties of the pixels from the pixel values such those for optimally weighted extraction and cosmic ray detection. Second , flat field signal between the orders may approach zero and application of the Flat field to an object frame can greatly magnify the noise between the orders. We need to model the shape of the Flat field spectrum in each order and normalize it away, and we must know where the orders are and replace the pixels between the orders with unit response. This procedure is done by *apflatten* task. The first step is to determine and set the width, the minimum separation between the orders, and two parameters defining the flux level at which to define the edges of the slit with the following commands:

- *apedit.width* = 23

- *apfind.minsep* = 16

- *apresize.ylevel* = 0.5

- *apresize.bkg* = *no*

Then we can run the *apflatten* task. This task automatically locates the orders but, if it fails, we can modify the number of orders and also their width. The second step is to measure the positions of the orders at other lines in the image because the échelle orders are not aligned with the image columns. The tracing is done in steps of ten rows with the average of ten rows. A function fit is then applied to the positions. This procedure is interactive and we can adjust to improve the fit for each order. We then create the normalized Flat field. For each order at each row the pixel values across the aperture are summed. This creates a one dimensional spectrum for each order. We then fit a function to normalize the Flat field pixels, the function and its order should be high enough to represent the overall shape of the Flat field. The final step is to apply the normalized Flat field to the data and, to do this, we use the *imarith* task.

3.2.2 Running *doecslit*

doecslit task requires the input echellle spectrum (the *IRAS* object), the aperture reference spectrum (a standard star with strong signal), the arc spectra (we have only one ThAr lamp spectrum). *doecslit* finds the positions of the orders in the standard star and resizes the orders interactively where is necessary. Then we find, fit and subtract the background. The next step is the identification of the ThAr lines for the calculation of the dispersion relation. It is not necessary to mark and identify each line in each order. The task fits the lines and it identifies new lines. It is important to eliminate possible misidentified lines and to fit again. In the last step, *doecslit* applies the dispersion relation to the target spectrum. The output fits file is an image where each line represents an order.

3.2.3 Continuum fitting and normalization

IRAF has a special task for the normalization of the spectra, but for echelle spectra I used a different method. First, using the IRAF task called *imcopy*, I divided all the orders, creating one fits file for each. Then, using the IRAF task *wspectext* I created a two-column data file for each order: wavelength and flux. The last step is to use an interactive Python routine called *specnorm.py*. This program requires the data file and plots the spectrum, the user then selects some points of the continuum in the spectrum, and the program calculates the

median of the flux in the range around the points and does a cubic spline fit to these points. The program then divides the spectrum by the spline function and outputs a normalized spectrum. It is possible to change the range of the median operation around the points to obtain the best results for each spectrum.

3.2.4   Problems with McDonald echelle spectra

A problem appears in the reduced McDonald echelle spectra. The regions at the edges of each spectral order have an incorrect dispersion relation and so the wavelength in these regions is wrong. This problem is due to the fact that, in the original fits file, the regions at the edges of each orders are too warped relative to the other part of the order so it was not possible to find a good comprehensive dispersion relation. Hence, the lines in these regions, such as the [O I] 6300.304Å, are shifted respect the reality. A way to correct this problem is to cross-correlate the lines affected by this problem with lines not affected finding the right dispersion relation.

Chapter 4

Data Analysis

This chapter presents the main spectroscopic result for IRAS $17449 + 2320$. I discuss some important physical quantities such as the equivalent width (EW_λ), the radial velocity (RV) and to observe dynamical phenomena through the line profile variation. I begin with a description of these measurement methods for the spectra taken at the Ondřejov Observatory focusing on the [O I] $\lambda\lambda$ 6300.304, 6363.776Å lines, on the Si II $\lambda\lambda$ 6347.091, 6371.359Å lines and the Hα line. These lines are formed in different environments and their contrast gives diagnostics of the density, temperature and ionization in different regions. I then describe the measurement methods for the CFHT, SPM and Mcdonald spectra, focusing on different lines of different species and degree of ionization. Stars that show B[e] phenomenon also show line profile variabilities on both mid/long term (years) and short term (days) timescales. I will show the velocity line profile of the lines with the aim of finding if the profile changes with time, focusing on the Balmer lines from the SPM spectra. I will focus the attention on the SPM because these are the only data taken with a regularity of day for two sets of six days each.

4.1 Measurement methods

4.1.1 Ondřejov slit spectra

The only lines measurable in Ondřejov slit spectra are the [O I] $\lambda\lambda$ 6300.304, 6363.776Å, the Si II $\lambda\lambda$ 6347.11, 6371.37Å and the Hα line. The study of these lines is important because it gives information about many layers of the environment at different distances from the star. We can detect the [O I] emission lines only in a low-density medium, so it is supposed to probe the outer regions that are not significantly affected by the processes that occur close to the star. Instead, the Si II lines are in absorption, so they are formed between us and the source, in a denser layer, and provide information about the inner part of the CS environment. Last, the Hα is formed thoughout the CS medium and provide information about the entire envelope.

It is possible to use a gaussian profile for [O I] lines. Instead, for Si II absorption lines and the Hα line it is not possible to use a gaussian, but we use a polynomial of sufficiently high order that depends on the line, with the order ≥ 2 and ≤ 5. This method constructs, with a Monte Carlo, a sheaf of a selected line based on the signal to noise ratio. In this way, this method gives a more realistic guess of errors. The Jeřábková routine ([29]) that I have improved requires the range of the wavelength where we want to fit the line, the type of function and order and gives the following quantities:

- For the [O I] emission lines:

    - Equivalent width (EW_λ) with error.
    - Relative Flux (F_λ) with error.
    - Radial velocity (RV) with error.

- For the Si II absorption lines:

    - Relative Flux (F_λ) with error.
    - Radial velocity (RV) with error.

- For the Hα line:

    - Relative Flux (F_V) with error of the violet part.
    - Radial velocity (RV_V) with error of the violet part.
    - Relative Flux (F_{CD}) with error of the central depression.

– Radial velocity (RV_{CD}) with error of the central depression.

– Relative Flux (F_R) with error of the red part.

– Radial velocity (RV_R) with error of the red part.

After, with Matlab, we plot all these quantities as a function of the Modified Heliocentric Julian Date (MJD = HJD − 2450000) and also calculate the following quantities with the relative errors:

- V/R ratio for the Hα line defined as

$$\frac{V}{R} = \frac{F_V}{F_R}$$

- The ratio between the relative flux of the two [O I] lines

$$R_{[OI]} = \frac{F_{6300} - F_{cont}}{F_{6364} - F_{cont}} = \frac{F_{6300} - 1}{F_{6364} - 1}$$

- The ratio between the EW_λ of the two [O I] lines

$$\frac{EW_{6300}}{EW_{6364}}$$

The V/R ratio is important because it gives information about the anisotropies and the motion of the circumstellar media.

Although the excited state of the [O I] $\lambda\lambda$ 6300, 6364Å lines is populated by collisions, the emission is formed by spontaneous decays to the ground state. So the ratio between the two fluxes depends on the ratio of the Einstein emission coefficients:

$$R_{[OI]} = \frac{F_{6300} - F_{cont}}{F_{6364} - F_{cont}} \propto \frac{A_{6300}\nu_{6300}}{A_{6364}\nu_{6364}} \approx \frac{A_{6300}}{A_{6364}}$$

If $R_{[OI]} \approx 3$ then the lines are formed in an optically thin region, instead if $R_{[OI]} < 3$ the lines are formed in an optically thick region where also collisions can be important for the level depopulations.

With the Jan Polster's routine ([64]) it is possible to get the EW_λ of the Si II absorption lines. This interactive routine is based on the trapezium method for the integration of a function, and it requires the input spectrum, its signal to noise ratio and the extremes of the integration for the EW_λ. It is important to choose the correct limits of integration, because we want to avoid to cut the line or to add too much noise to the calculation of the EW_λ. The EW_λ depends on the limits of integration as follow:

$$EW_\lambda = \int_{-\infty}^{+\infty} \frac{F_\lambda^{cont} - F_\lambda(\lambda)}{F_\lambda^{cont}} d\lambda \approx \int_{\lambda_L}^{\lambda_R} \frac{F_\lambda^{cont} - F_\lambda(\lambda)}{F_\lambda^{cont}} d\lambda \tag{4.1}$$

This quantity represents the width of an hypothetical line which drops to an intensity of zero and has the same integrated flux deficit from the continuum as the true one and gives a quantitative measure of the strength of a spectral line. The error on the EW_λ is a function of the signal to noise ratio and follows the Vollmann and Eversberg approach ([86]).

4.1.2 McDonald, San Pedro Martir and CFHT échelle spectra

For each line, we identify the species with the help of the Multiplet Table of Astrophysical Interest ([55])and NIST([36]). This because the lines are shifted from the rest wavelength. In some case it is obvious what forms an absorption or an emission line like Hα, Hβ, Hγ, Hδ, [O I] $\lambda\lambda$ 6300, 6364Å, Si II $\lambda\lambda$ 6347, 6371Å, Na I Doublet $\lambda\lambda$ 5890, 5896Å etc. In other cases it is not obvious , but it is possible to make a guess, considering the species like Fe I, Fe II, Si II, Cr I, Cr II, Mg I, Mg II, He I, Ti I, Ti II.

For the measurement of the radial velocity RV, the equivalent width EW_λ and the signal to noise ratio S/N I have written a Matlab script called *lambda_EW_RV.m* . The script imports the data from the file containing the wavelength and the flux of an order of the echelle and requires the boundaries of a region in the spectrum where there are no lines (the continuum) for the calculation of the mean μ and the standard deviation σ of the signal. After, it calculates the signal to noise ratio $S/N = \mu/\sigma$. I assume an error for the flux equal to the standard deviation of the continuum signal, so $dF = \sigma$, the error on the wavelength is $d\lambda = (\lambda_j - \lambda_{j-1})/2$. The script requires the boundaries of a line λ_L and λ_R and it calculates the EW_λ with the trapezium method and its error as in equation 4.1. Also, it calculates a wavelength $\bar{\lambda}$ that is the mean weighted on the flux:

$$\bar{\lambda} = \langle \lambda \rangle_F = \frac{\int_{-\infty}^{\infty} F(\lambda) \cdot \lambda \cdot d\lambda}{\int_{-\infty}^{\infty} F(\lambda) \cdot d\lambda} \approx \frac{\int_{\lambda_L}^{\lambda_R} F(\lambda) \cdot \lambda \cdot d\lambda}{\int_{\lambda_L}^{\lambda_R} F(\lambda) \cdot d\lambda} \tag{4.2}$$

4.2 Spectral line list

The spectral type of B[e] objects is difficult to understand because the central object is surrounded by an optically thick envelope. Looking at all the lines, it is possible to constrain the spectral type even if the lines are weak. In this way it is possible to detect better the physical conditions of the object and quantities like the temperature, the mass and possibly the luminosity and the distance, but also if the object presents binarity. Table 4.1 reports the line transitions found in the spectra, ordered by atomic number, state of ionization and RMT multiplet, reporting also the observed wavelength where it was possible to measure it and if the line is in emission, absorption or both. Sometimes, usually for metal lines (e.g. Fe I, Ti I, Fe II, Ti II, Cr II), there are multiple transitions forming a blend. The wavelength at rest is taken from [36]. The spectra used for this investigation are from CFHT because these have the highest spectral resolution.

Species	λ (Å)	λ_{obs} (Å)	Multiplet	Profile
H I	Hα	$\star$	1	E+A
H I	Hβ	$\star$	1	E+A
H I	Hγ	$\star$	1	E+A
H I	Hδ	$\star$	1	E+A
H I	Hϵ	$\star$	1	E+A
H I	H8	$\star$	1	E+A
H I	H9	$\star$	1	E+A
H I	H10	$\star$	1	E+A
H I	H11	$\star$	1	E+A
H I	H12	$\star$	1	E+A
H I	P8	$\star$	2	E+A
H I	P9	$\star$	2	E+A
H I	P10	$\star$	2	E+A
H I	P11	$\star$	2	E+A
H I	P12	$\star$	2	E+A
H I	P13	$\star$	2	E+A
H I	P14	$\star$	2	E+A
H I	P15	$\star$	2	E+A
H I	P16	$\star$	2	E+A
He I	5015.678	5015.4	4	A
He I	5875.621	5875.3	11	A
He I	4713.146	4712.9	12	A
He I	4471.480	4471.29	14	A
He I	4026.191	4025.9	19	A
He I	6678.151	6677.8	46	A
He I	4921.931	4921.7	48	A
[O I]	6300.304	6300.0	1	E
[O I]	6363.776	6363.4	1	E
O I	7771.960	7771.5	1	A+E
O I	7774.180	7773.7	1	A+E
O I	7775.400	7775.0	1	A+E
O I	8446.250	8446	4	A+E
O I	8446.360	8446	4	A+E
O I	8446.760	8446	4	A+E
Na I	5889.951	5889.7	1	A+E
Na I	5895.923	5895.6	1	A+E
Mg I	5167.322	5167.1	2	A
Mg I	5172.684	5172.4	2	A
Mg I	5183.604	5183.3	2	A
Mg I	3829.354	3829.1	3	A
Mg I	5528.404	5528.1	9	A
Mg I	4702.980	4702.7	11	A
Mg II	4481.129	4480.9	4	A
Mg II	4384.643	4384.4	10	A
Mg II	5390.585	5390.3	10	A
Si II	3853.660	3853.4	1	A
Si II	3856.020	3855.8	1	A
Si II	3862.600	3862.4	1	A

Si II	6347.100	6346.7	2	A
Si II	6371.360	6371.0	2	A
Si II	4128.070	4127.8	3	A
Si II	4130.890	4130.7	3	A
Si II	5978.930	5978.6	4	A
Si II	5041.030	5040.7	5	A
Si II	5055.980	5055.7	5	A
Si II	5056.317	5056.0	5	A
Ca II	3933.660	3933.4	1	A+E
Ca II	3968.470	3968.2	1	A+E
Ca II	8498.02	8497.6	2	A+E
Ca II	8542.09	8541.6	2	A+E
Ca II	8662.140	8661.7	2	A+E
Ti II	4443.801	4443.5	19	A
Ti II	4395.031	4394.8	19	A
Ti II	4294.094	4293.8	20	A
Ti II	4468.492	4468.2	31	A
Ti II	4501.270	4501.0	31	A
Ti II	3913.461	3913.2	34	A
Ti II	4629.290	4629.1	38	A
Ti II	4417.714	4417.4	40	A
Ti II	4290.215	4290.0	41	A
Ti II	4300.042	4299.8	41	A
Ti II	4307.866	4307.6	41	A
Ti II	4312.860	4312.6	41	A
Ti II	4314.971	4314.7	41	A
Ti II	4533.960	4533.7	50	A
Ti II	4563.758	4563.5	50	A
Ti II	4399.765	4399.5	51	A
Cr II	4242.366	4242.1	31	A
Cr II	4261.917	4261.7	31	A
Cr II	5237.322	5237.0	43	A
Cr II	4558.644	4558.4	44	A
Cr II	4588.198	4587.9	44	A
Fe I	5167.488	5167.2	37	A
Fe I	4383.545	4383.3	41	A
Fe I	4404.750	4404.5	41	A
Fe I	4415.122	4414.9	41	A
Fe I	4271.760	4271.5	42	A
Fe I	4307.902	4307.6	42	A
Fe I	4325.762	4325.5	42	A
Fe I	4045.812	4045.6	43	A
Fe I	4063.594	4063.3	43	A
Fe II	4233.163	4232.9	27	A
Fe II	4303.168	4302.9	27	A
Fe II	4351.729	4351.5	27	A
Fe II	4416.818	4416.6	27	A
Fe II	4178.855	4178.6	28	A
Fe II	4296.567	4296.3	28	A
Fe II	4491.400	4491.1	37	A
Fe II	4515.334	4515.1	37	A
Fe II	4520.221	4519.9	37	A
Fe II	4534.166	4533.7	37	A
Fe II	4555.888	4555.6	37	A
Fe II	4629.336	4629.1	37	A
Fe II	4508.280	4508.0	38	A
Fe II	4522.628	4522.4	38	A
Fe II	4583.829	4583.6	38	A
Fe II	4923.921	4923.7	42	A+E
Fe II	5018.435	5018.1	42	A+E

Fe II	5169.028	5169.7	42	A+E
Fe II	4731.439	4731.2	43	A
Fe II	5264.801	5264.5	48	A
Fe II	5362.864	5362.6	48	A
Fe II	5197.568	5197.3	49	A
Fe II	5234.624	5234.3	49	A
Fe II	5275.997	5275.7	49	A
Fe II	5316.610	5316.3	49	A
Fe II	5534.839	5534.5	55	A

Table 4.1: Spectral line list for IRAS 17449 + 2320. It shows the name of the transitions with specie and grade of ionizations, wavelength at rest (λ), observed wavelength (λ_{obs}), multiplet and the profile of the line (E for emission, A for absorption). $\star$: the observed wavelength is not reported because of their broad profile.

In section 4.4, I will present the time series of the most intense lines of H I, O I, He I, Si II, Mg II, Fe II (multiplet 42), Ca II and Na I D.

4.3   Ondřejov slit spectra

4.3.1   Hα

The Hα line is in emission with self absorption feature forming a double peaked profile (denoted Violet V and Red R). The self absorption feature, that comes from the CS material in the direction toward us, will be referred to as the central depression. The far wings are in absorption. The Hα line has a wavelength $\lambda = 6562.817$Å and the multiplet number is 1 ($n = 2 \div 3$).

Figures 4.1, 4.2 and 4.3 show the radial velocity as a function of the MJD for the violet peak, the central depression and the red peak of the Hα line, respectively. It is clear that there is a drastic change in velocity of the violet peak and central depression (up to ≈ 70 km s^{-1}). Their RVs decrease from MJD≈ 6500, reaching the minimun around MJD≈ 6875 and then increase (again with a change of ≈ 70 km s^{-1}) with a time scale of about two weeks. In the same period the red peak varies in the same fashion but the change is lower, ≈ 15 km s^{-1}.

Figures 4.4, 4.5 and 4.6 show the relative flux at the peak as a function of the MJD for the violet peak, the central depression and the red peak of the Hα line, respectively. Figure 4.7 shows the V/R ratio as a function of the MJD. The V/R ratio appears to vary in the range of values $[0.4, 1.2]$.

There is a correlation between the different parts of the Hα line in radial velocity and flux. I have plotted the F_V versus F_C, F_R versus F_C, F_V versus F_R, RV_V versus RV_C, RV_R versus RV_C, RV_V versus RV_R respectively in figure 4.8 to figure 4.13. For each pair of observables, I calculated the Pearson product-moment correlation coefficient (Pearson's r). This is a measure of *linear* correlation between two variables x and y. r takes value between -1 and $+1$ inclusive, where $r = 0$ is no correlation, $r = -1$ is anticorrelation and $r = 1$ is correlation defined by:

$$r = \frac{\text{cov}(x,y)}{\sigma_x \sigma_y} \tag{4.3}$$

where $\text{cov}(x,y)$ is the covariance between x and y, σ_x and σ_y are the standard deviation of the two variables x and y. Tables 4.2 and 4.3 gives the Pearson's r for the flux and radial velocity of the Hα line. For the relative flux, there is a moderate linear correlation between F_r and F_v, and between F_c and F_r, and F_c and F_v are more correlated. For RV, there is a moderate correlation between RV_r and RV_v, RV_c and RV_r are more correlated, and the strongest linear correlation is between RV_c and RV_v.

	F_c	F_v	F_r
F_c	1	0.78	0.66
F_v	0.78	1	0.62
F_r	0.66	0.62	1

Table 4.2: Pearson's r between each couple of the Hα peak's flux.

	RV_c	RV_v	RV_r
RV_c	1	0.88	0.70
RV_v	0.88	1	0.48
RV_r	0.70	0.48	1

Table 4.3: Pearson's r between each couple of the Hα peak's radial velocity.
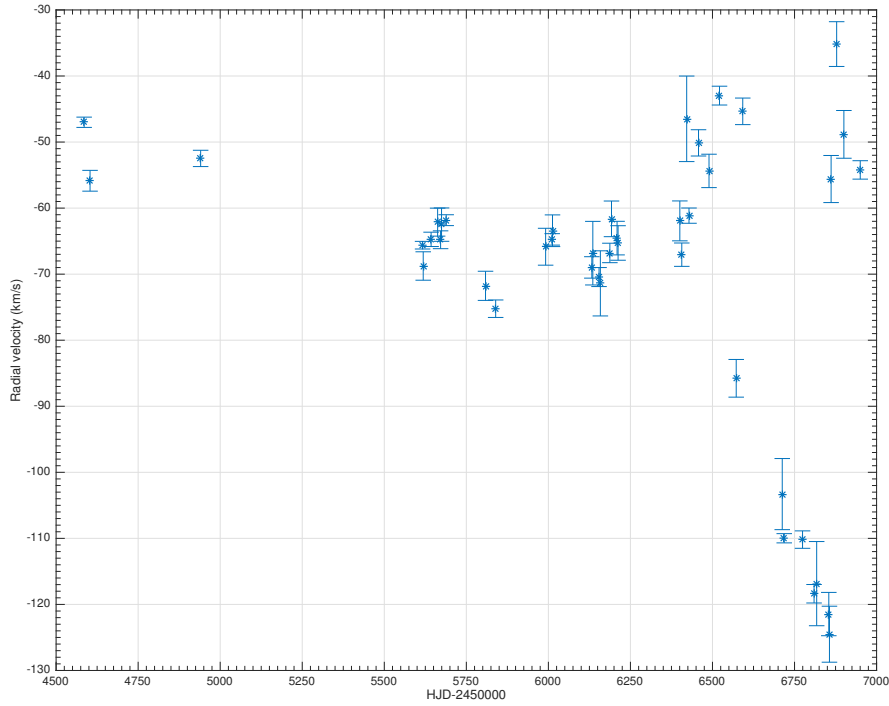
Figure 4.1: Hα V peak radial velocity.
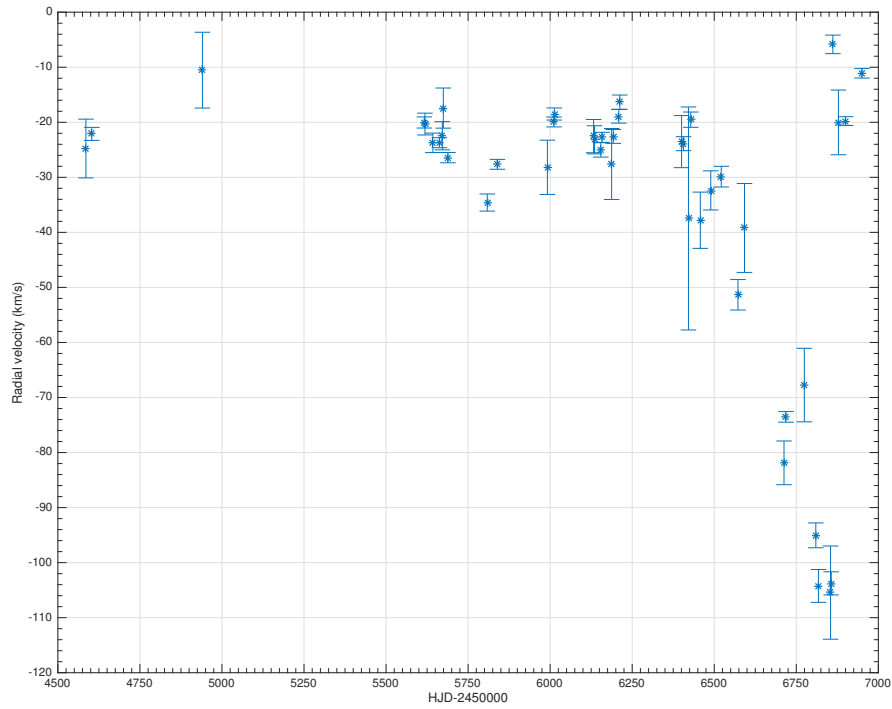
Figure 4.2: Hα central depression radial velocity.
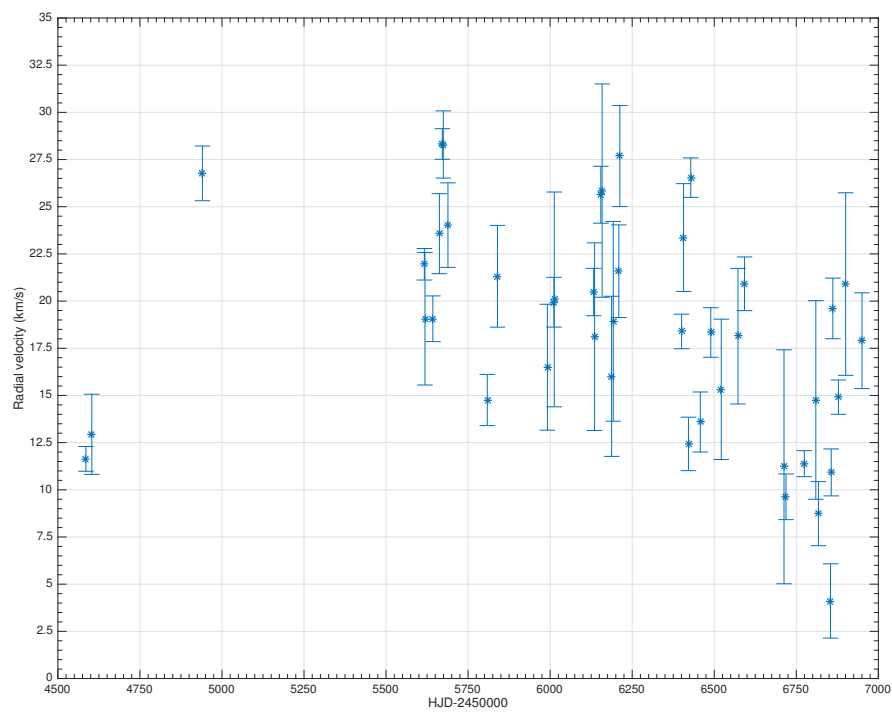
Figure 4.3: Hα red peak radial velocity.
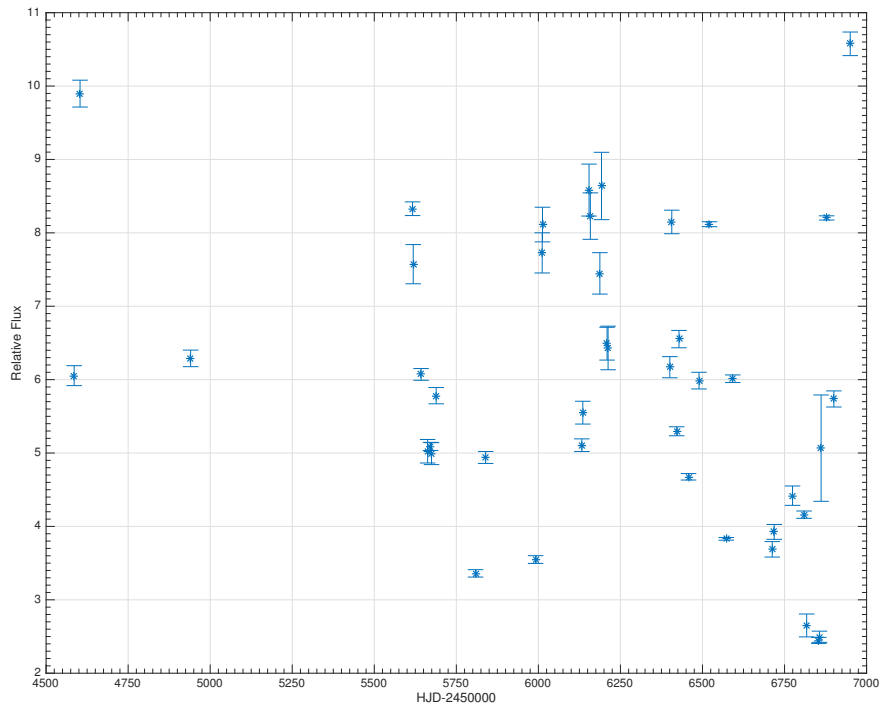
Figure 4.4: Hα violetpeak relative flux.
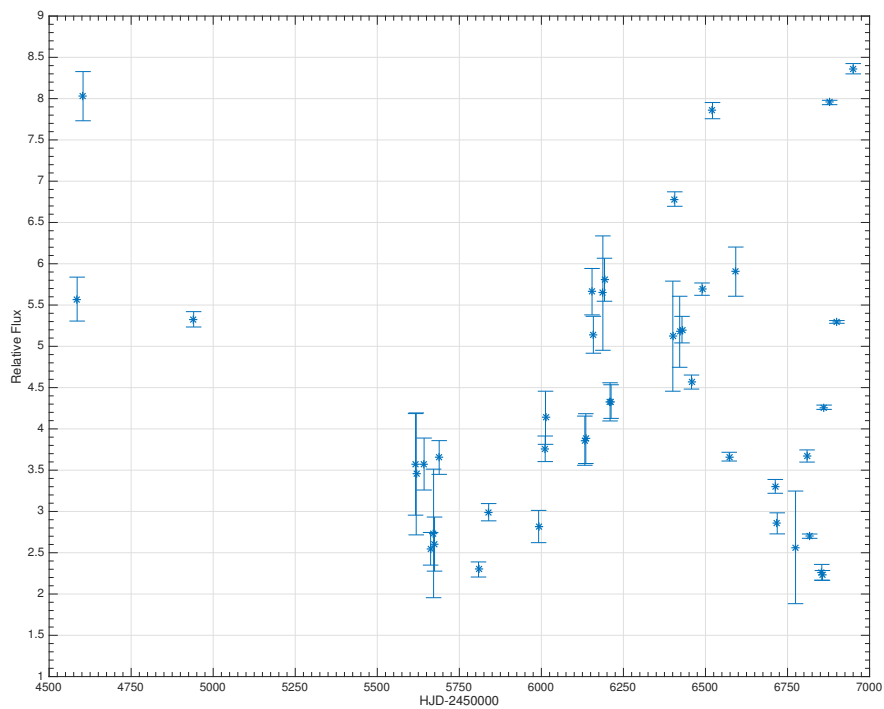
Figure 4.5: Hα central depression relative flux.
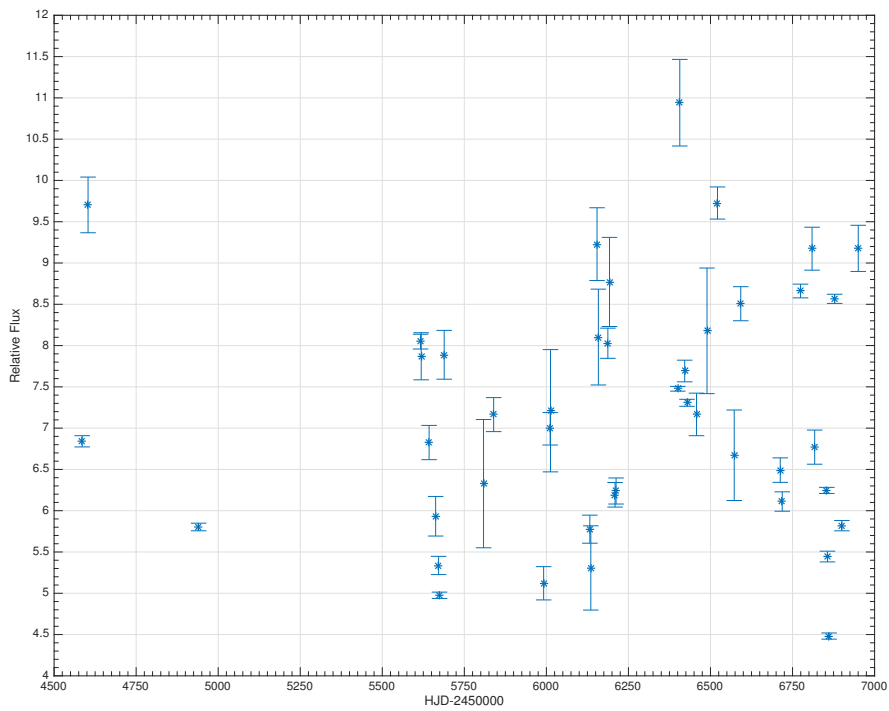
Figure 4.6: Hα red peak relative flux.
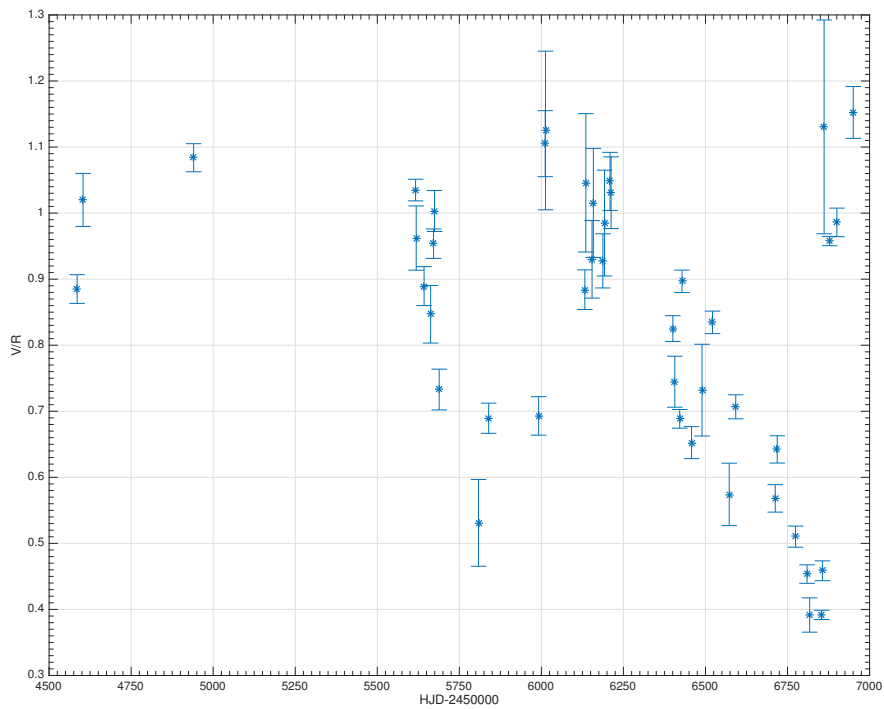
Figure 4.7: V/R ratio.
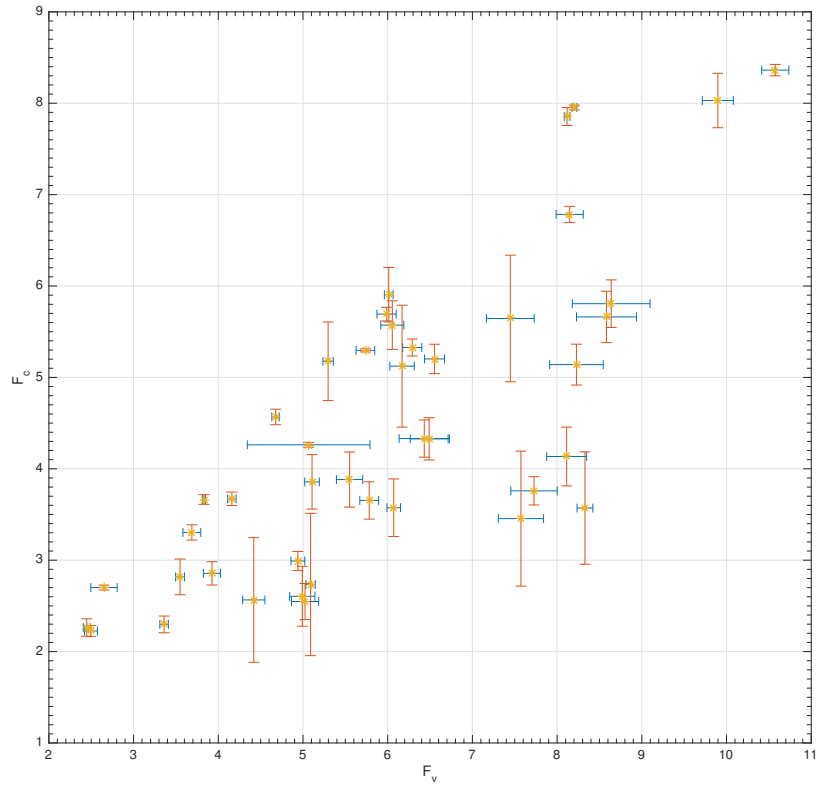
Figure 4.8: Correlation between the relative flux of the central depression and the violet peak of the Hα line.
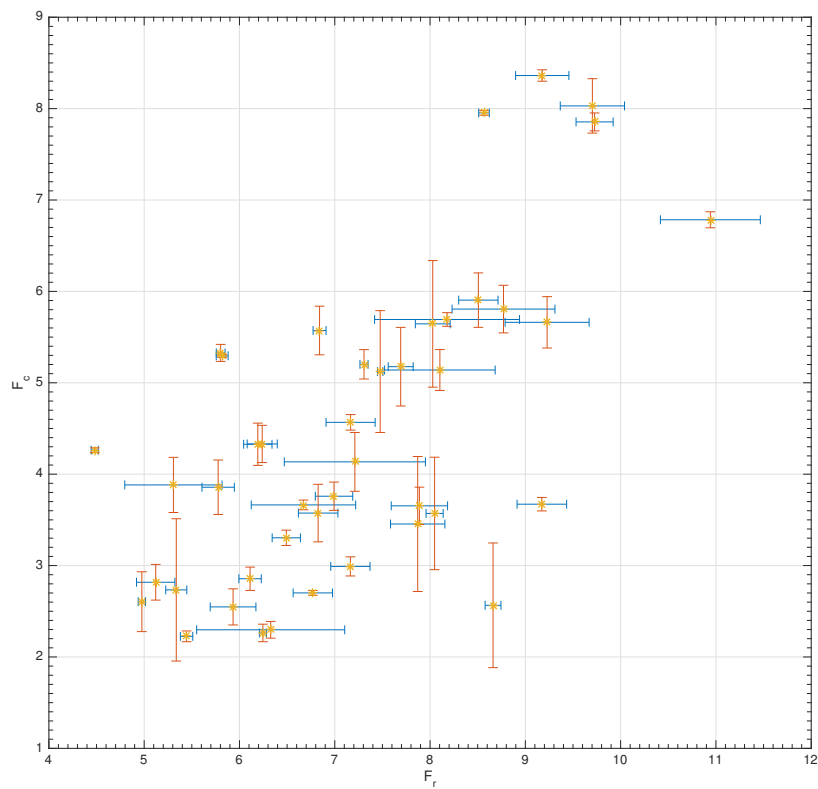
Figure 4.9: Correlation between the relative flux of the central depression and the red peak of the Hα line.
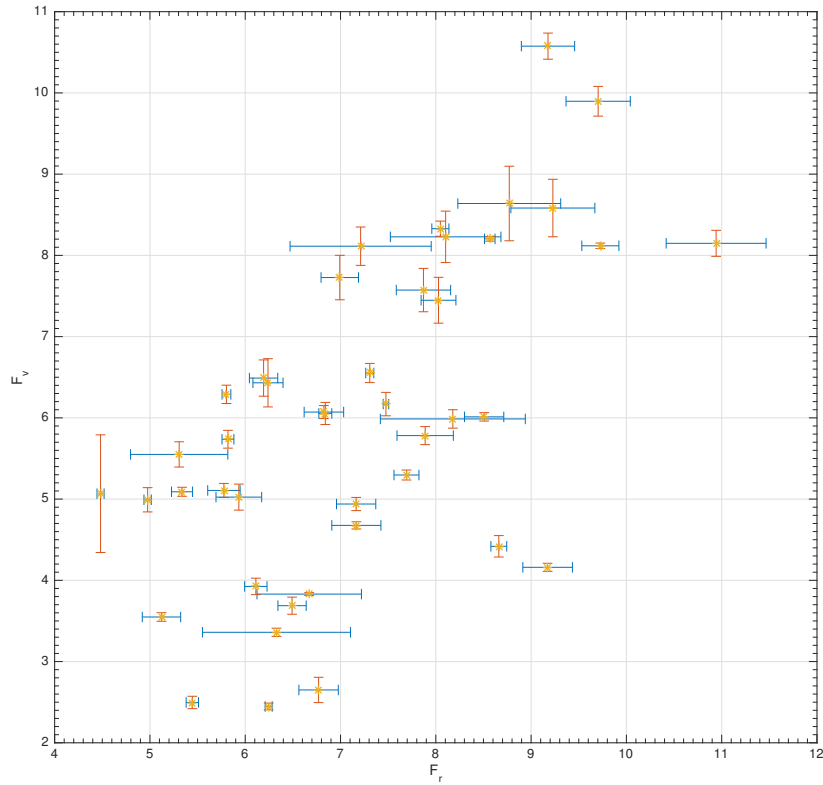
Figure 4.10: Correlation between the relative flux of the red and the violet peak of the Hα line.
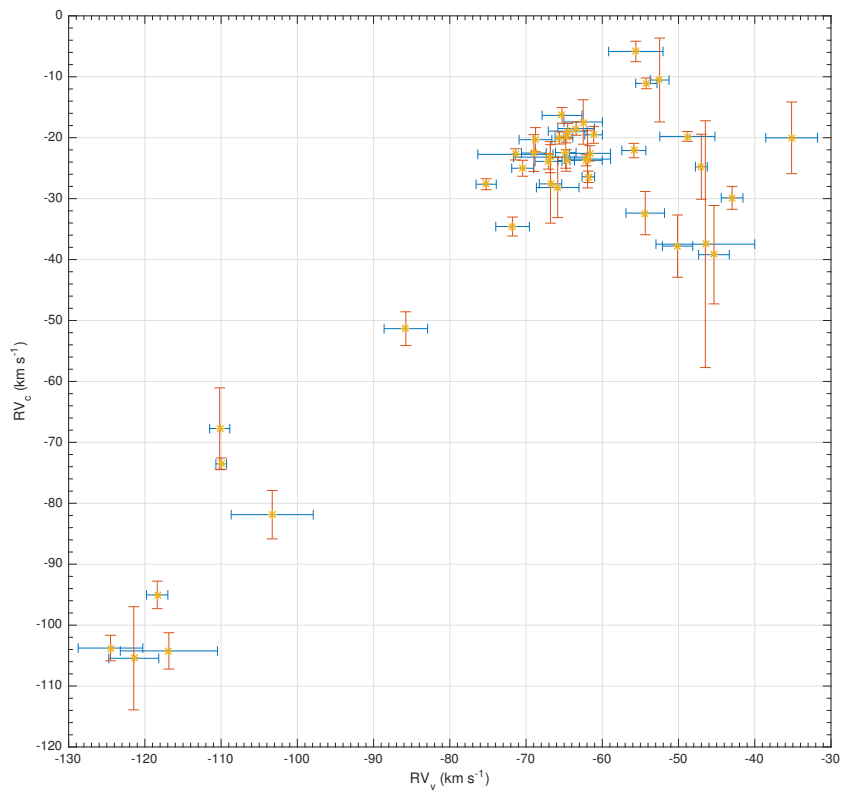
Figure 4.11: Correlation between the radial velocity of the central depression and the violet peak of the Hα line.
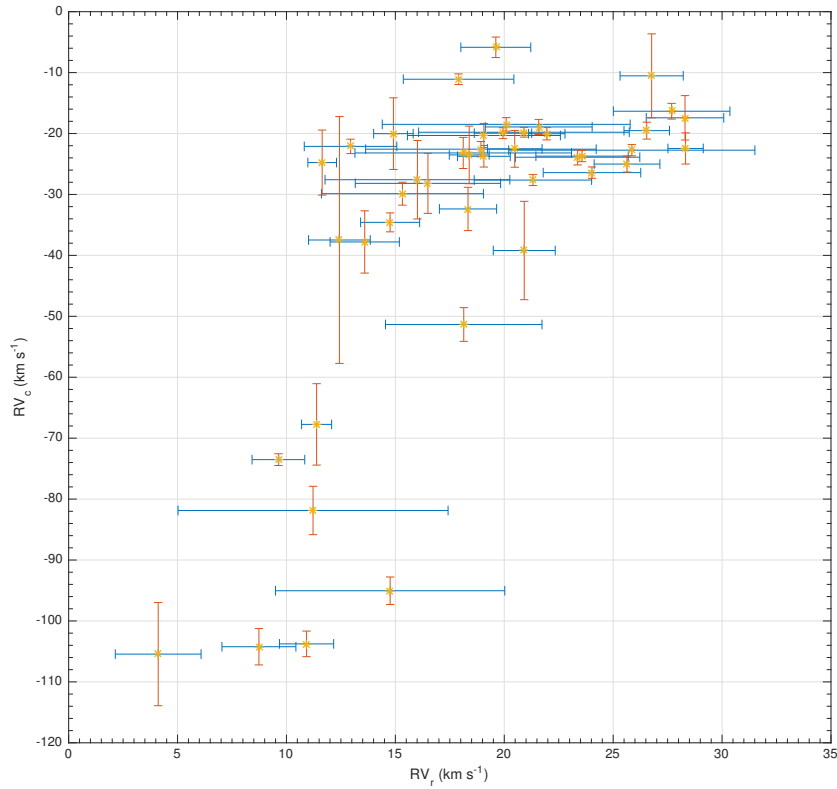
Figure 4.12: Correlation between the radial velocity of the central depression and the red peak of the Hα line.
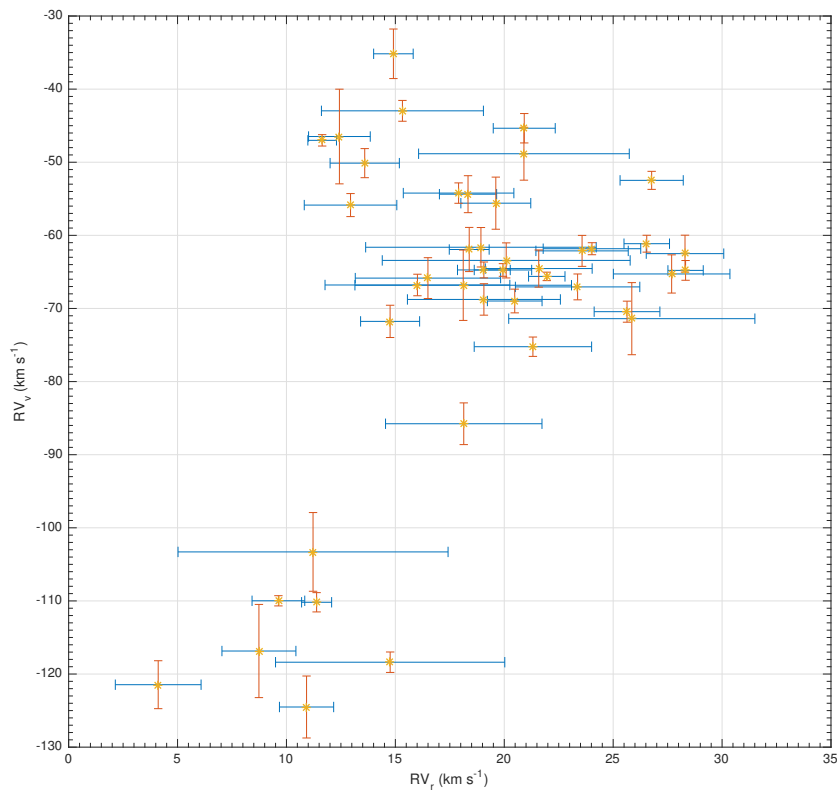
Figure 4.13: Correlation between the radial velocity of the red and the violet peak of the Hα line.

4.3.2   [O I] $\lambda\lambda$ 6300.304, 6363.776Å lines

The forbidden line [O I] 6300.304 Å is a resonance transition $^1D_2$ - $^3P_2$, where the upper level is $E_u = 1.967eV$. The forbidden line [O I] 6363.776 Å is the fine structure component transition $^1D_2$ - $^3P_1$, where the upper level is $E_u = 1.967eV$ and the lower lever is $E_l = 0.020eV$, so the two lines have the common upper level and come from the same multiplet $1F$, where F stands for forbidden. Figures 4.14 and 4.15 show their radial velocity as a function of the MJD. Figures 4.16 and 4.17 show their relative flux. Figures 4.18 and 4.19 show their (emission) equivalent width EW_λ and figures 4.20 and 4.21 show the R ratio and the ratio EW_{6300}/EW_{6364} as functions of MJD, respectively. The ratio EW_{6300}/EW_{6364} and the $R_{[OI]}$ give an estimate of the optical depth of the lines forming region; if the ratio is equal to 3, the medium is optically thin and the optical depth increases as this ratio decreases. I find that these quantities are very close to the optically thin limit. Because these two lines are from the same doublet, the RV must be the same for both. From figures 4.14 and 4.15, it is clear that the [O I] RV is constant and this radial velocity can be used for the star. The radial velocity is peaked at RV$= (-16 \pm 2)$ km s^{-1}. The EW$_\lambda$ is also constant. This means that the environment in which these lines are forming is not affected by the variations of the physical state of the central object.
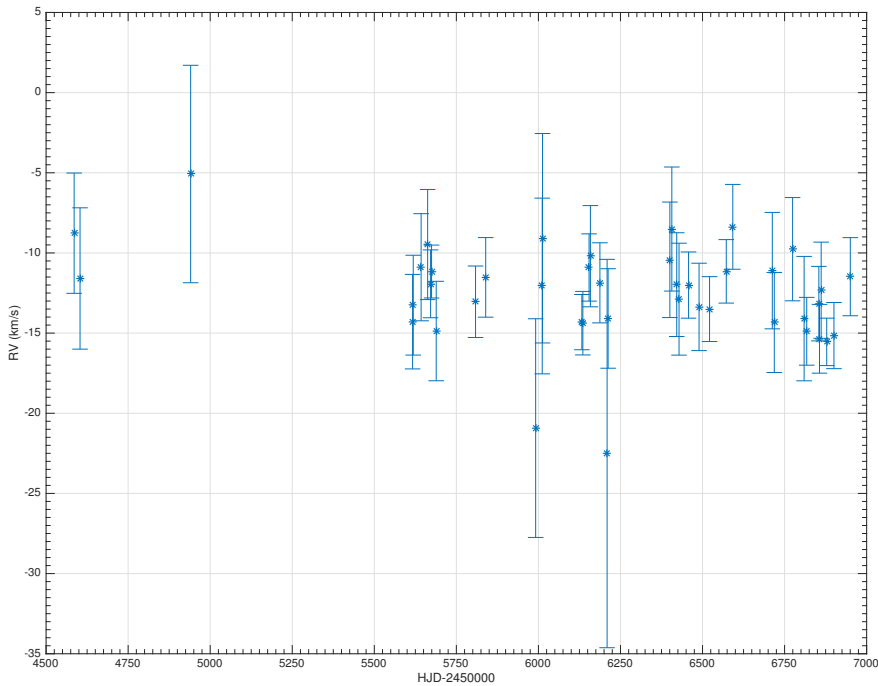
Figure 4.14: Radial velocity of the 6300.304Å [O I] line.
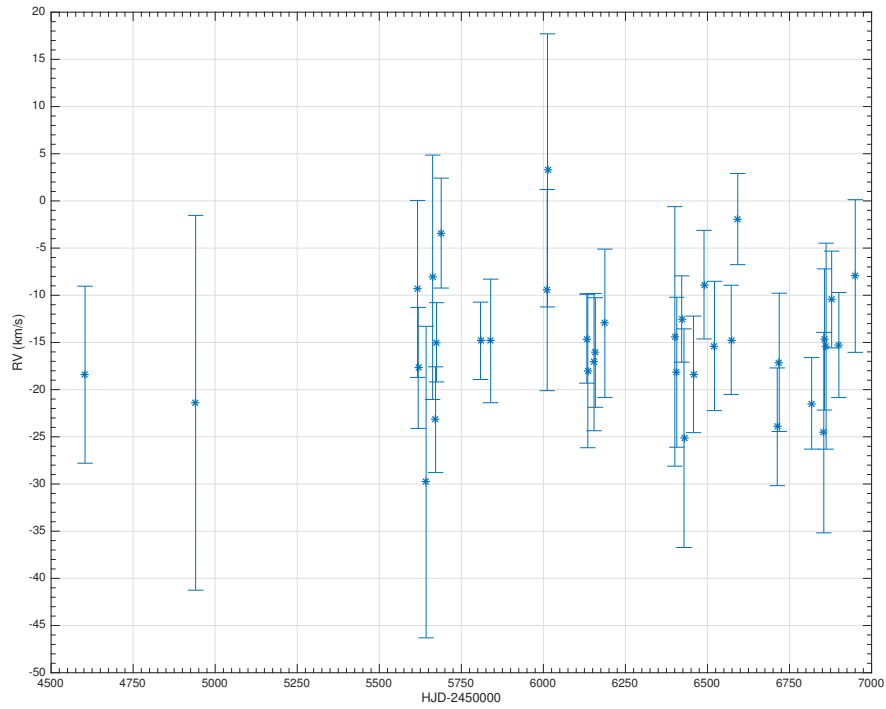
Figure 4.15: Radial velocity of the 6363.776Å [O I] line.
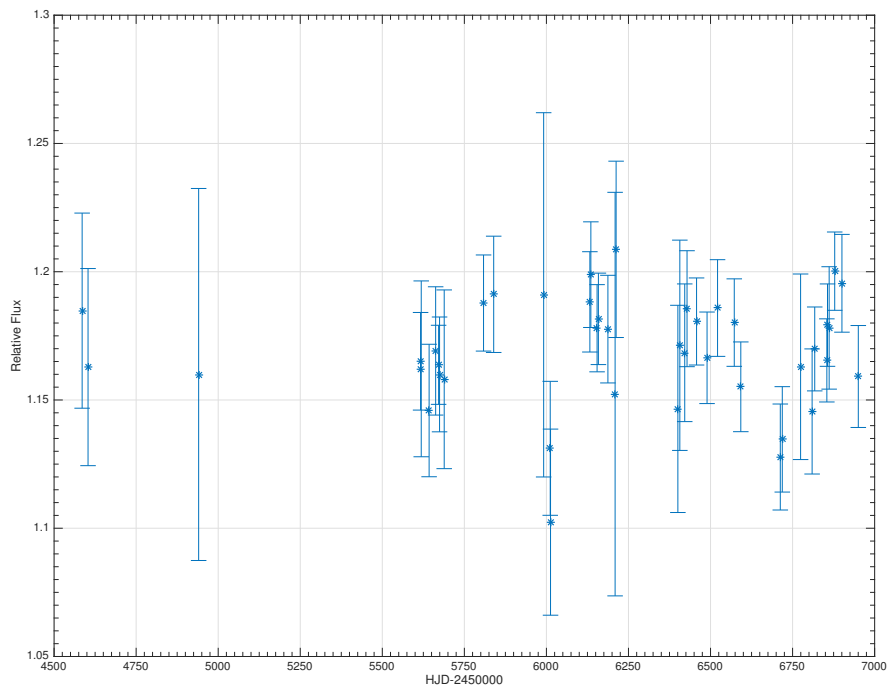
Figure 4.16: Relative Flux of the 6300.304Å [O I] line.
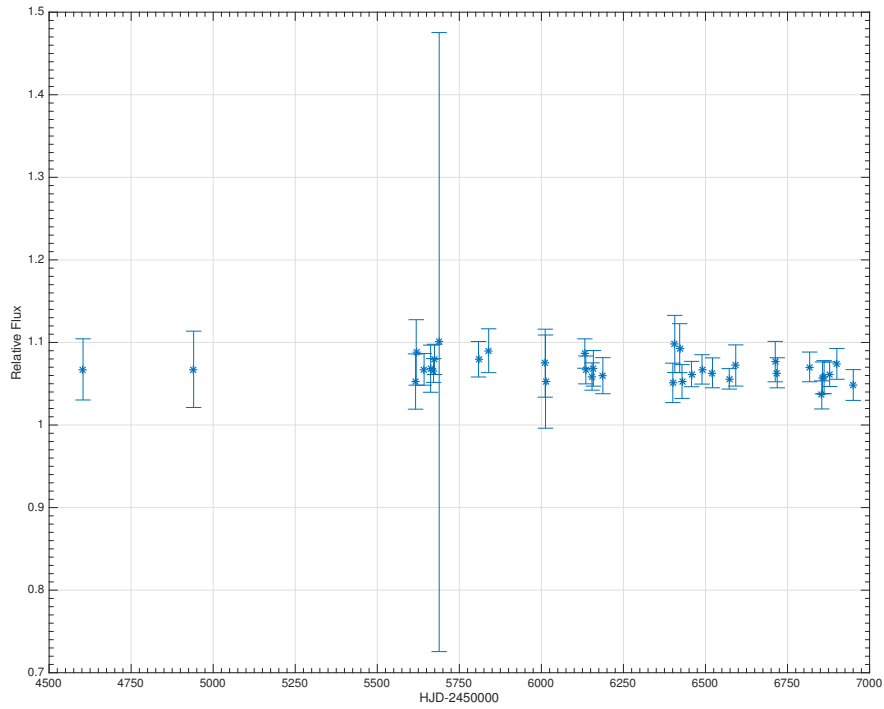
Figure 4.17: Relative Flux of the 6363.776Å [O I] line.
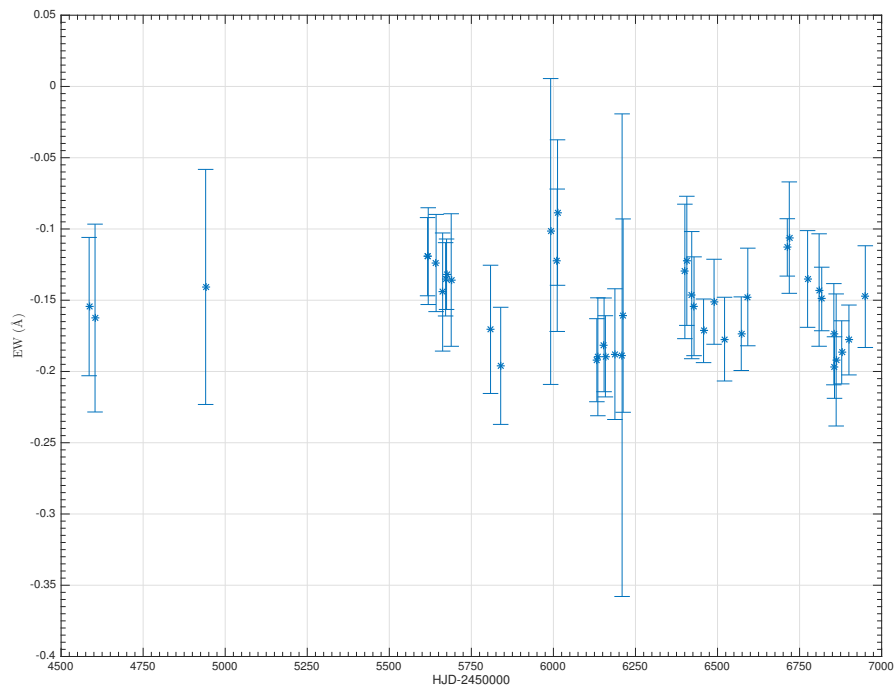
Figure 4.18: Equivalent width of the 6300.304Å [O I] line.
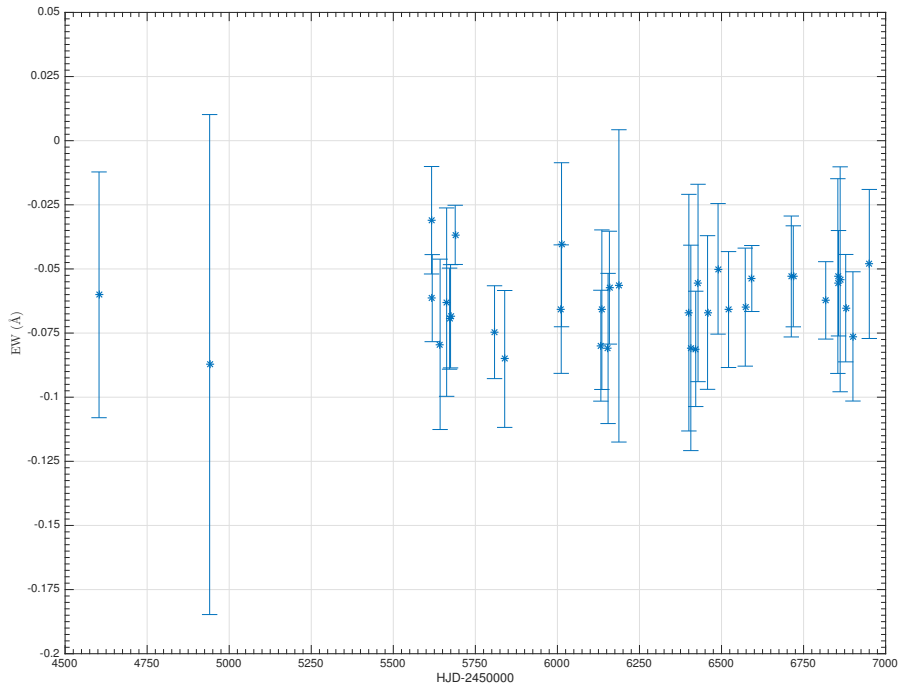
Figure 4.19: Equivalent width of the 6363.776Å [O I] line.
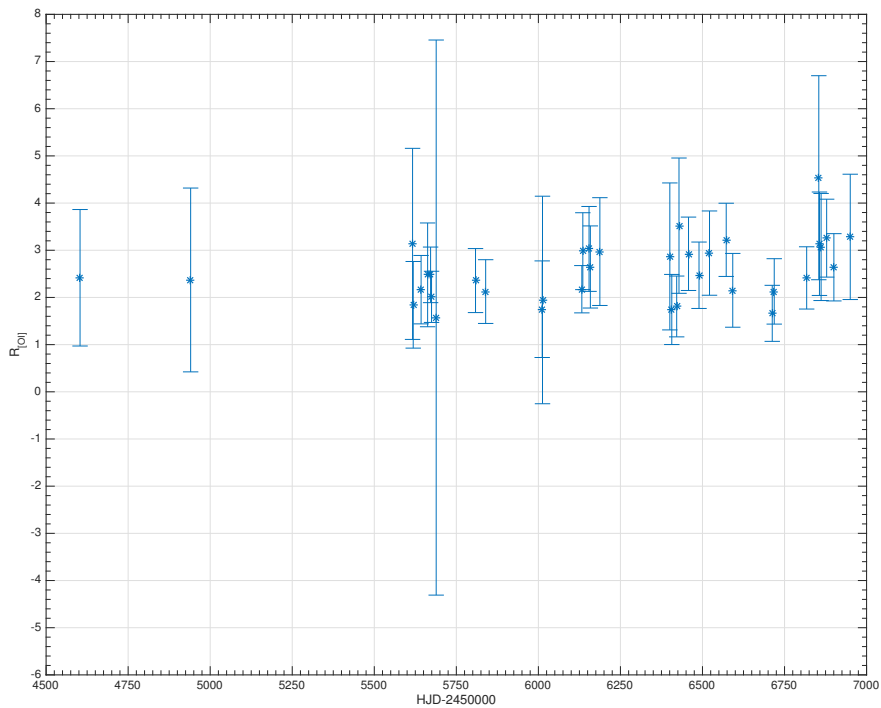
Figure 4.20: $R_{[OI]}$ factor 6300.304Å and 6363.776Å [O I] lines.
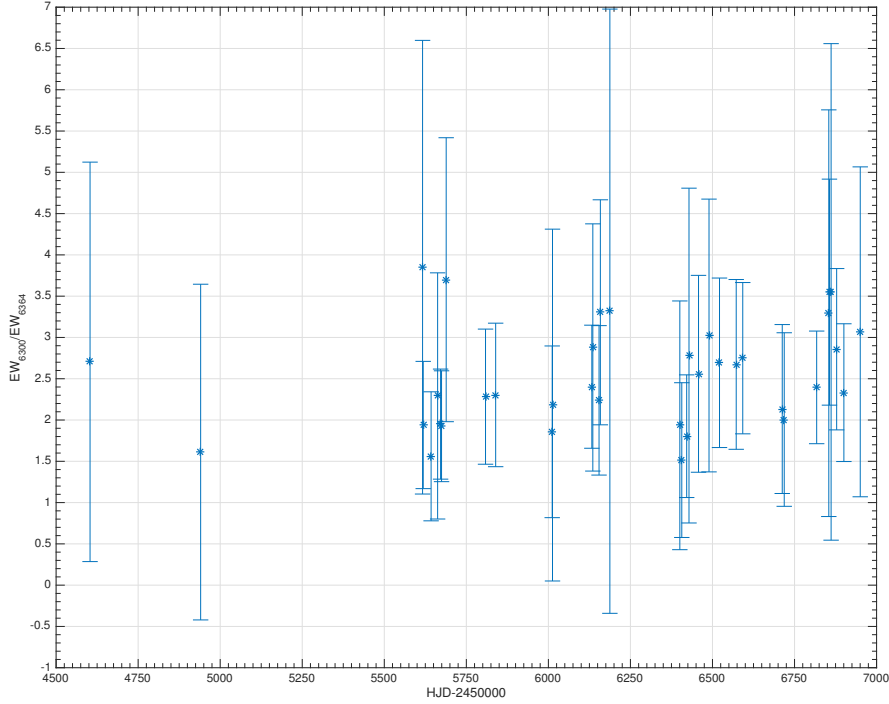
Figure 4.21: Ratio between the EW of the 6300.304Å and 6363.776Å [O I] lines.

4.3.3   Si II $\lambda\lambda$ 6347.091, 6371.359Å lines

The Si II $\lambda\lambda$ 6347.091, 6371.359Å lines have the same lower level $^2S_{1/2}$ with energy $E_l = 8.121eV$ but different upper levels, respectively $^2P^o_{3/2}$ with energy $E_u = 10.074eV$ and $^2P^o_{1/2}$ with energy $E_u = 10.066eV$. Both transitions come from multiplet number 2. Figures 4.22 and 4.23 show their radial velocity RV. As we can see, the RV for both the lines is constant to within the errors to RV= (-17 ± 2) km s^{-1} like [O I]. Figures 4.24 and 4.25 show the relative flux, and figures 4.26 and 4.27 show the EW_λ. The equivalent width of these lines does not show great variability and EW$_{6347}$ >EW$_{6371}$, which is expected because the lines have different oscillator strengths.
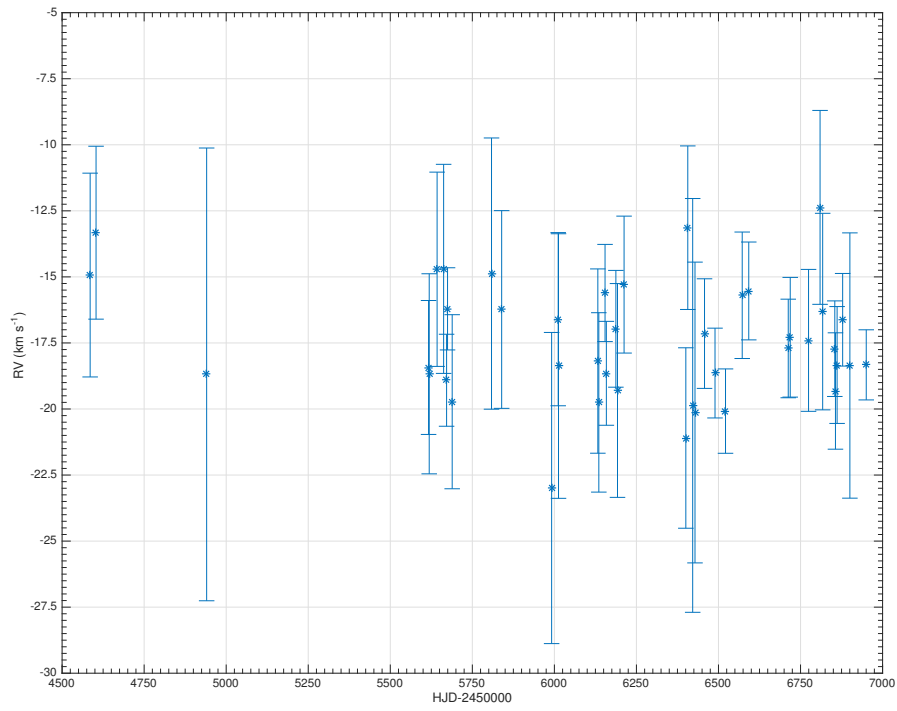
Figure 4.22: Radial velocity of the 6347.091Å Si II line.
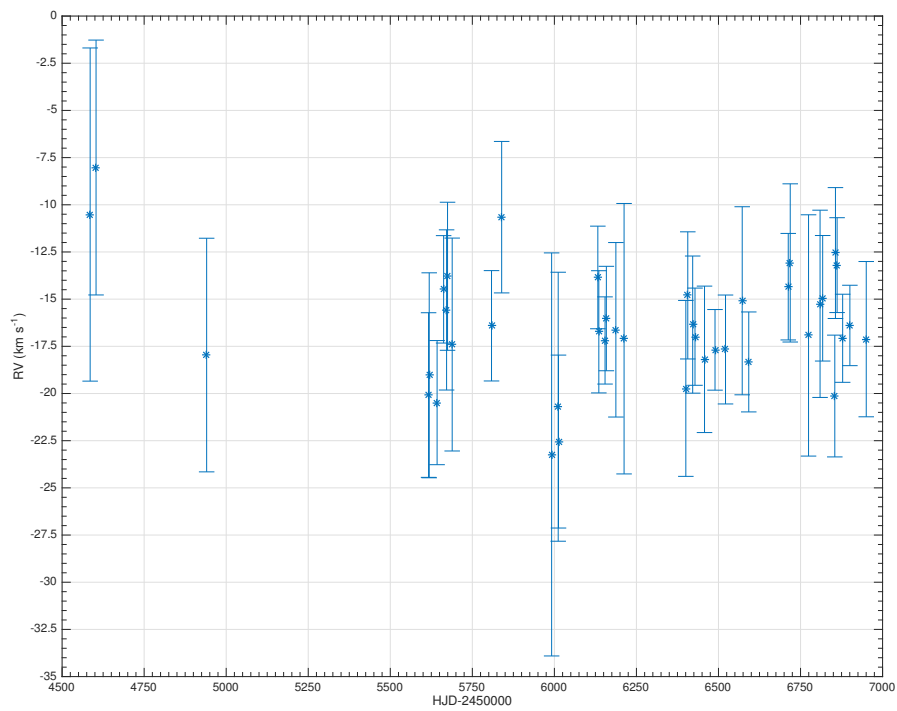
Figure 4.23: Radial velocity of the 6371.359Å Si II line.
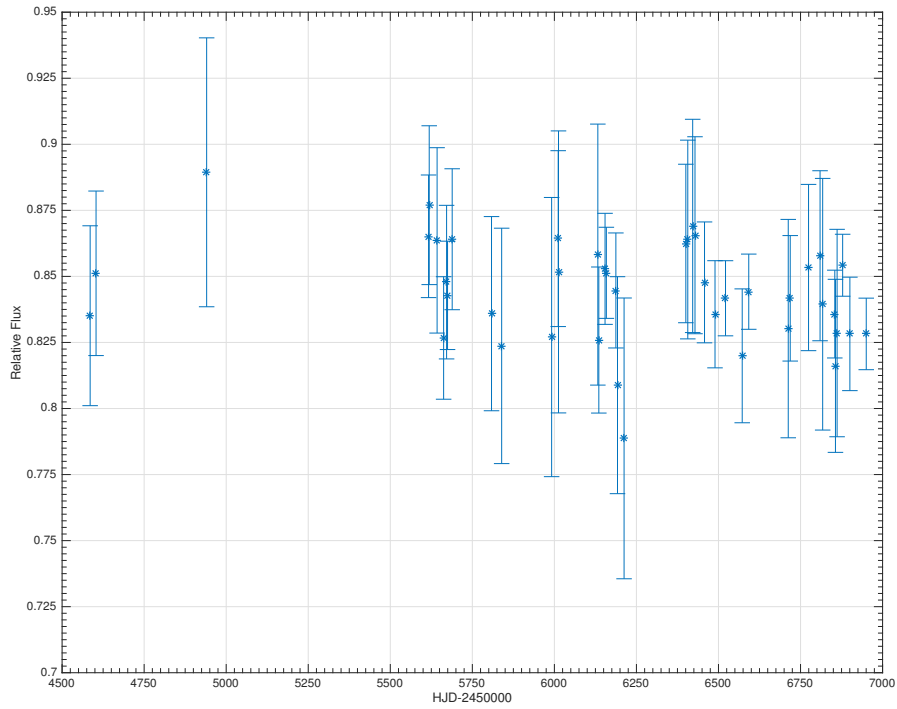
Figure 4.24: Relative Flux of the 6347.091Å Si II line.
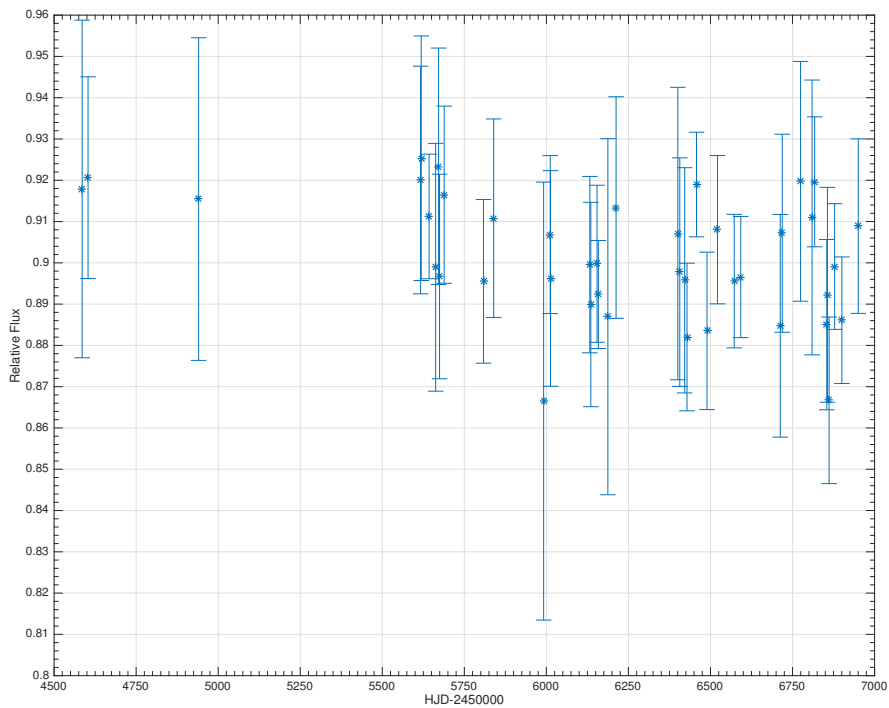
Figure 4.25: Relative Flux of the 6371.359Å Si II line.
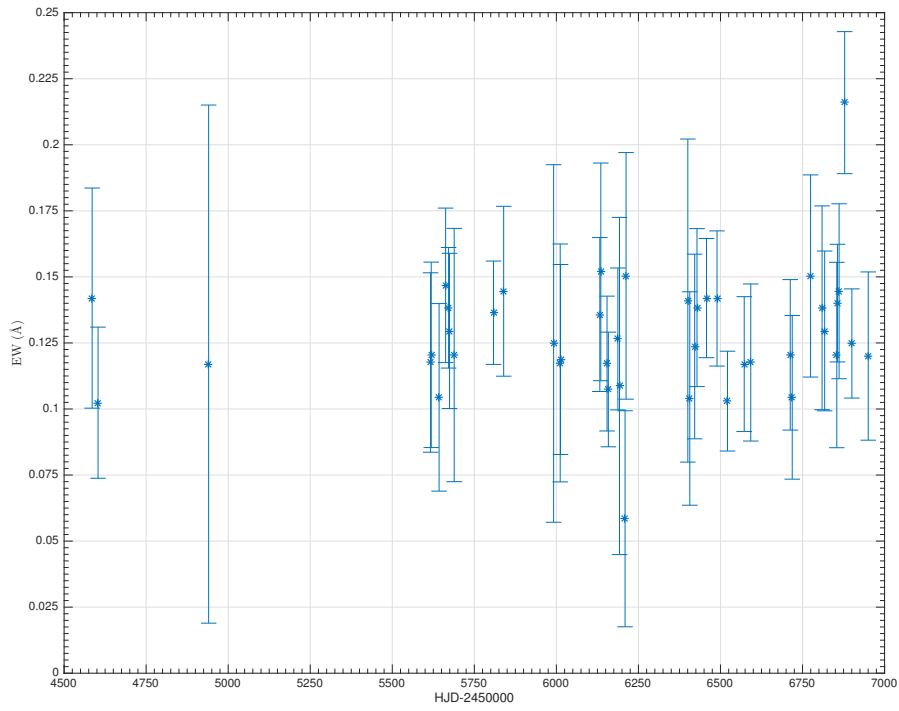
Figure 4.26: Equivalent width of the 6347.091Å Si II line.
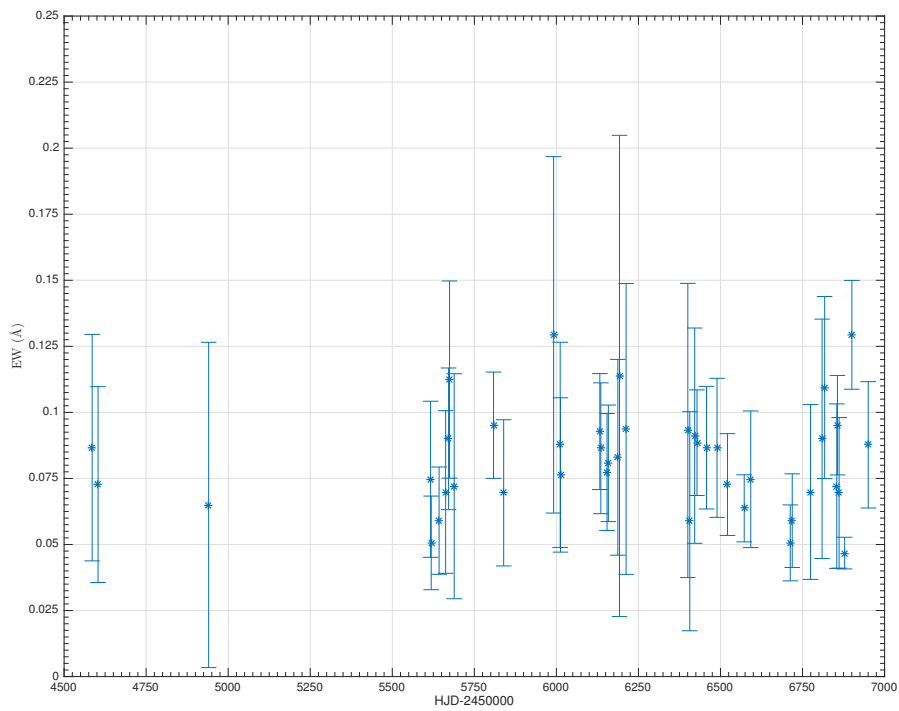
Figure 4.27: Equivalent width of the 6371.359Å Si II line.

4.4   Line Profile Variations

If we want to see if some dynamical phenomena are changing the structure of the source and its envelope, we must see how the spectral line profile is changing in time. To do this, it is better to plot the spectral line in velocity instead in wavelength. The rest wavelength is the zero velocity. I do this for Balmer lines, He I, Fe II, Mg I, Mg II, Ca II, Si II, Na I and O I. I'm using different spectra with different spectral resolution and a crude comparison could lead to wrong conclusions. To avoid this problem, the higher resolution spectra have been processed to the lowest resolution. The spectra f at higher resolution are convolved with a gaussian filter g of N points and standard deviation $\sigma = m \cdot d\lambda$, with $d\lambda = \lambda_j^{low} - \lambda_{j-1}^{low}$ using the resolution of the spectra at lower resolution. N is chosen in such a way that the normalized gaussian is truncated at value of 10^{-4}. The resulting function f_c from the convolution is then interpolated with a cubic spline to obtain a lower resolution spectra f_i. The parameter m is chosen comparing the atmospheric lines from the lowest resolution spectra with the convolved and interpolated f_i spectrum. For the convolution and the interpolation, Matlab provides the functions called $conv(f, g,' same')$ and the $interp1(\lambda_{high}, f_c, \lambda_{high \rightarrow low},' spline')$. $conv$ requires the two input vectors for the convolution and, in this case the option $'same'$ that creates the output vector f_c with the same length of f. $interp1$ requires the higher resolution λ_{high} vector, the vector that has to be interpolated f_c, the new lower resolution $\lambda_{high \rightarrow low}$ vector and the function used for the interpolation, that in this case is a cubic spline. Figure 4.28 shows the comparison between the atmospheric lines from CFHT at original resolution (blue line) and SPM (red line); figure 4.29 shows the comparison between the same atmospheric lines from CFHT after the convolution and interpolation (blue line) and SPM (red line).
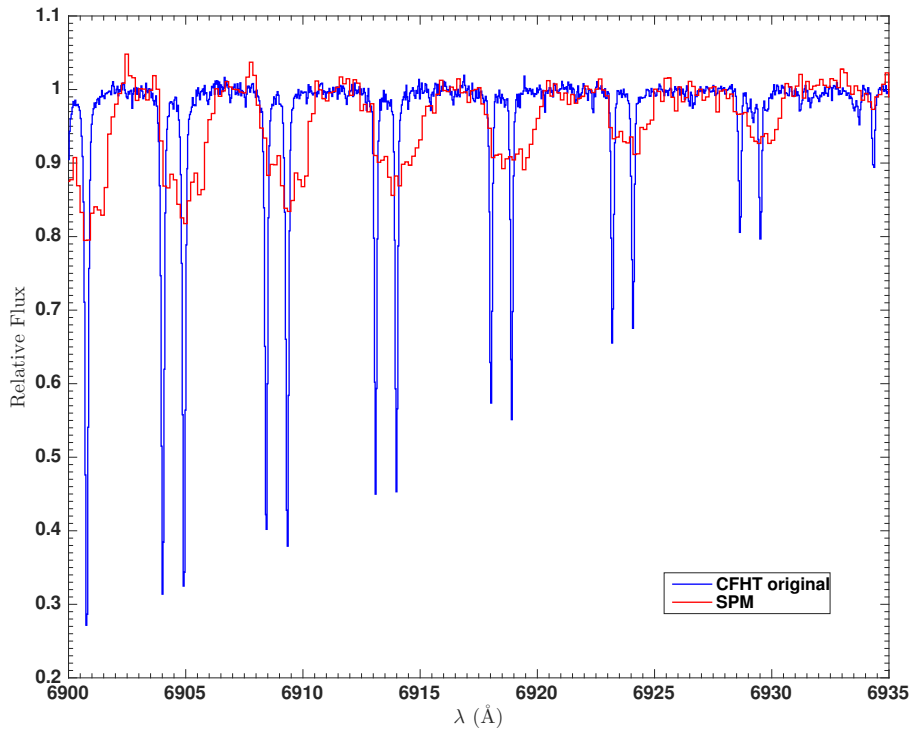
Figure 4.28: Atmospheric lines comparison before the convolution. Spectra from CFHT (blue line) and SPM (red line). The atmospheric lines from CFHT are shifted respect SPM because of the different heliocentric velocity of the Earth in the two days of observations.
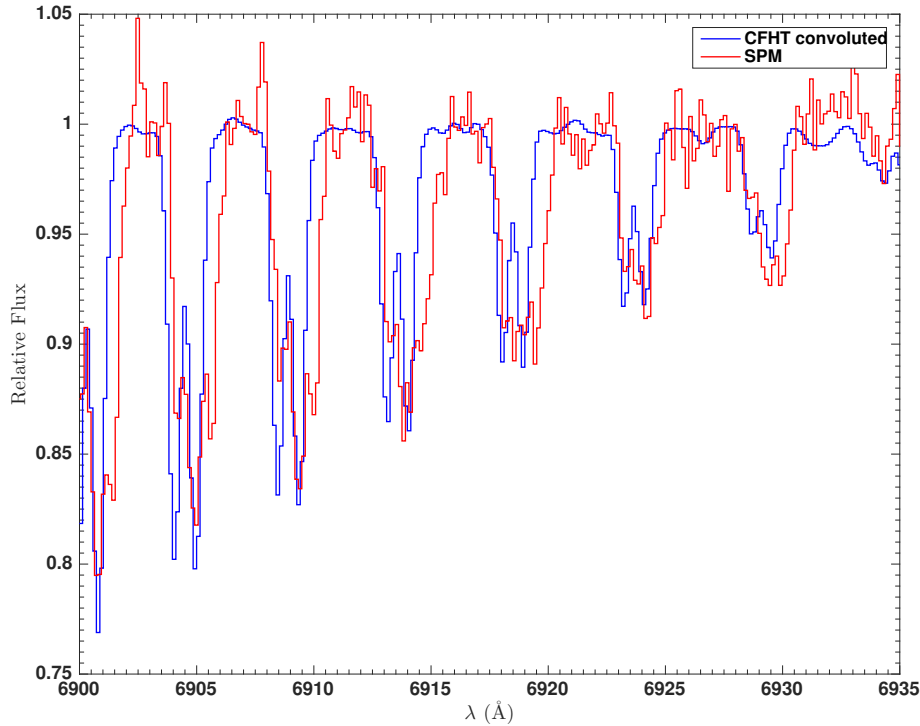
Figure 4.29: Atmospheric lines comparison after the convolution and interpolation. Spectra from CFHT (blue line) and SPM (red line).The atmospheric lines from CFHT are shifted respect SPM because of the different heliocentric velocity of the Earth in the two days of observations.

When comparing the Ondřejov, the McDonald, the CFHT and the San Pedro Martir spectra, the lower resolution spectra are these from Ondřejov, so the others are convolved to lower resolution. In the case where there are only San Pedro Martir, CFHT and McDonald spectra, the spectra from the latter two observatories are convolved to the SPM resolution. To better compare the spectra, it is useful to plot the curves in *histogram* mode.

4.4.1   Balmer lines

The Balmer lines are the Hydrogen lines that come from the transition between the second energy level ($n = 2$) and higher energy levels. The Balmer lines are strongest in absorption in late B-type and early A-type stars reslative to other spectral type, and so these lines are very important for the object IRAS $17449 + 2320$.

In the next sections, I will show the Balmer lines from Hα to Hδ, focusing on the dynamical changes in the lines.

4.4.1.1   Hα

As said before, Hα line is in emission with wings in absorption and the core composed by a self absorption feature forming a double peak profile, in which the peaks are called violet and red peak and the self absorption feature is called central depression.

Figure 4.30 shows the velocity line profile of the core of Hα line from the spectra taken from CFHT and San Pedro Martir observatories. These plots are very useful for recognizing the presence of dynamical phenomena that can alter the line profiles. In the complete data set, we see that the violet, the red peak and the central depression are changing in time leading to a change in time of the V/R ratio.

The line is in emission and so it must form in a less opaque circumstellar environment. As [O I] can be used as an indicator of the physical phenomena acting in the circumstellar material. The central depression feature caused by self absorption indicates the presence of a region that is optically thicker than the emitting region.
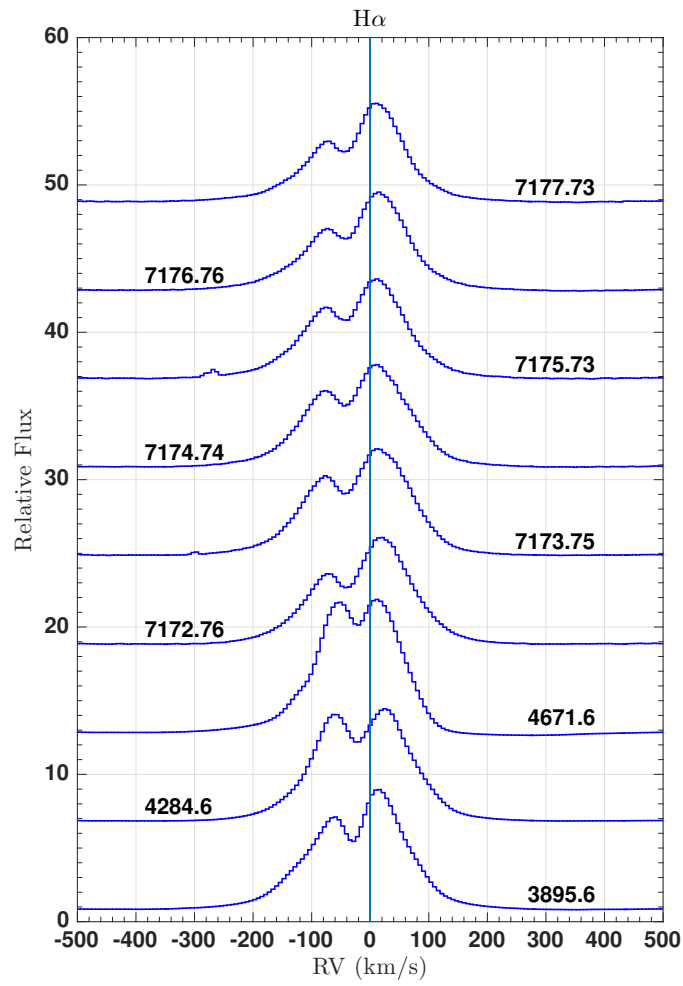
Figure 4.30: Hα: velocity line profile variations. Spectra taken from CFHT and San Pedro Martir. The number on each spectrum is the MJD.

4.4.1.2   Hβ

The Hβ line comes from the transition between the levels with $n_u = 4$ and $n_l = 2$ and has a wavelength $\lambda = 4861.332$Å.

The line profile of the core of Hβ from the spectra of the McDonald, CFHT and San Pedro Martir observatories is shown in figure 4.31. For the McDonald spectrum (MJD = 5080.63), it was not possible to fit the continuum in a good way because the line is located in the peripheral pixels of the CCD and so the wings of the line seem to be flat. Its radial velocity may also be wrong, but not the shape of the core.

Because the San Pedro Martir spectra are taken for six consecutive days (SPM2015 MJD = $7172 \div 7177$), then it is possible to find possible variabilities with time scale of the order of days in the line profiles.

The wings of the line are in absorption, but the core is complex and shows both emission and absorption components. This line seems to be formed in an environment optically thicker than Hα because the absorption component is dominant respect the emission one.

In SPM2015 case, Hβ shows complex absorption features that are shifting day-by-day in RV. This is clear looking at the San Pedro Martir spectra in figure 4.31 (MJD = $7172 \div 7177$). The self-absorption feature shifts to the red (positive radial velocities) from a radial velocity of ≈ -40 km s^{-1} to ≈ 80 km s^{-1} and, at the same time, the red peak also shifts and decreases its flux until it disappears and around $-30 km/s$ a second self-absorption feature appears on the blue side forming other two peaks.
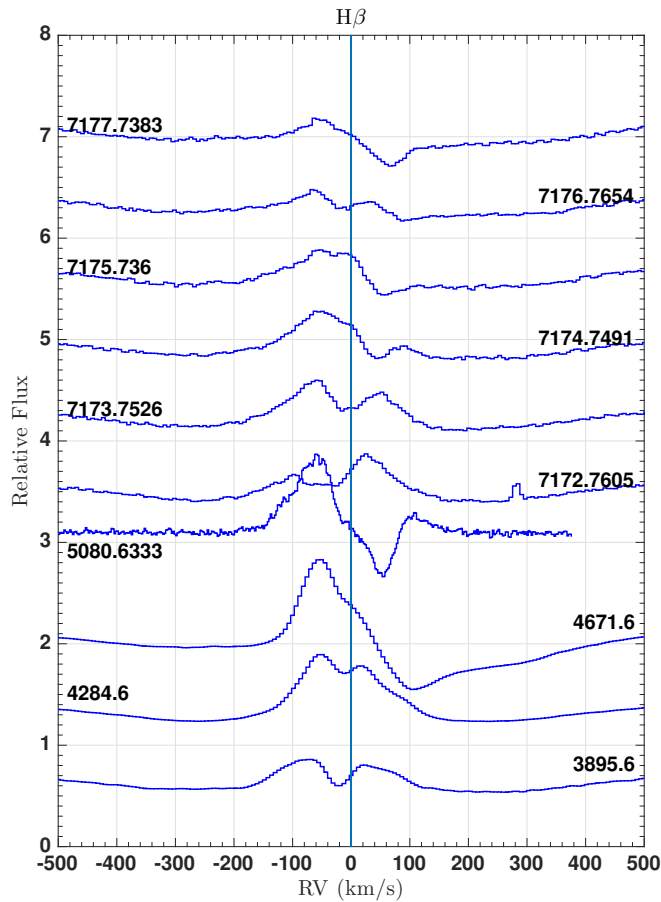
Figure 4.31: Hβ: velocity line profile variation. Spectra taken from the observatories of McDonald, CFHT and San Pedro Martir. The number on each spectrum is the MJD. The spectrum with MJD= 5080.63 is from McDonald and it was not possible to fit the continuum in a good way because the line is located in the final pixels of the CCD and so the wings of the line seem to be flat.

4.4.1.3   Hγ

The Hγ line comes from the transition between the levels with $n_u = 5$ and $n_l = 2$ and has a wavelength $\lambda = 4340.468$Å.

    The line profile of the Hγ core from the spectra of the McDonald, CFHT and San Pedro Martir observatories is shown in figure 4.32. The wings of the lines are in absorption and the core presents complex absorption features like Hβ but with weaker emission. Like Hβ, this line formed in deeper region than Hα but also than Hβ. The Hγ line profile of the SPM2015 spectra changes day by day following the behaviour of the Hβ line, where the absorption feature shifts from a radial velocity of $\approx -40 km/s$ to $\approx 80 km/s$.
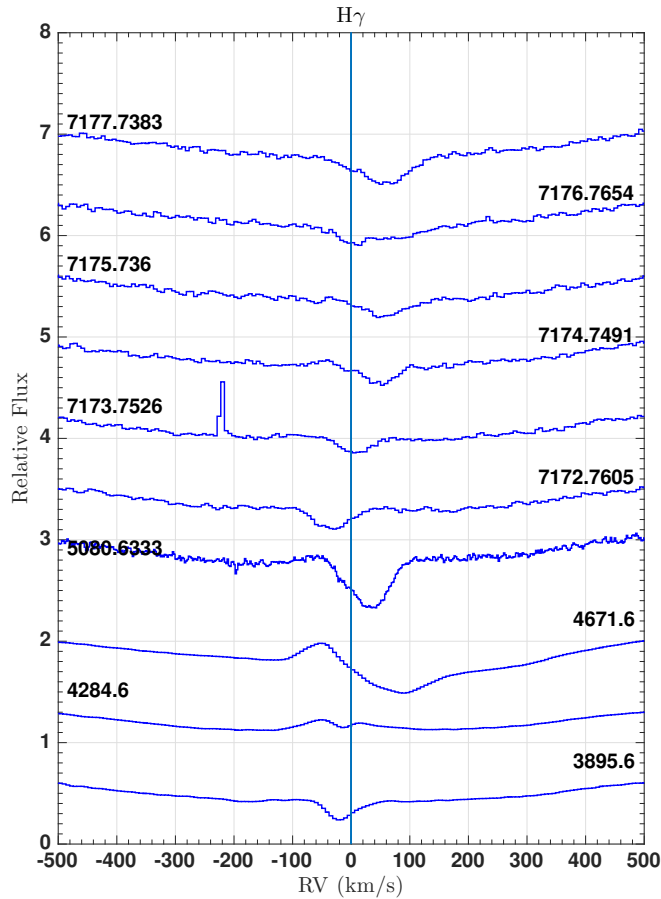
Figure 4.32: Hγ: velocity line profile variation. Spectra taken from the observatories of McDonald, CFHT and San Pedro Martir. The number on each spectrum is the MJD. In the spectrum with MJD= 7173.7526, there is an emission feature compatible with a cosmic ray.

4.4.1.4   Hδ

The Hδ line comes from the transition between the levels with $n_u = 6$ and $n_l = 2$ and has a wavelength $\lambda = 4101.737$Å.

     The line profile of the Hδ from the spectra of the McDonald, CFHT and San Pedro Martir observatories is shown in figure 4.33. It also has absorption wings and a complex core. As Hβ and Hγ, this line is forming in an optically thicker region respect the Hα but also respect the Hβ. In the SPM2015 case, we can see that the absorption feature is shifting to the red part day by day from a radial velocity of ≈ -40 km s^{-1} to ≈ 80 km s^{-1}.
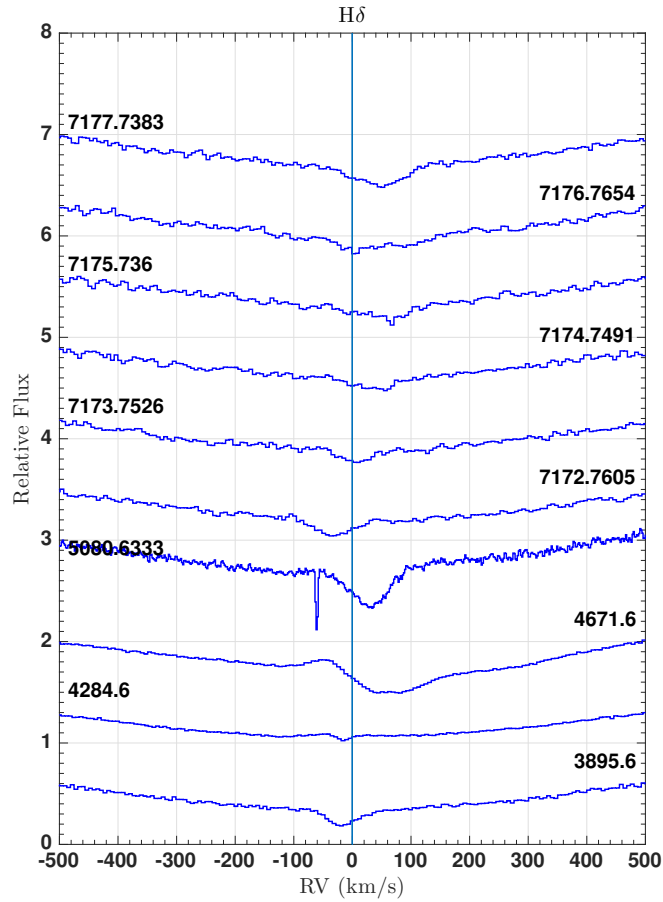
Figure 4.33: Hδ: velocity line profile variation. Spectra taken from the observatories of McDonald, CFHT and San Pedro Martir. The number on each spectrum is the MJD.

4.4.1.5 Wings and core of Balmer lines

It is useful to plot all the Balmer line (Hα, Hβ, Hγ and Hδ) in a single plot. In this way, it is possible to observe the behaviour of these lines for each day of observation. I will report the spectra from San Pedro Martir, McDonald and CFHT. Figures 4.34, 4.35 and 4.36 show the Balmer lines from the spectra of the CFHT observatory respectively on the days 2006/06/09, 2007/07/02 and 2008/07/24. Figures 4.37, 4.38, 4.39, 4.40, 4.41 and 4.42 show the Balmer lines from SPM2015 taken on days from 2015/05/29 to 2015/06/03.

For each day of observation, I plot the Balmer lines, first in a range of velocity that is $[-1800, 1800]$ km s^{-1} and second in a range of velocity that is $[-500, 500]$ km s^{-1}. The first range is useful for studying the broad wings of Balmer lines, the second range for the variable line core. For the first range, the Hα line is cutted, and it is showed only its wings. In the second range, the Hα flux is scaled by a factor 4, for display better all the Balmer lines together. This rescaling of the line does not change the profile.

The plots in the range $[-1800, 1800]$ km s^{-1} show that the wings of the Balmer lines are broad. As we can see, in the case of SPM 2015, the absorption features in Hβ, Hγ and Hδ move together with the same velocities, but the central depression of Hα is almost stationary. This behaviour suggests that the Balmer lines, except Hα, are forming in a region where dynamical phenomena are changing the optical depth creating the complex absorption features. The complex absorption features can be explained by a transient structure orbiting around the central object.
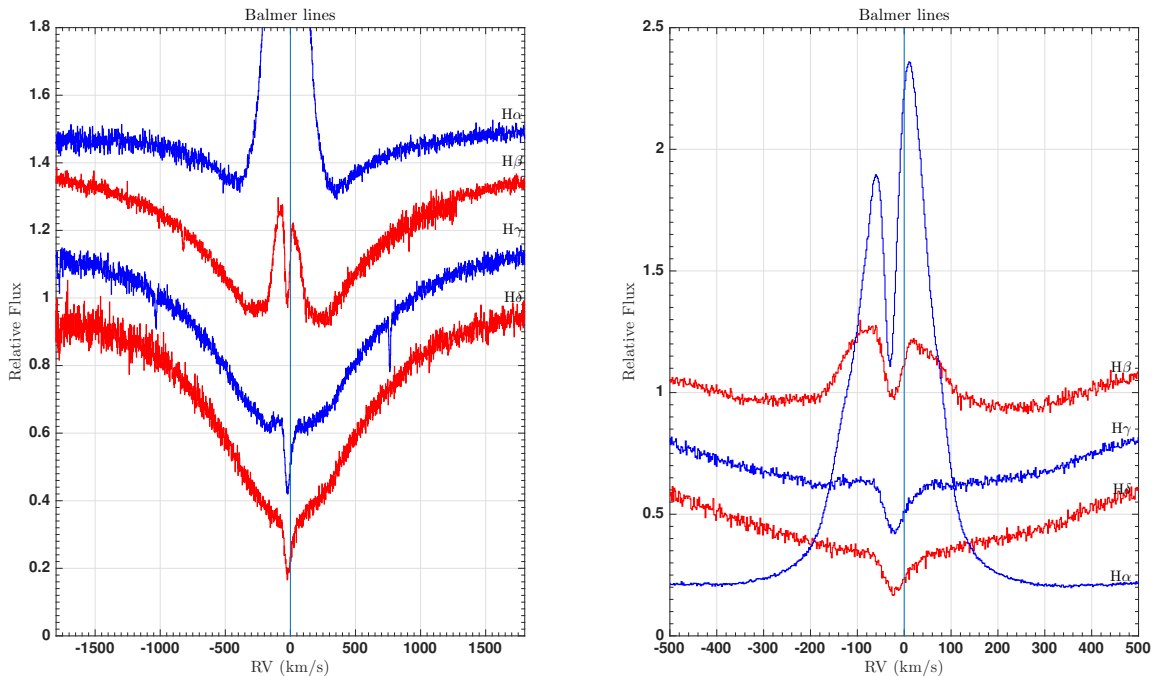
Figure 4.34: Line profile changes of the Balmer lines. Spectra taken from CFHT MJD= 3895.60. On the left the Balmer lines are plotted in the range $[-1800, 1800]$ km s^{-1}, on the right in the range $[-500, 500]$ km s^{-1} .
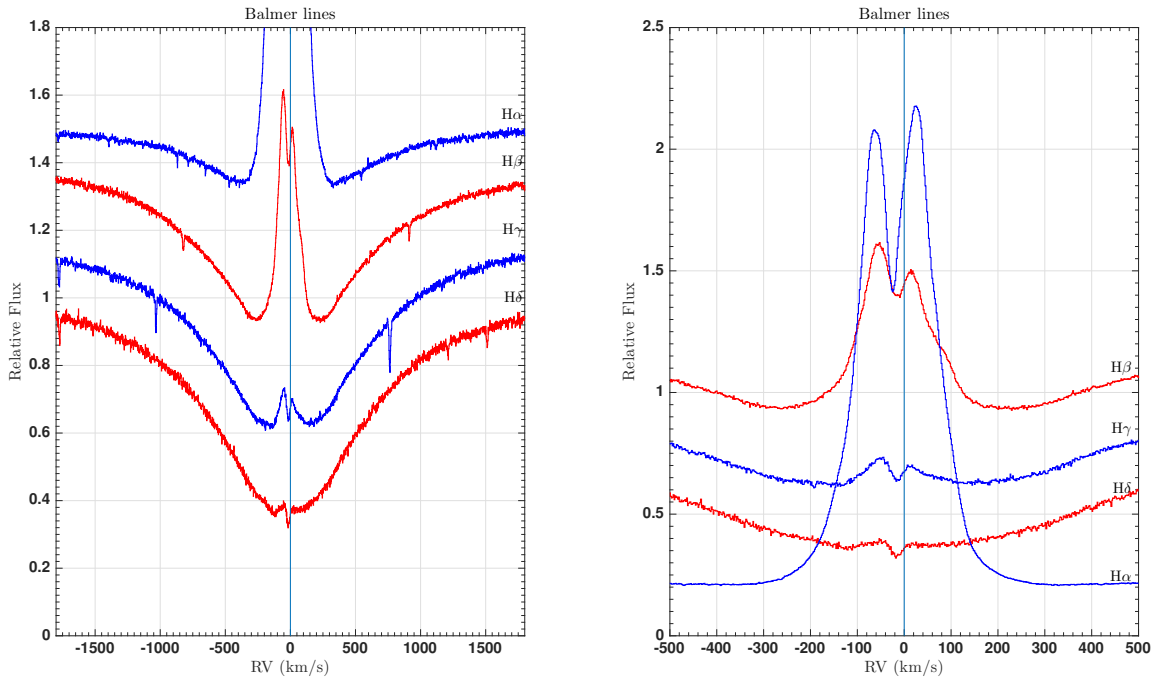
Figure 4.35: Line profile changes of the Balmer lines. Spectra taken from CFHT MJD= 4284.60. On the left the Balmer lines are plotted in the range $[-1800, 1800]$ km s^{-1}, on the right in the range $[-500, 500]$ km s^{-1}.
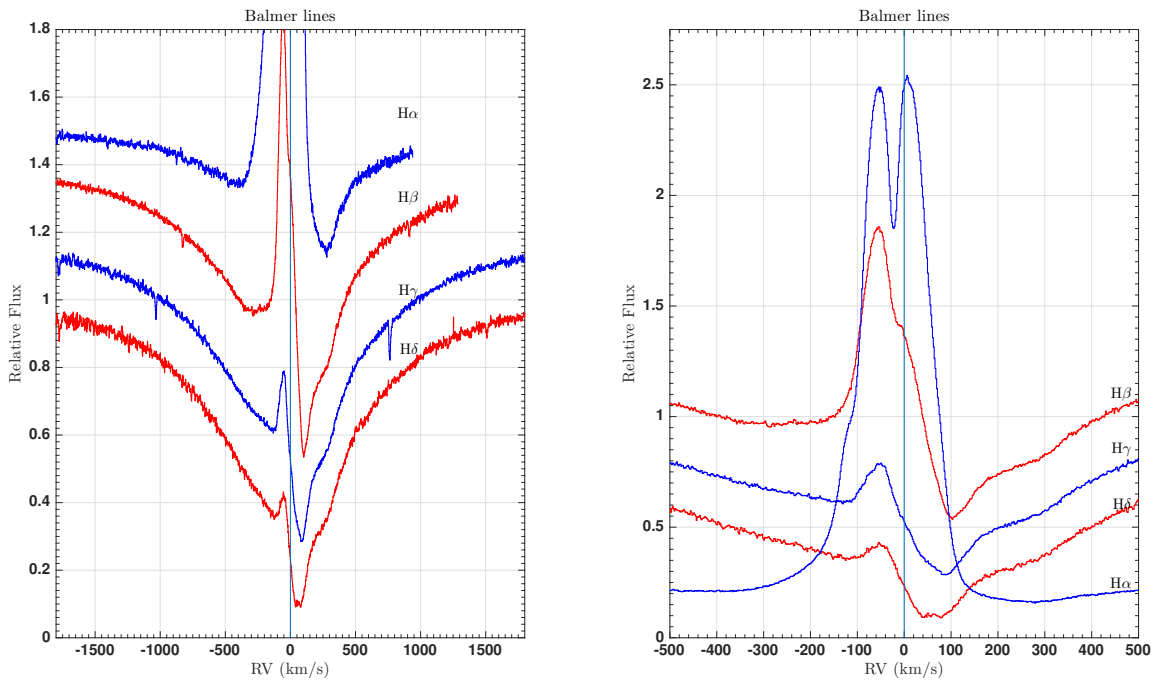
Figure 4.36: Line profile changes of the Balmer lines. Spectra taken from CFHT MJD= 4671.60. On the left the Balmer lines are plotted in the range $[-1800, 1800]$ km s^{-1}, on the right in the range $[-500, 500]$ km s^{-1}.
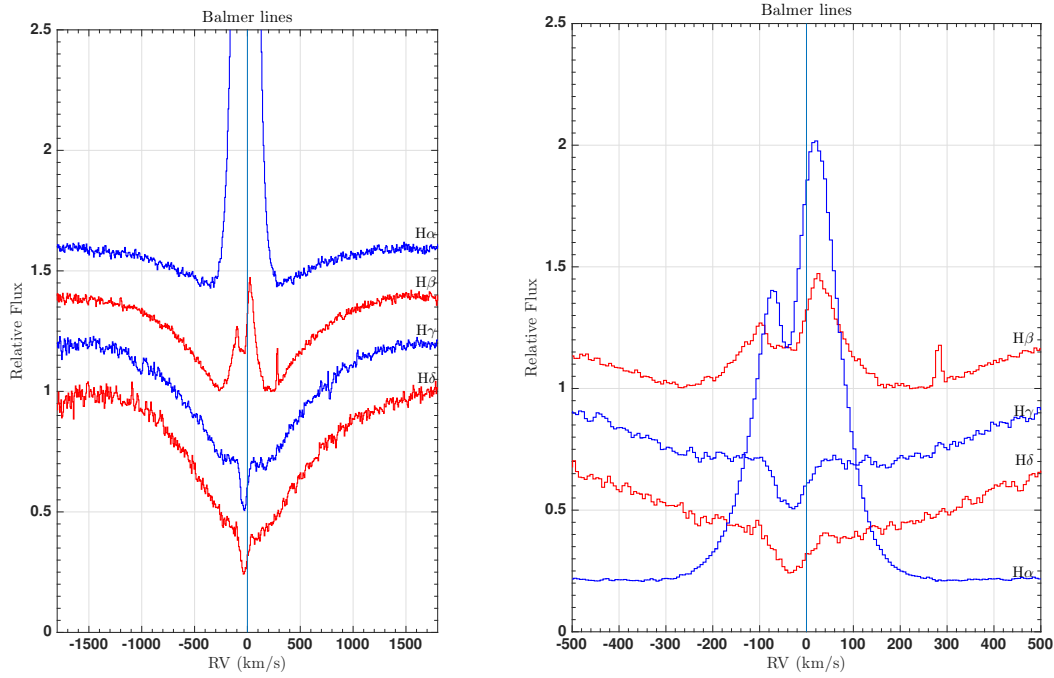
Figure 4.37: Line profile changes of the Balmer lines. Spectra taken from SPM2015 MJD= 7172.76. On the left the Balmer lines are plotted in the range $[-1800, 1800]$ km s^{-1}, on the right in the range $[-500, 500]$ km s^{-1}.
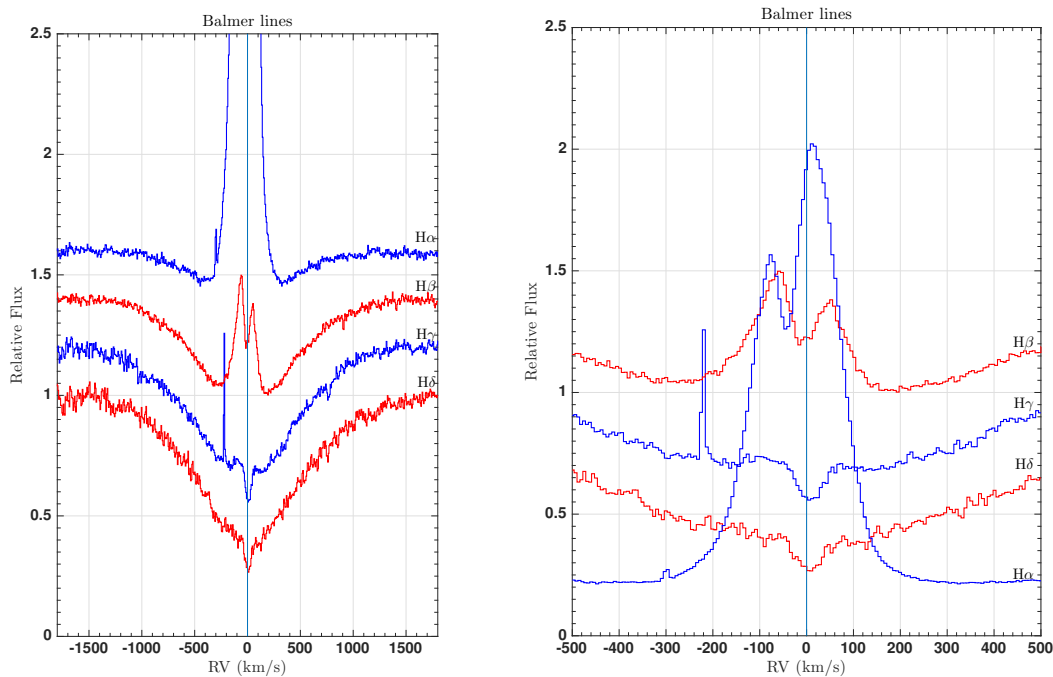
Figure 4.38: Line profile changes of the Balmer lines. Spectra taken from SPM2015 MJD= 7173.75. On the left the Balmer lines are plotted in the range $[-1800, 1800]$ km s^{-1}, on the right in the range $[-500, 500]$ km s^{-1}.
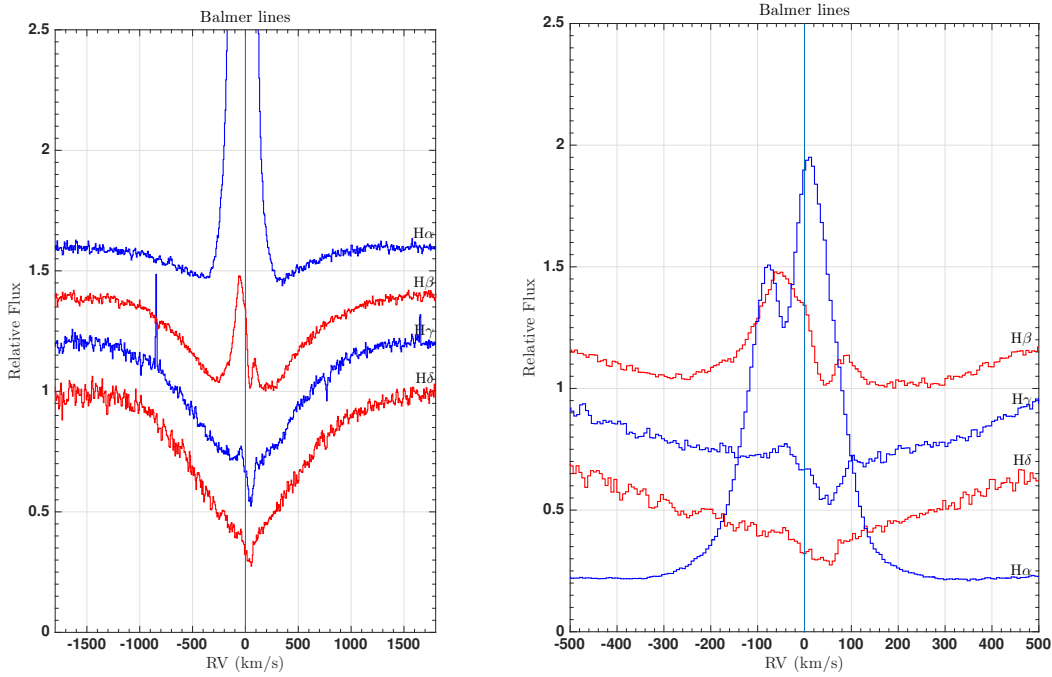
Figure 4.39: Line profile changes of the Balmer lines. Spectra taken from SPM2015 MJD= 7174.74. On the left the Balmer lines are plotted in the range $[-1800, 1800]$ km s^{-1}, on the right in the range $[-500, 500]$ km s^{-1}.
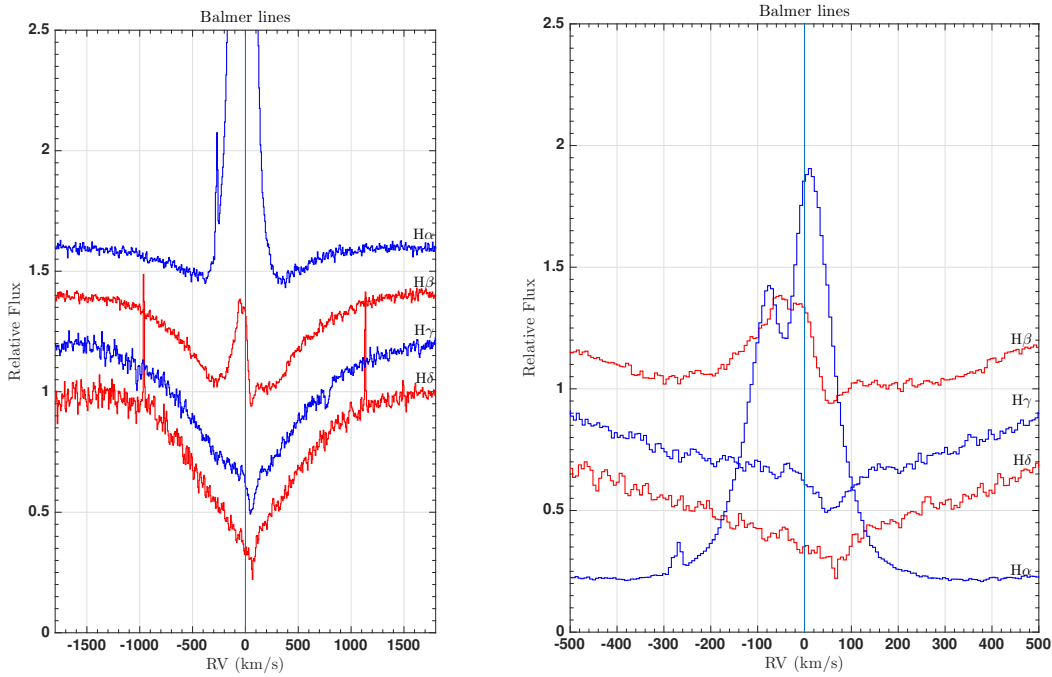
Figure 4.40: Line profile changes of the Balmer lines. Spectra taken from SPM2015 MJD= 7175.73. On the left the Balmer lines are plotted in the range $[-1800, 1800]$ km s^{-1}, on the right in the range $[-500, 500]$ km s^{-1}.
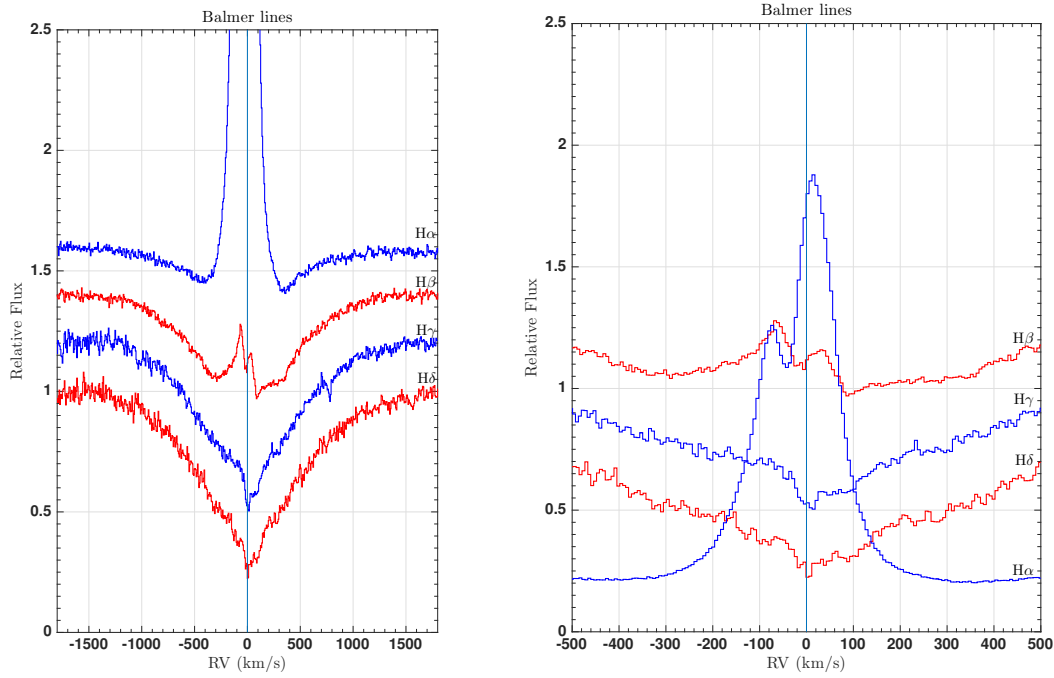
Figure 4.41: Line profile changes of the Balmer lines. Spectra taken from SPM2015 MJD= 7176.76. On the left the Balmer lines are plotted in the range $[-1800, 1800]$ km s^{-1}, on the right in the range $[-500, 500]$ km s^{-1}.
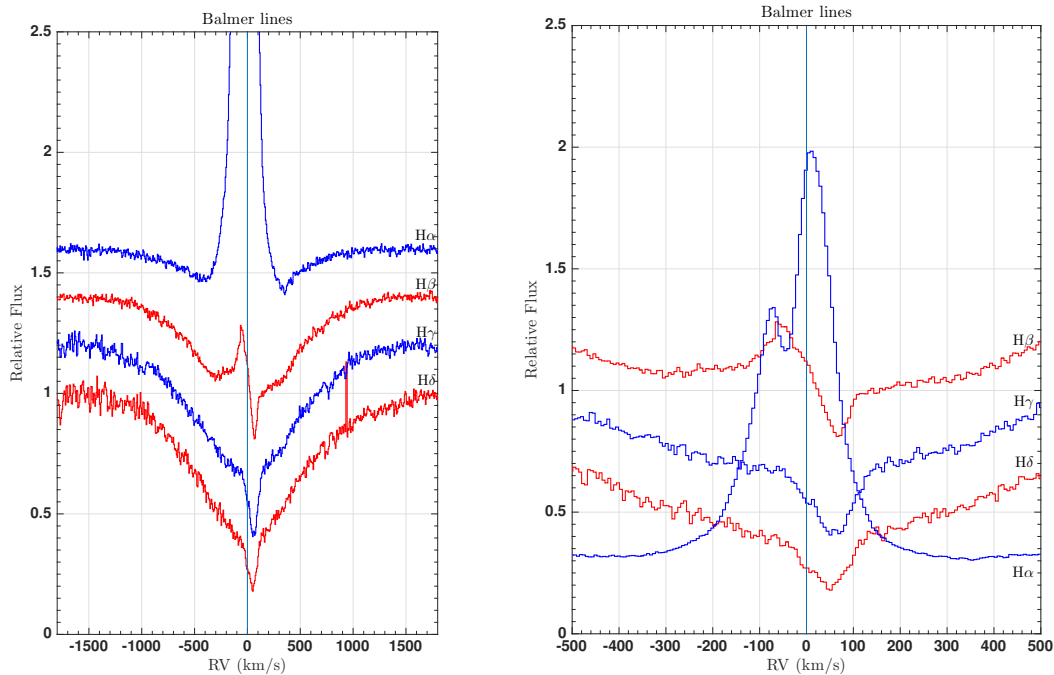
Figure 4.42: Line profile changes of the Balmer lines. Spectra taken from SPM2015 MJD= 7177.73. On the left the Balmer lines are plotted in the range $[-1800, 1800]$ km s^{-1}, on the right in the range $[-500, 500]$ km s^{-1}.

4.4.1.6 Comparison with β Leonis, an A-type star

It is evident that the Balmer line profile is changing, even on the timescale of days (SPM 2015). It is useful to show the difference between the Balmer lines of IRAS 17449 + 2320 and those of a reference star. In this way

we can eliminate the wings that likely arise from the photosphere and concentrate on the line core. Here I will show this comparison between the reference star and the SPM2015 case.

The Balmer lines in the spectral type range between B8V and A3V are stronger relative to the other spectral types. I have chosen an A3V star, β Leonis (also called Denebola). If IRAS $17449 + 2320$ is almost the same spectral type of Denebola, the photospheric part of the Balmer lines, so the wings, must be canceled in the subtraction of the spectra and this is very useful because the only remaining feature is the core of the lines and hence the part that varies in time. Figure 4.43 shows the variation of the Hα for all the spectra (on the left) and for the SPM spectra (on the right) day by day respect to β Leonis spectrum. In the same fashion, figure 4.44 shows respectively, on the left and on the right, the variation of the Hβ and Hγ lines day by day respect to β Leo spectrum. Unfortunately, the spectrum of β Leo does not cover the Hδ range. As shown, the core is the only feature that remains. Now we can understand better in which range of velocities the dynamical processes are playing a role and put constraint on the phenomena. Figures 4.43 and 4.44 show that this dynamical processe is confined to the velocity range $[-300, 300]$ km s^{-1} for all Balmer lines. For Hα from SPM 2015, there is change in the RV of the peaks of about 10 km s^{-1}, and in the V/R ratio (that I will analyze later). At Hβ and Hγ, there is a shift in the RV of the complex absorption components of about 150 km s^{-1}.
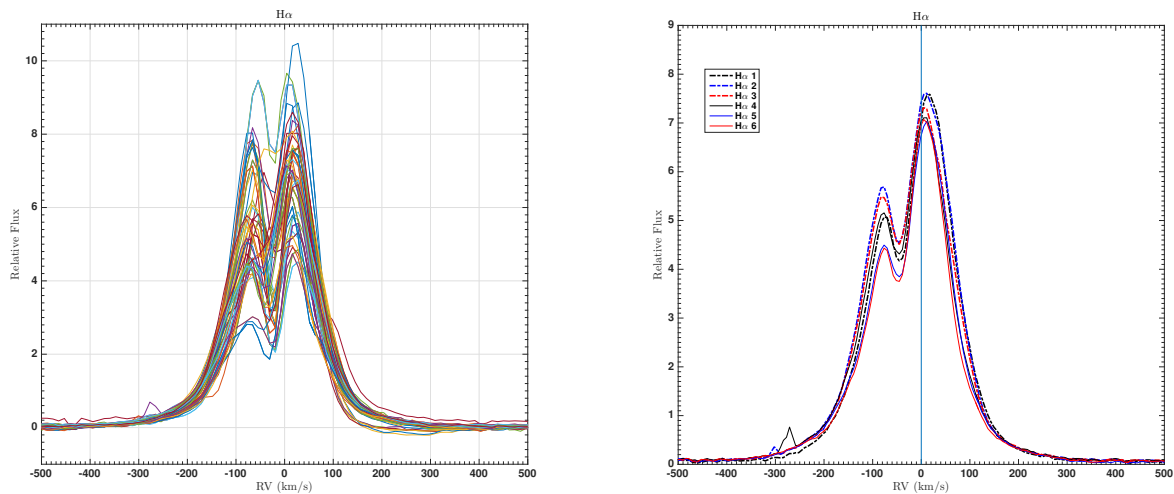
Figure 4.43: Hα variation. Left: Line profile variation for the Hα line for the spectra taken at CFHT, McDonald, SPM and Ondřejov telescopes. Right: Line profile variation for the Hα line for the spectra SPM2015.
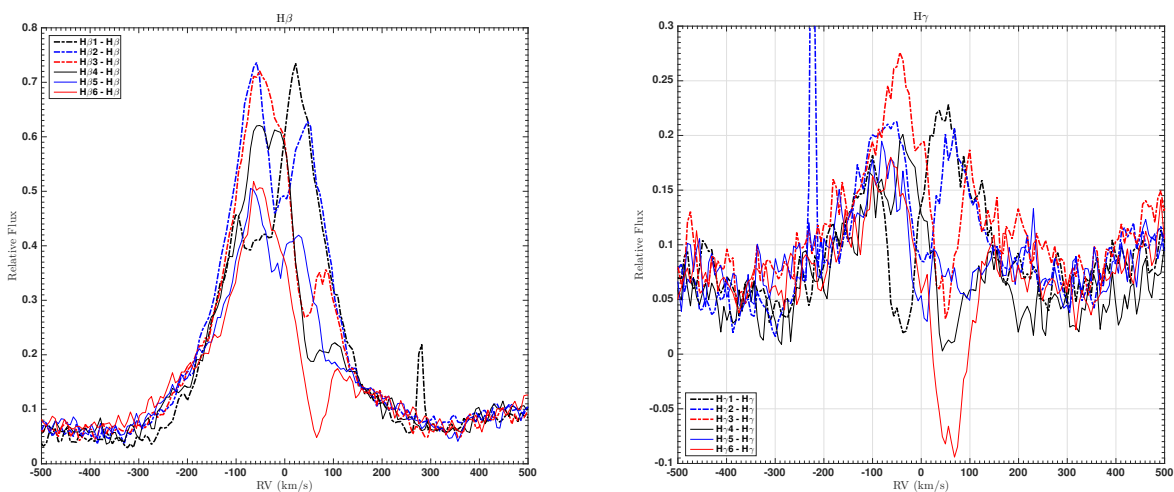
Figure 4.44: Hβ and Hγ. Left: Line profile variation for the Hβ line. Right: Line profile variation for the Hγ line. Spectra from SPM2015.

4.4.1.7 Balmer line ratio

Figures 4.45, 4.46 and 4.47 show the ratio between the Balmer lines (from Hβ to Hδ) and the Hβ line of β Leo for each day of SPM2015. This kind of plot is also useful for observing dynamical phenomena in the spectra. Note, in particular, how the composite absorption features inall lines are shifting similarly with a time scale of few days.
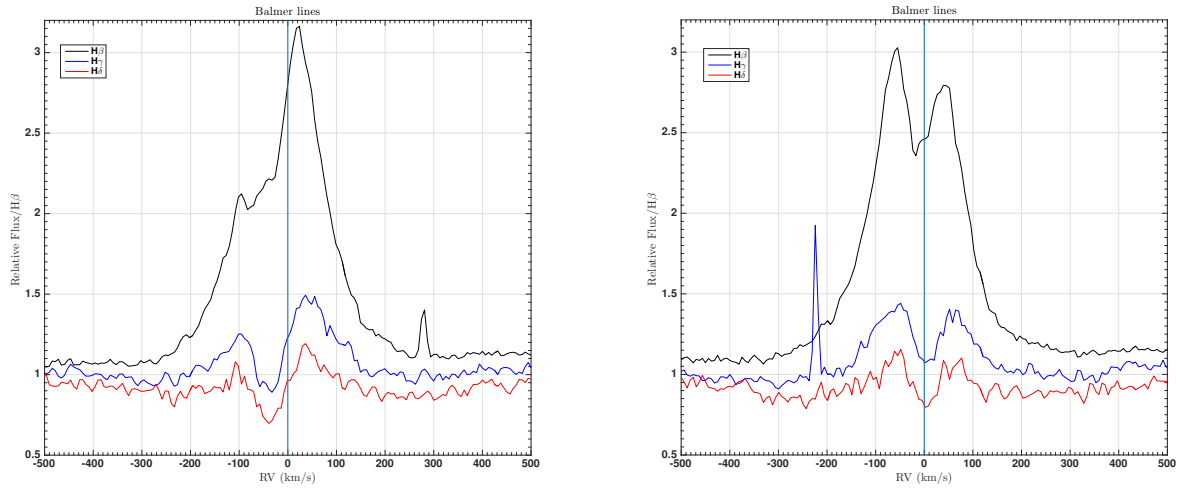
Figure 4.45: Balmer ratio. Left: Balmer line ratio for SPM2015 MJD= 7172.76. Right: Balmer line ratio for SPM2015 MJD= 7173.75.
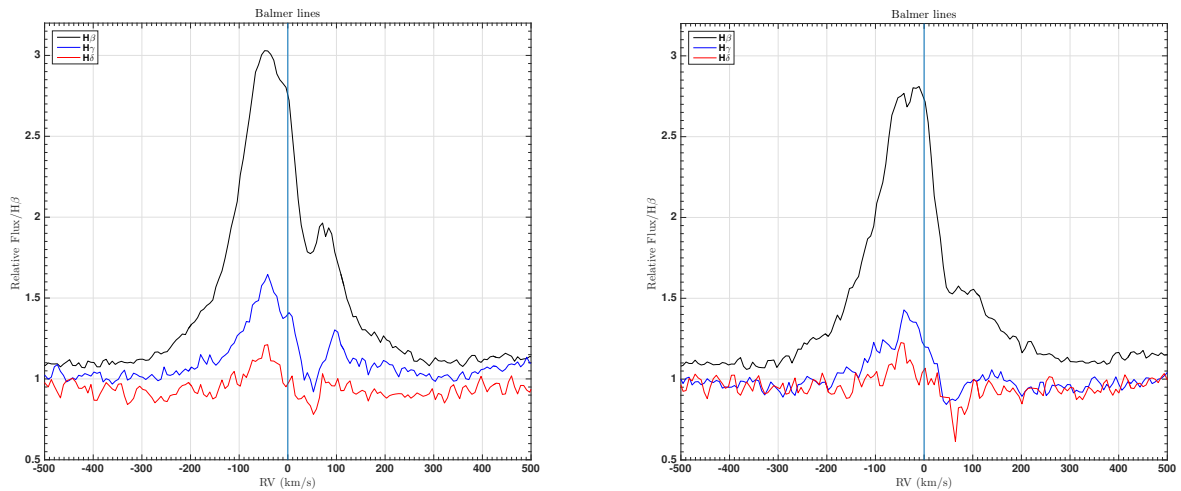
Figure 4.46: Balmer ratio. Left: Balmer line ratio for SPM2015 MJD= 7174.74 . Right: Balmer line ratio for SPM2015 MJD= 7175.73.
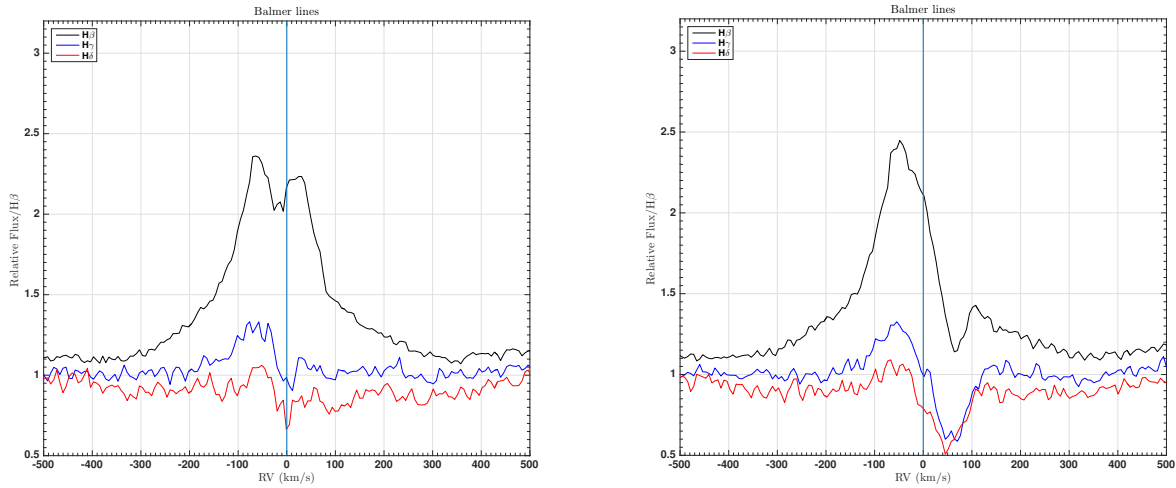
Figure 4.47: Balmer ratio. Left: Balmer line ratio for SPM2015 MJD= 7176.76. Right: Balmer line ratio for SPM2015 MJD= 7177.73.

4.4.1.8 V/R ratio for SPM spectra

To calculate the V/R ratio I subtracted the β Leo spectrum, interpolated all the spectra to the same resolution and binning, measured the signal to noise ratio (SN) choosing a region in the spectrum where there are no lines. I then measured the violet and the red peaks and the central depression manually in flux and velocity. Figure 4.48 shows the V/R variation in the SPM spectra. There is a significant variation during the SPM2015 sequence. Figure 4.49 shows the correlation between the V/R ratio and the central depression flux (residual depression) . The Pearson's r is 0.9755, a strong correlation. Figure 4.50 shows the correlation between the V/R ratio and the residual depression for the Ondřejov (blue numbered data) plus SPM2015 spectra (red data). Even if the Hα line does not vary as the other Balmer lines because of the dominant emission component, it is possible to see if something is happening through the correlation between the V/R ratio and the central residual depression. In the next paragraph (4.4.1.10) I will discuss this behaviour.
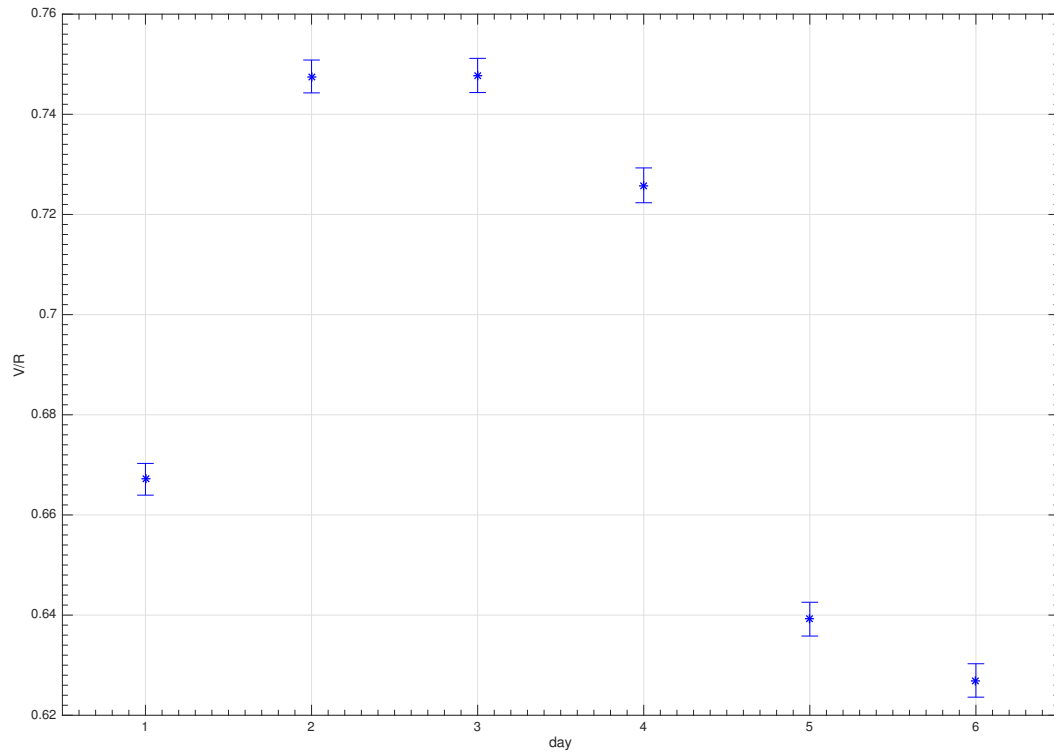
Figure 4.48: V/R ratio for the SPM2015 spectra.
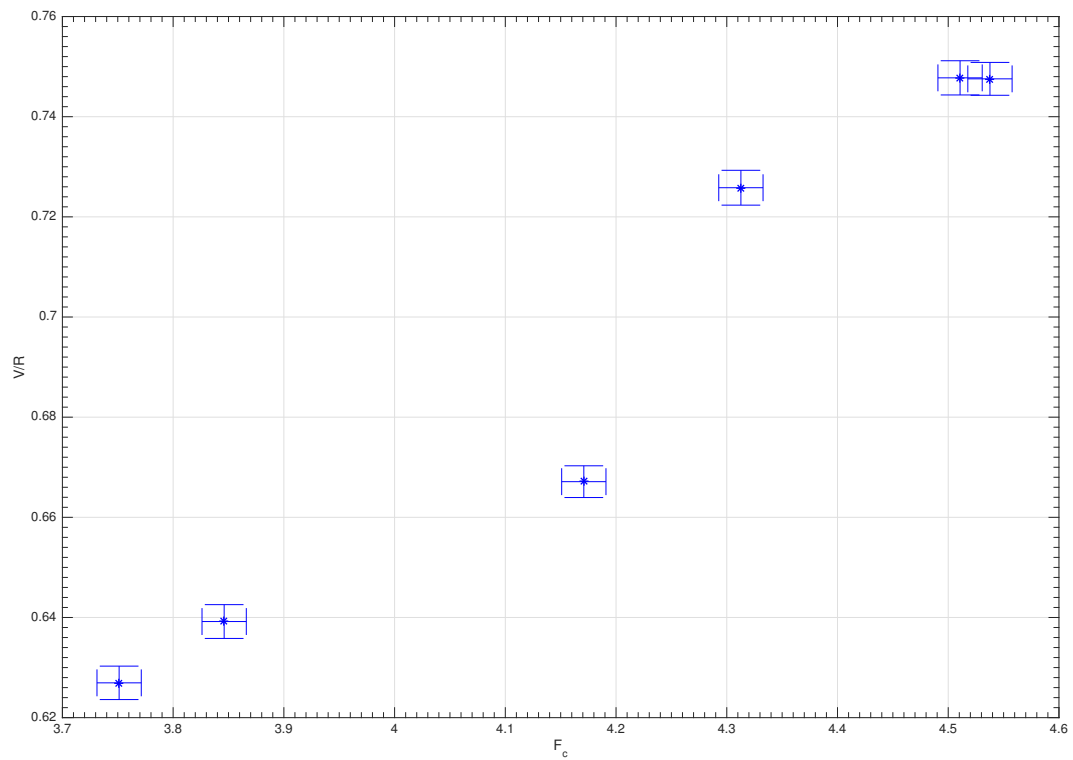
Figure 4.49: Correlation between the V/R ratio and the central depression flux for the SPM2015 spectra.

47
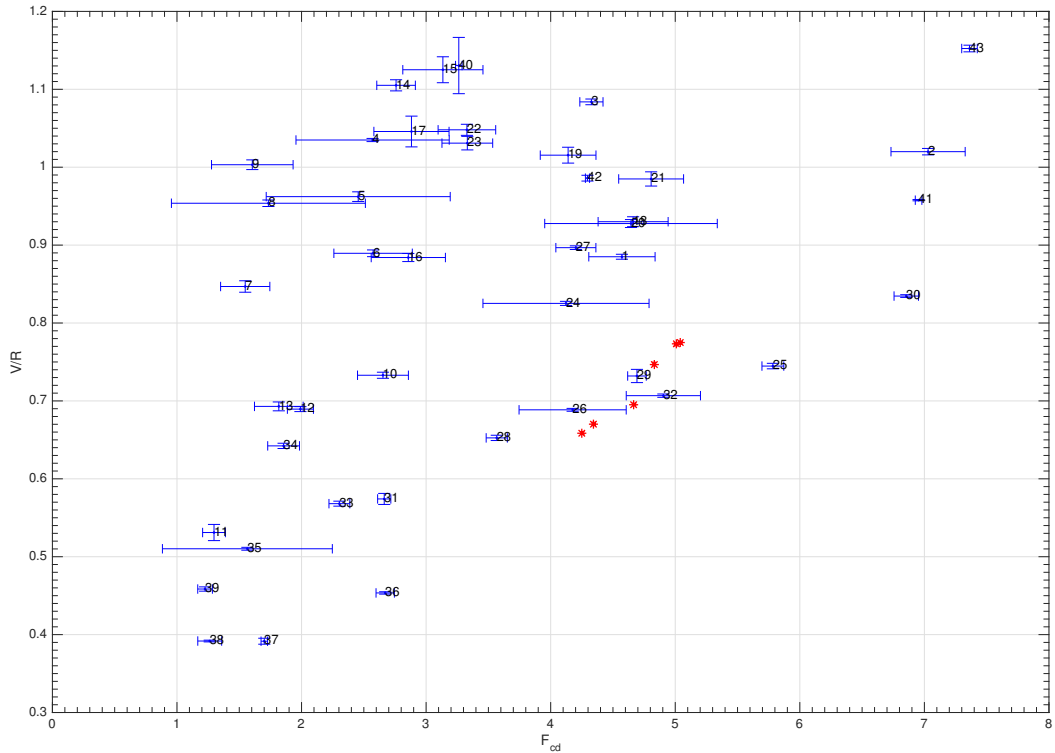
Figure 4.50: Correlation between the V/R ratio and the central depression flux for the Ondřejov and SPM spectra. Blue and numbered data are from Ondřejov, instead the red data are from SPM2015.

4.4.1.9   Comparison with Vega

Vega is oriented pole on toward us and appears to be a non rotatoring star ([22], [6], [23]). Convolving its spectra with a rotating line profile and comparing it with IRAS $17449 + 2320$, we can find how much the projected rotational velocity is for IRAS $17449 + 2320$. Figures 4.51 shows the Hα line profile of Vega with three different rotational velocity and 4.52 shows the comparison between the non rotated Vega and IRAS $17449 + 2320$ as regard Hβ lines. The Balmer lines wings of IRAS $17449 + 2320$ are well matched by a rotated Vega profile by 200 km s^{-1}. Hence the star is a fast rotator and the wings of the Balmer lines are formed in the photosphere.
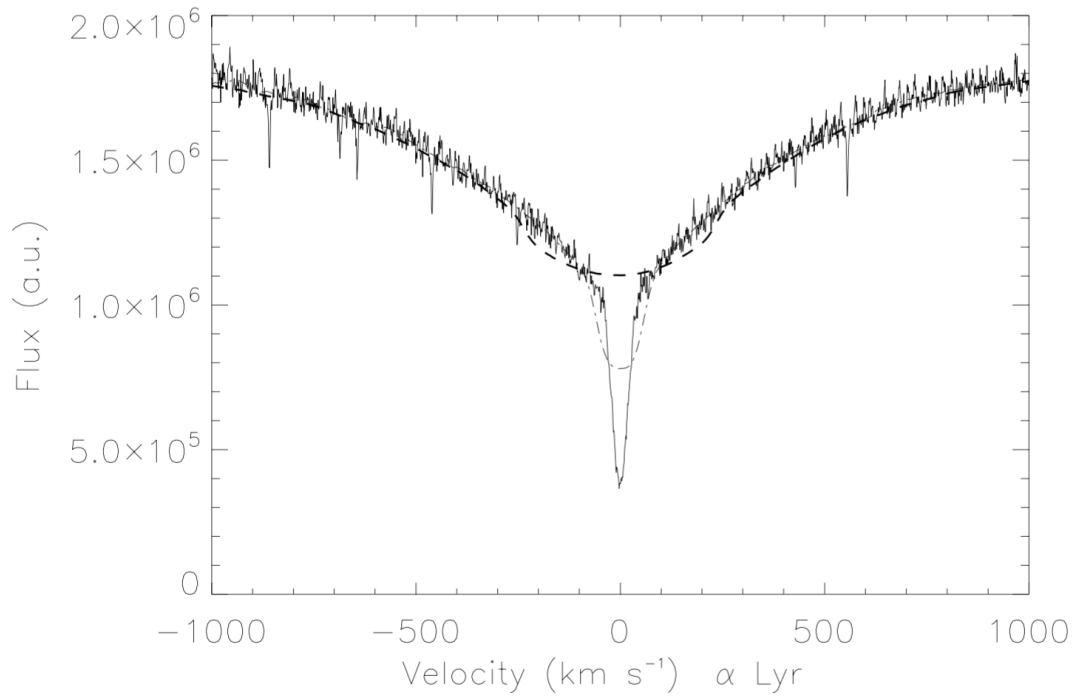
Figure 4.51: Comparison between the profile of non rotated Vega (solid line), rotated Vega by 50 km s^{-1} (dot-dashed line) and rotated Vega by 200 km s^{-1} (dashed line). The line is the Hα. Spectrum from ESO.
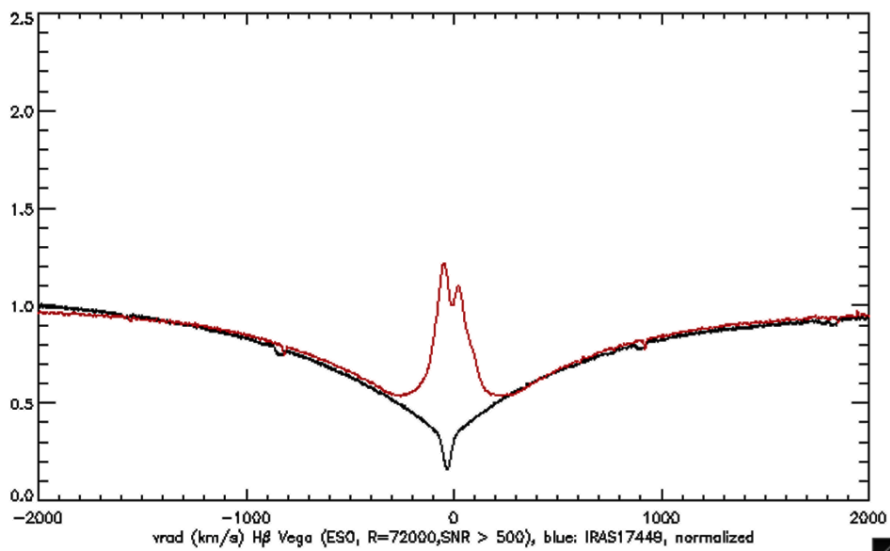
Figure 4.52: Comparison between Vega and IRAS 17449 + 2320 for Hβ.

4.4.1.10   Observations and Summary on Balmer lines

Considering only the SPM2015 spectra, so from figure 4.37 to 4.42, it is clear that there are two absorption features present in the Hβ, Hγ and Hδ lines that are moving from the blue to the red side of the line, with a timescales of days and a change in RV of order of 150 km s^{-1}. For the first two days there is only one absorption feature, but on the third and the fourth day of SPM observations, a second absorption feature appears at the same time as the disappearance of the first. For Hβ, the two absorption features are not blended, but for Hγ and Hδ, they are blended and produce a broader absorption feature. The absorption features and their shift can be explained by the presence of a transient coherent structure that, moving around the central object, changes the optical depth.

For Hα line (figure 4.30), in contrast to the other Balmer lines, the absorption feature does not change its velocity as much. The only thing that changes day by day is the V/R ratio as we can see in figures 4.7 and 4.48 respectively for Ondřejov spectra and SPM spectra.

For Hβ while the first feature is shifting toward the red side, the V/R ratio increases, then when the second feature appears the V/R ratio decreases. This is consistent with an orbiting coherent structure, but because the emission is dominant in Hα, the variation of V/R is smaller.

Returning on Hα, its profile can be approximated roughly as $\phi(\lambda)e^{-\tau_\lambda}$ with $\tau_\lambda \approx \tau_0 \phi(\lambda \pm \Delta\lambda)$ and so when the transient coherent structure moves, the optical depth changes. If τ_λ increases, the central depression residual decreases but also the violet peak and hence the V/R ratio. This can be explain the strong correlation between V/R and the central depression residual.

The complete data set, figure 4.50, does not show the same correlation on longer timescales. It seems there are at least two groups: one that shows the same correlation as in SPM data and one that does not. This could be explained assuming the absorber is a stochastic structure or having a recurrence timescale that is only poor sampled.

Looking also at other lines such as [O I] (figure 4.57), that it is in emission, it is clear the presence of an extended low density structure around the star. The presence of the self absorption feature combined with the presence of other absorption lines, that we will investigate later, are an evidence of a denser region, that is a disk.

The comparison of the Balmer lines from IRAS 17449 + 2320 and a rotated Vega spectrum suggests the star has a projected rotational velocity of about 200 km s^{-1}, hence it is a fast rotator.

4.4.2   Paschen lines

Other than Balmer lines, IRAS 17449+2320 has Paschen lines. As shown in table 4.1, I found Paschen lines from P8 to P16. These lines are indicator that the star is in main sequence. Figure 4.53 shows the velocity line profile of Paschen $8-16$. They are in absorption with the core weakly in emission. The higher the Paschen transition, the smaller the residual respect the continuum. The wings are contaminated by atmospheric absorption lines.
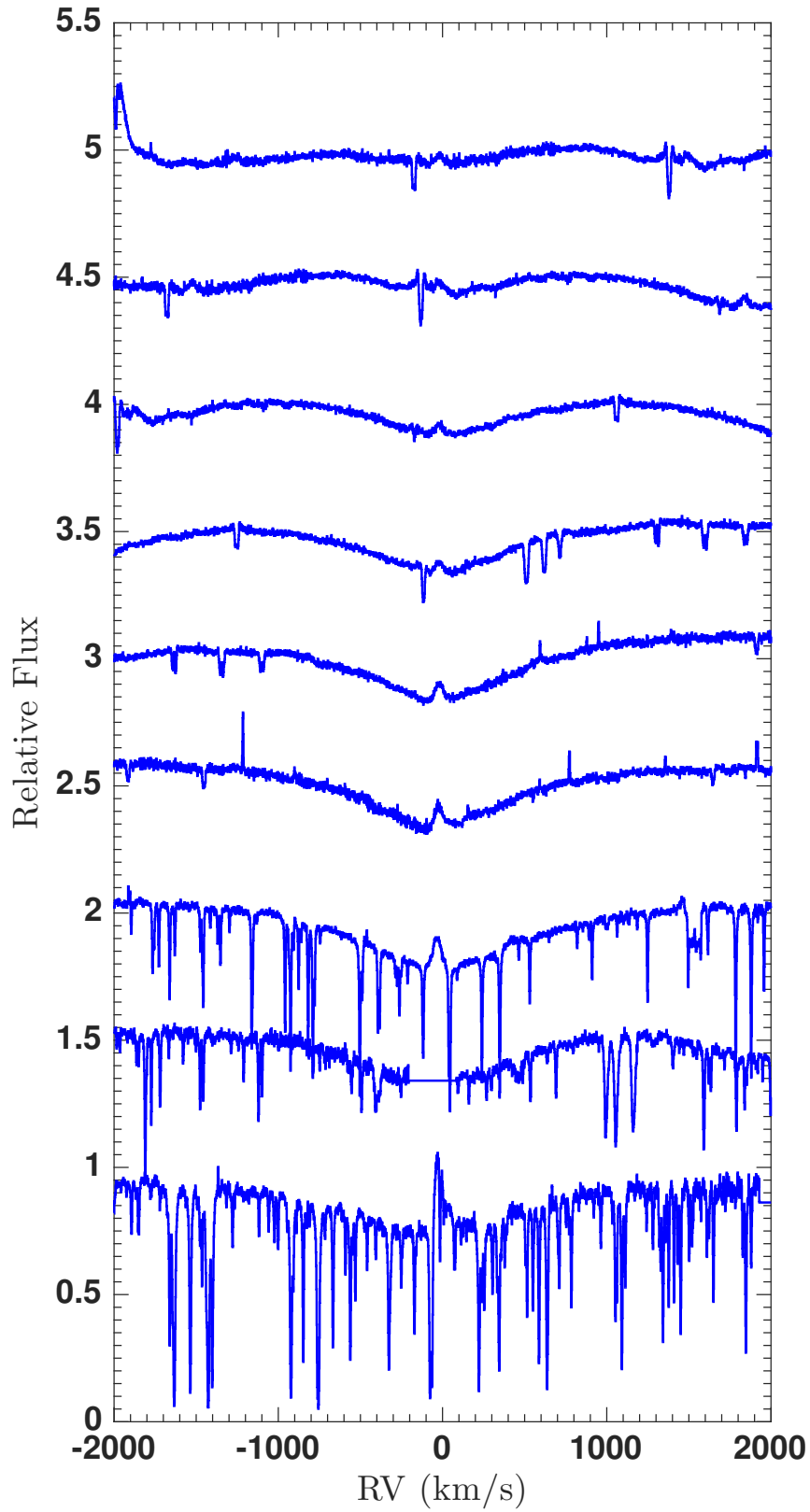
Figure 4.53: Paschen lines. Velocity line profile from P8 (bottom line) to P16 (upper line). Lines taken from CFHT spectrum with MJD= 4284.60. P9 has a discontinuity due to a gap between the orders in CFHT spectrograph.

4.4.3   He I

Photospheric He I is a good indicator of the spectral type of the object ([20]). The presence of He I and the absence of He II implies a late B-type star. The weaker the He I the later the type. I found trace of He I in absorption (see table 4.1) in IRAS $17449 + 2320$ but these lines are very weak, consistent with a late B-type star and not an A0V as proposed by Miroshnichenko ([52]). One of the He I lines found is the 4471.480Å absorption line comes from the transition between the $^3P^o$ level with energy $E_l = 20.964eV$ and the ^3D level with energy $E_u = 23.736eV$. The multiplet is the number 14. Figure 4.54 shows its velocity line profile from the CFHT spectra. SPM spectra are not reported in the plot because their spectra are too noisy in this spectral region. The line shape is asymmetric with a steeper blue side. This line is composed by transitions between different upper and lower sublevels and a different lifetime can explain the asymmetry. Table 4.4 gives the equivalent width and radial velocity from the CFHT.

MJD	EW$_\lambda$ (mÅ)	RV (km s^{-1})
4284.60	65.1 $\pm$ 13.8	-15.1 $\pm$ 1.0
4671.60	80.2 $\pm$ 13.6	-14.9 $\pm$ 0.9

Table 4.4: EW$_\lambda$ and radial velocity of He I 4471.480Å line.

The mean radial velocity is RV$= (-15.0 \pm 1.3)$km s^{-1}. Although the EW$_\lambda$ is the same within the errors, from figure 4.54, the absorption on MJD$= 4671.6$ seems to be stronger. This is not a resolution effect but a real change in the line profile, as we will see in paragraph 4.4.11.
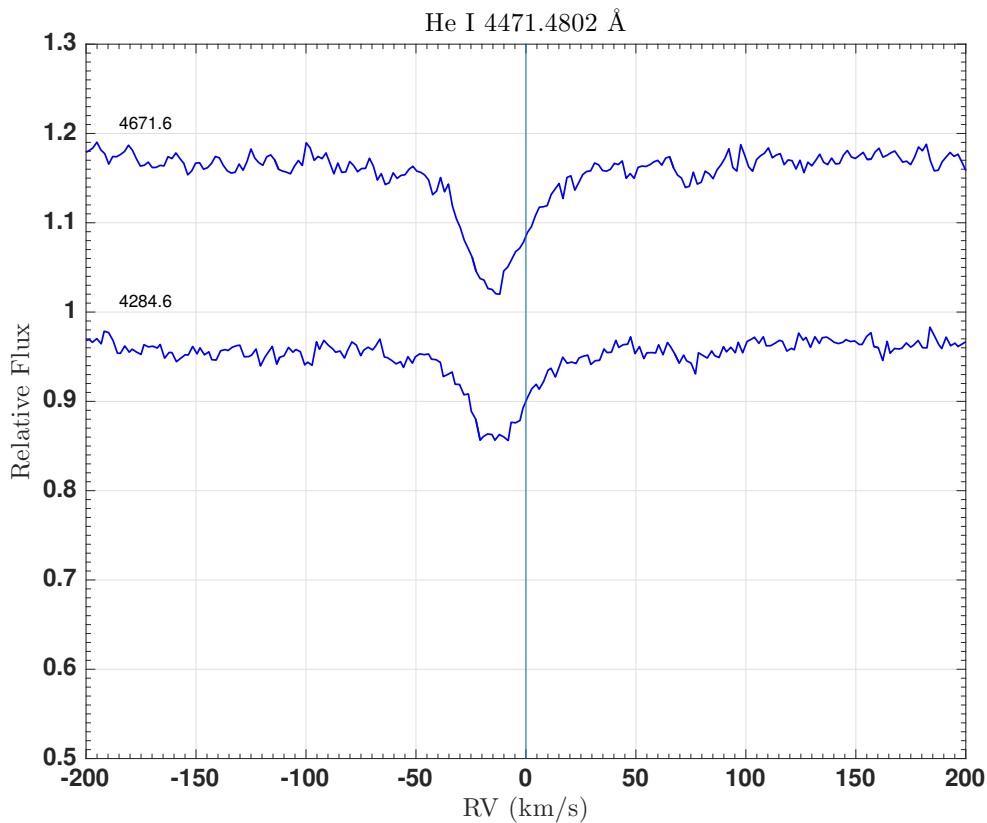
Figure 4.54: He I 4471.480Å: line profile variability. Spectra taken from the observatories of CFHT. The number on each spectrum is the MJD.

The second He I line is the 5875.621Å that comes from the transition between a $^3P^o$ level with energy $E_l = 20.964eV$ and a ^3D level with energy $E_u = 23.074eV$. The multiplet number is 11. The velocity line profiles from McDonald, CFHT and San Pedro Martir are shown in figure 4.55. The line has an asymmetric line profile, like He I 4471.480Å for the same reason. Table 4.5 gives the equivalent widths and the radial velocities from CFHT, SPM and McDonald. The velocity is almost constant in the error, the mean radial velocity is RV= (15.8 ± 1.9) km s^{-1}. The EW$_\lambda$ seems to vary during the observations, as does the line shape. In particular, the He I 5875.621Å taken at MJD= 4671.60 is stronger in absorption than the others, like He I 4471.480Å.

MJD	EW$_\lambda$ (mÅ)	RV (km s^{-1})
3895.60	85.7 ± 9.9	-16.1 ± 0.8
4284.60	71.1 ± 11.0	-15.7 ± 1.0
4671.60	126.0 ± 16.7	-15.1 ± 0.9
5080.63	46.5 ± 10.4	-13.5 ± 1.2
7172.76	46.7 ± 12.5	-14.4 ± 3.1
7173.75	72.6 ± 17.6	-18.9 ± 3.1
7174.74	64.4 ± 15.4	-17.5 ± 3.1
7175.73	76.5 ± 17.4	-18.5 ± 3.1
7176.76	60.3 ± 14.6	-13.9 ± 3.1
7177.73	64.3 ± 14.8	-14.2 ± 3.1

Table 4.5: EW$_\lambda$ and radial velocity of He I 5875.621Å line.
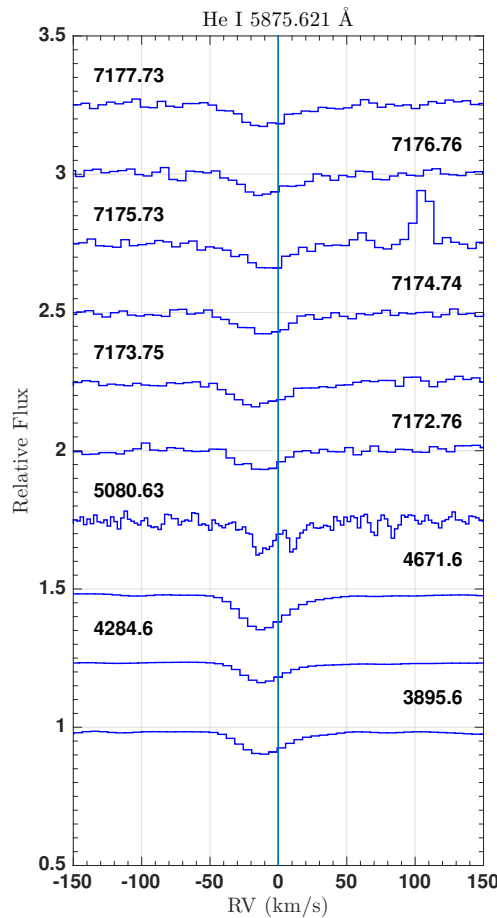
Figure 4.55: He I 5875.621Å: line profile variability. Spectra taken from the observatories of McDonald, CFHT and San Pedro Martir. The number on each spectrum is the MJD.

The He I 6678.149Å absorption line comes from the transition between the $^1P_1^o$ level with energy $E_l = 21.218eV$ and the $^1D_2$ level with energy $E_u = 23.074eV$. The multiplet is the number 46. Figure 4.56 shows the velocity line profile of He I 6678.149Å taken from the CFHT spectra. SPM spectra are not reported in the plot because their spectra are too noisy in the line region. The line appears in absorption and centered at RV$= (-15.3 \pm 0.8)$ km s^{-1}. Table 4.6 gives the equivalent widths and the radial velocities from CFHT. The EW$_\lambda$ seems to vary in the period of observations, and also the line shape. In particular, the He I 5875.621Å taken at MJD$= 4671.60$ is stronger in absorption than the others.

MJD	EW$_\lambda$ (mÅ)	RV (km s^{-1})
3895.60	15.2 ± 3.1	-16.1 $\pm$ 1.0
4284.60	12.0 ± 2.1	-14.7 $\pm$ 0.9
4671.60	25.4 ± 5.0	-15.1 $\pm$ 0.9

Table 4.6: EW$_\lambda$ and radial velocity of He I 6678.149Å line.
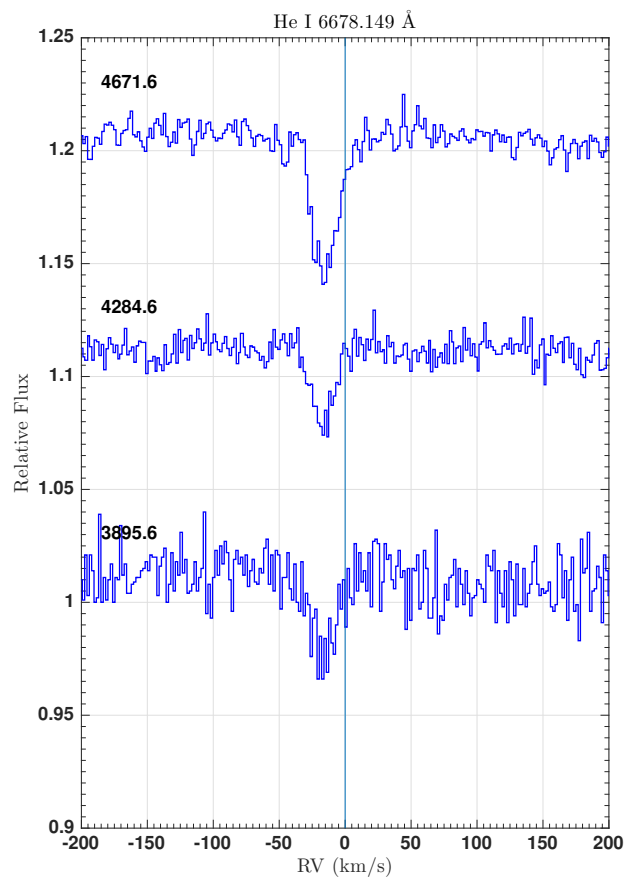
Figure 4.56: He I 6678.149Å: line profile variability. Spectra taken from the observatories of CFHT. The number on each spectrum is the MJD.

4.4.4   O I

O I lines are good physical indicators of the circumstellar envelope's conditions. The first ionization potential of O I is $E_{O,ion} = 13.618$ eV, very close to H I $E_{H,ion} = 13.598$ eV. The presence of [O I] emission lines tells us that the envelope where this line is forming is a low density region. Finding and studying the presence of various O I emission lines, it is possible to reconstruct with Grotrian diagrams which is the main line that pumps the O I system and hence take informations about the radiation field (see figure 4.60).

The first lines identified as O I are the [O I] $\lambda\lambda$ 6300.304, 6363.776Å. Their velocity line profile taken from the spectra of the observatories of CFHT and San Pedro Martir are shown in figure 4.57. As we can see, both lines are in emission and peaked at RV= (-16 ± 2) km s^{-1}. These lines, in particular the 6363.776Å, are not strong and so they could be affected by the noise and produce a false small variability.

Table 4.7 shows the EW$_\lambda$ and the RV for [O I] $\lambda\lambda$ 6300.304, 6363.776Å lines.
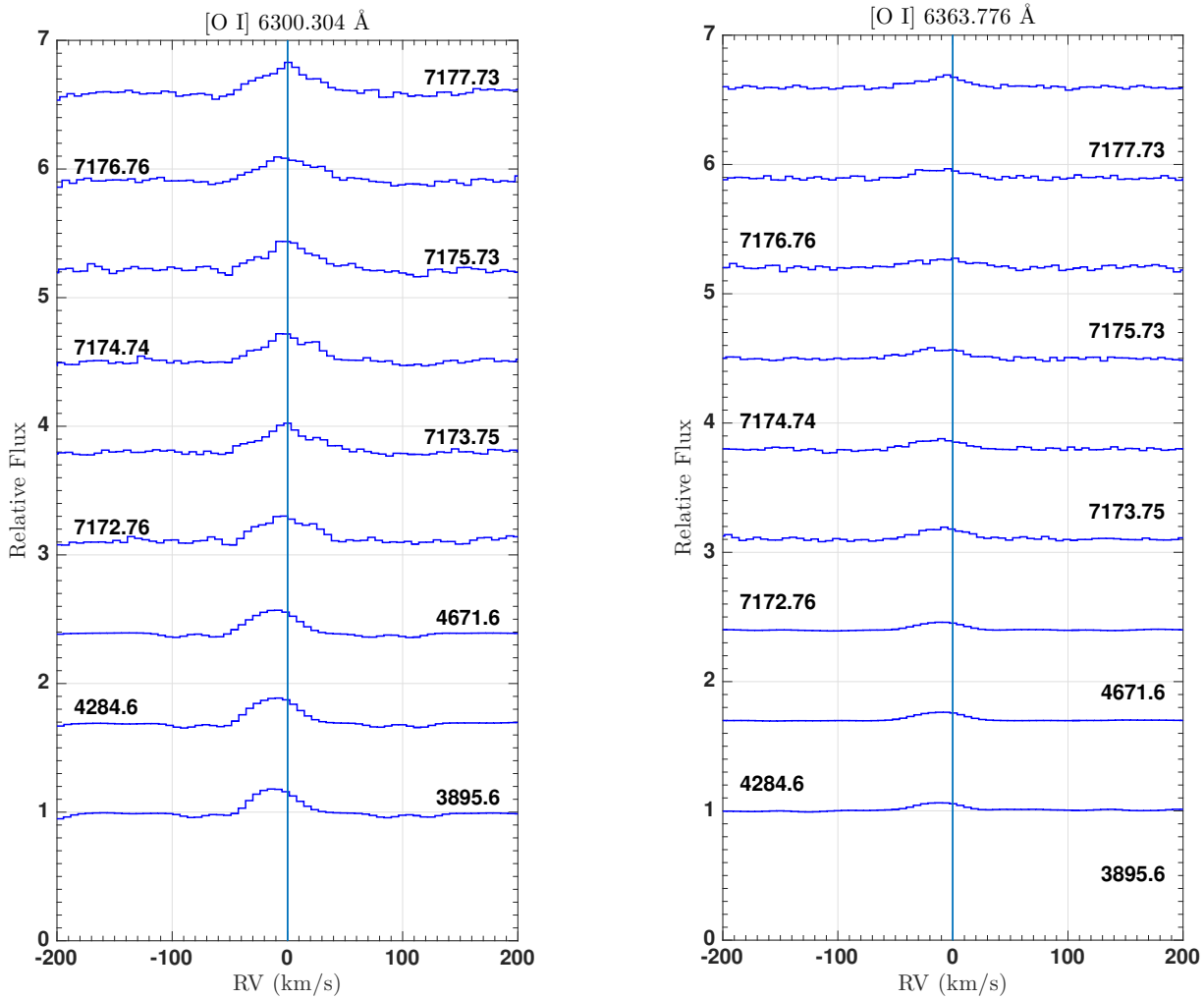
Figure 4.57: [O I] $\lambda\lambda$ 6300.304, 6363.776Å: line profile variability. Spectra taken from the observatories of CFHT and San Pedro Martir. The number on each spectrum is the MJD.

MJD	EW$_{6300}$ (mÅ)	EW$_{6364}$ (mÅ)	RV$_{6300}$ (km s^{-1})	RV$_{6364}$ (km s^{-1})
4603.44	-162.5± 65.9	-60.1 ± 47.9	-11.6 ± 4.4	-18.4 ± 9.4
4940.44	-140.7 ± 82.5	-87.3 ± 97.5	-5.1 ± 6.8	-21.4 ± 19.9
5616.64	-119.4 ± 27.4	-31.0 ± 21.0	-14.3 ± 3.0	-9.3 ± 9.4
5618.59	-119.1 ± 34.0	-61.4 ± 17.0	-13.3 ± 3.1	-17.7 ± 6.4
5642.61	-123.9 ± 34.1	-79.4 ± 33.2	-10.9 ± 3.3	-29.8 ± 16.5
5662.51	-144.2 ± 41.4	-62.9 ± 36.7	-9.5 ± 3.4	-8.1 ± 13.0
5671.55	-135.3 ± 25.7	-69.4 ± 19.7	-11.9 ± 2.1	-23.2 ± 5.6
5674.44	-131.8 ± 24.7	-68.5 ± 20.1	-11.2 ± 1.7	-15.0 ± 4.2
5688.59	-135.8 ± 46.5	-36.7 ± 11.5	-14.9 ± 3.1	-3.4 ± 5.82
5808.44	-170.4 ± 45.0	-74.7 ± 18.1	-13.0 ± 2.2	-14.8 ± 4.1
5839.36	-196.0 ± 41.1	-85.1 ± 26.7	-11.5 ± 2.5	-14.8 ± 6.6
6011.61	-122.0 ± 50.0	-65.7 ± 25.1	-12.1 ± 5.5	-9.5 ± 10.7
6012.54	-88.47 ± 51.0	-40.6 ± 32.0	-9.08 ± 6.5	3.2 ± 14.5
6132.3	-192.1 ± 29.1	-79.9 ± 21.6	-14.3 ± 1.7	-14.6 ± 4.7
6135.40	-189.7 ± 41.4	-65.9 ± 31.1	-14.4 ± 2.0	-18.0 ± 8.2
6154.35	-181.3 ± 32.9	-81.0 ± 29.3	-10.9 ± 2.1	-17.1 ± 7.3
6158.36	-189.4 ± 28.5	-57.3 ± 22.0	-10.2 ± 3.2	-16.1 ± 5.8
6187.34	-187.8 ± 45.9	-56.6 ± 60.9	-11.9 ± 2.5	-13.0 ± 7.9
6400.49	-129.8 ± 47.2	-67.0 ± 46.1	-10.4 ± 3.6	-14.4 ± 13.8
6406.46	-122.4 ± 45.3	-80.8 ± 40.0	-8.5 ± 3.9	-18.2 ± 8.0
6421.40	-146.4 ± 44.6	-81.2 ± 22.5	-12.0 ± 3.2	-12.5 ± 4.6
6428.42	-154.2 ± 34.7	-55.5 ± 38.48	-12.9 ± 3.5	-25.1 ± 11.6
6457.45	-171.5 ± 22.3	-67.0 ± 30.0	-12.0 ± 2.1	-18.4 ± 6.17
6489.42	-151.1 ± 29.8	-50.0 ± 25.5	-13.4 ± 2.7	-8.87 ± 5.8
6521.41	-177.3 ± 29.4	-65.8 ± 22.6	-13.5 ± 2.0	-15.4 ± 6.9
6572.31	-173.5 ± 25.8	-64.9 ± 23.0	-11.1 ± 2.0	-14.7 ± 5.8
6592.24	-147.7 ± 34.3	-53.7 ± 12.9	-8.4 ± 2.7	-1.9 ± 4.8
6712.57	-112.9 ± 20.1	-52.9 ± 23.6	-11.1 ± 3.6	-23.9 ± 6.2
6718.63	-106.1 ± 39.1	-52.9 ± 19.7	-14.3 ± 3.1	-17.1 ± 7.3
6817.47	-149.1 ± 22.3	-62.3 ± 15.1	-14.9 ± 2.1	-21.5 ± 4.9
6854.40	-173.8 ± 35.5	-52.8 ± 38.0	-13.2 ± 2.3	-24.6 ± 10.6
6856.41	-197.2 ± 21.6	-55.6 ± 20.6	-15.4 ± 2.1	-14.7 ± 7.5
6861.44	-191.9 ± 46.3	-54.0 ± 43.9	-12.3 ± 3.0	-15.4 ± 10.9
6878.36	-186.6 ± 22.1	-65.3 ± 20.9	-15.5 ± 1.5	-10.4 ± 5.13
6900.36	-177.9 ± 24.5	-76.3 ± 25.2	-15.2 ± 2.1	-15.3 ± 5.6
6950.23	-147.5 ± 35.7	-48.1 ± 29.1	-11.5 ± 2.4	-8.0 ± 8.1
7172.76	-205.1 ± 48.5	-89.4 ± 19.7	-17.5 ± 3.1	-16.7 ± 3.1
7173.75	-225.3 ± 45.0	-74.0 ± 16.6	-0.2 ± 3.2	-10.3 ± 3.1
7174.74	-235.3 ± 48.1	-83.8 ± 17.7	-0.8 ± 3.2	-15.9 ± 3.1
7175.73	-272.8 ± 52.7	-91.1 ± 17.8	-2.4 ± 3.1	-10.7 ± 3.1
7176.76	-229.1 ± 45.7	-59.8 ± 14.2	-5.1 ± 3.2	-10.7 ± 3.1
7177.73	-198.5 ± 44.5	-75.6 ± 17.3	-11.0 ± 3.2	-17.5 ± 3.1

Table 4.7: EW$_\lambda$ and radial velocity of [O I] $\lambda\lambda$ 6300.304, 6363.776Å lines

Other O I lines founded are the triplet $\lambda\lambda$ 7771.96, 7774.18, 7775.4Å thatcome from the transition between the singlet state $^5S_2^o$ with energy $E_l = 9.146eV$ and the triplet level ^5P that has three sublevels, i.e. the $^5P_3$ with energy $E_u = 10.741eV$, the $^5P_2$ with energy $E_u = 10.740(5)eV$ and the $^5P_1$ with energy $E_u = 10.740(2)eV$. the multiplet is the number 1.

Figure 4.58 shows the velocity line profiles of the O I $\lambda\lambda$ 7771.96, 7774.18, 7775.4Å lines from the spectra of the CFHT. The structure of these lines is composite, it is mainly in emission with absorption features due to self absorption by the three lines. The self absorption components of these lines are peaked at RV≈ -15 km s^{-1}.
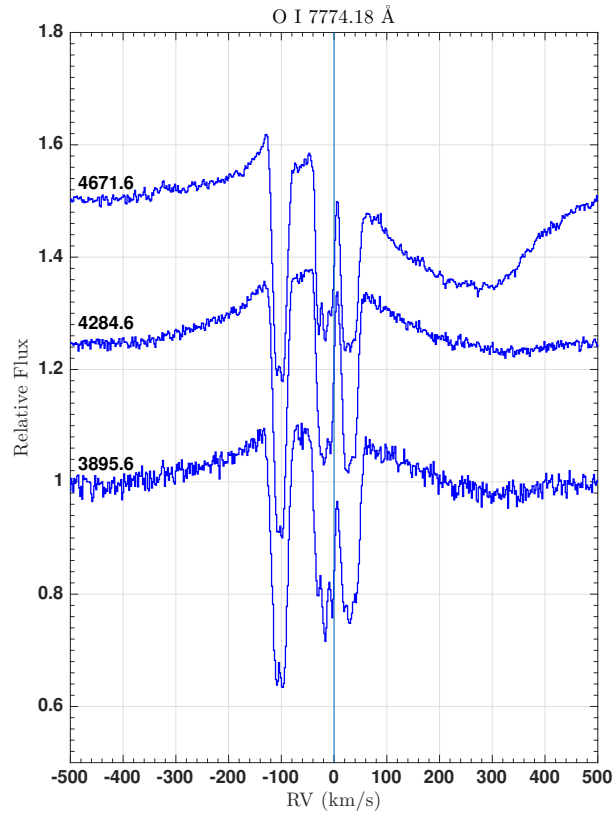
Figure 4.58: O I $\lambda\lambda$ 7771.96, 7774.18, 7775.4Å: line profile varibility. RV is referred to O I 7774.18Å. Spectra taken from the observatories of CFHT. The number on each spectrum is the MJD.

Another O I triplet is present in the spectrum and it is the $\lambda\lambda$ 8446.25, 8446.36, 8446.76Å lines come from the transitions between the singlet state $^3S^o_1$ with energy $E_l = 9.521eV$ and the triplet ^3P that has three sublevels, i.e. the $^3P_0$ with energy $E_u = 10.988(88)eV$, the $^3P_2$ with energy $E_u = 10.988(86)eV$ and the $^3P_1$ with energy $E_u = 10.988(79)eV$. The multiplet is the number 4. Figure 4.59 shows the velocity line profiles of the O I $\lambda\lambda$ 8446.25, 8446.36, 8446.76Å lines from the spectra of the CFHT. As we can see, the triplet has a complex structure composed by an overall emission plus self absorptions due to the triplet itself.
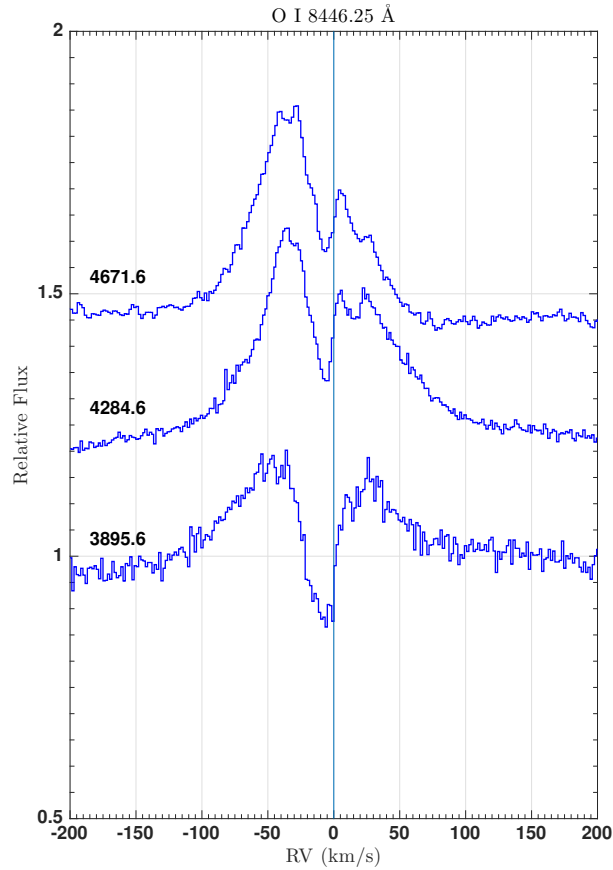
Figure 4.59: O I $\lambda\lambda$ 8446.25, 8446.36, 8446.76: line profile variability. RV is referred to O I 8446.25Å. Spectra taken from the observatories of CFHT. The number on each spectrum is the MJD.

Figure 4.60 shows the Grotrian diagram for O I useful for understand which line is pumping the system. The presence of the previous O I lines means that they could be pumped by the radiative decay of the $^3D^o$ level, which is created by the absorption of photons in the UV with wavelength $\lambda = 1025.762$Å, also justify by the absence of O I $\lambda\lambda5577,4368$Å. Unfortunately my spectra do not cover the UV range.
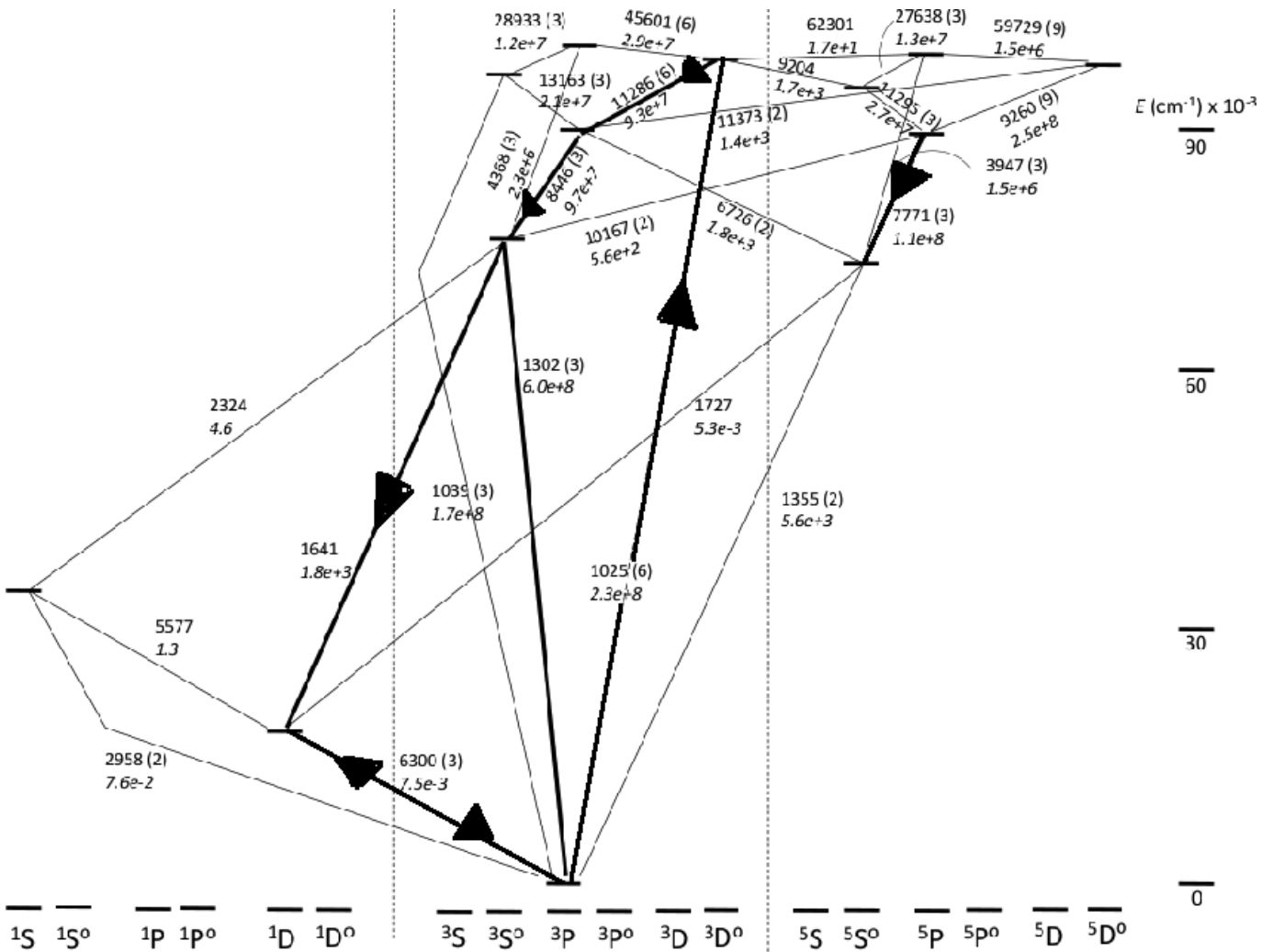
Figure 4.60: The Grotrian diagram for O I. For each transition the wavelength in Å and the A_{ij} coefficients are indicated. On the right column and on the bottom line, the energy level (in cm^{-1}) and the electronic configuration in spectroscopic notation are shown. Figure from [73].

4.4.5 Mg II 4481.129Å

The Mg II 4481.129Å absorption line comes from the transition between a $^2D_{5/2}$ level with energy $E_l = 8.864eV$ and a $^2F_{7/2}$ level with energy $E_u = 11.630eV$. The multiplet is the number 4. This line is common to find in B[e] object ([51]) but also in late B to late A type stars ([20]). Some authors (see Miroshnichenko [51]) use the He I 4471/Mg II 4481 ratio as an indicator of stellar spectra. Because B[e] objects have material around the central star, it is impossible without a model to separate their contributions on the line formation, so He I 4471/Mg II 4481 could be misleading.

The velocity line profile of the Mg II 4481.129Å from McDonald, CFHT and San Pedro Martir is shown in figure 4.61. This line is in pure absorption and seems to be almost stationary in velocity (see table 4.8). The mean radial velocity of this line is RV= (-15.1 ± 2.8) km s^{-1}. The EW$_\lambda$ is constant within the errors.

MJD	EW$_\lambda$ (mÅ)	RV (km s^{-1})
3895.60	353.0 $\pm$ 51.0	-15.4 $\pm$ 0.9
4284.60	352.3 $\pm$ 53.3	-10.0 $\pm$ 1.0
4671.60	316.7 $\pm$46.0	-11.2 $\pm$ 0.9
5080.63	301.2 $\pm$ 52.9	-11.7 $\pm$ 1.2
7172.76	324.3 $\pm$ 71.1	-14.7 $\pm$ 3.1
7173.75	324.7 $\pm$ 71.2	-14.6 $\pm$ 3.1
7174.74	313.3 $\pm$ 72.6	-16.8 $\pm$ 3.1
7175.73	307.3 $\pm$ 68.8	-12.7 $\pm$ 3.1
7176.76	307.2 $\pm$ 69.8	-19.5 $\pm$ 3.1
7177.73	325.6 $\pm$ 71.7	-15.4 $\pm$ 3.1

Table 4.8: EW$_\lambda$ and radial velocity of Mg II 4481.129Å line.
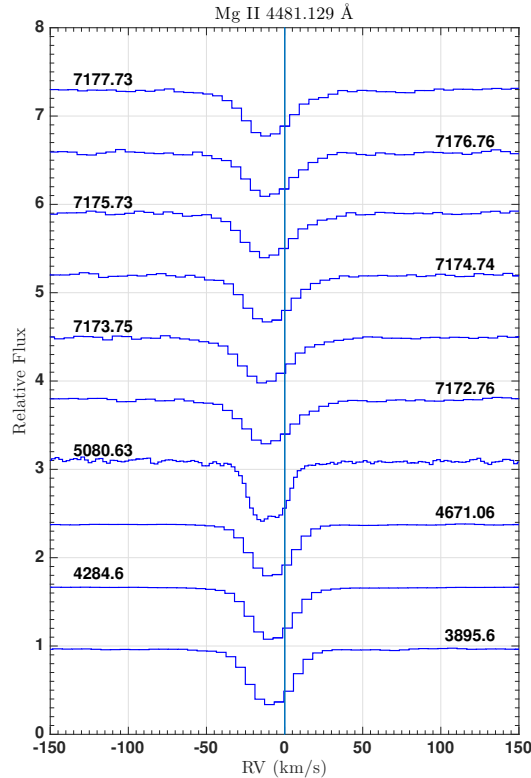
Figure 4.61: Mg II 4481.129Å: line profile variability. Spectra taken from the observatories of McDonald, CFHT and San Pedro Martir. The number on each spectrum is the MJD.

4.4.6   Na I Doublet $\lambda\lambda$ 5889.952, 5895.923Å

The Na I Doublet $\lambda\lambda$ 5889.952, 5895.923Å absorption lines come from the transition between the ground state $^2S_{1/2}$ and the level $^2P^o_{3/2}$ with energy $E_u = 2.104 eV$ and $^2P^o_{1/2}$ with energy $E_u = 2.102 eV$, respectively. The multiplet number is 1. Na I D is a component of the interstellar medium and so it is important to separate the interstellar component from the object. Otherwise we do not know if the line is stellar or not and how much it is. To do this, we must see the H I map survey ([31]) and find the interstellar component radial velocity in the direction of IRAS $17449 + 2320$. Figure 4.65 shows the profile of the interstellar neutral hydrogen. The Interstellar medium in the direction of IRAS $17449 + 2320$ has a radial velocity peaked around 2 km s^{-1}, instead the Na I D lines are peaked around -15 km s^{-1} (figure 4.62). This means that the Na I D lines are not interstellar.

The velocity line profiles from McDonald, CFHT and San Pedro Martir are shown on the left and right side of figure 4.62. This doublet has a strong core in absorption and wings in emission (see figure 4.66). I detect the emission wings only in the CFHT data because of the resolution. This emission is not a thermal effect, it is likely due to scattering of light in the envelope around the star.

Figure 4.63 shows the superposition of the Na I D lines for each day of observation. The two components of the doublet have the same profile. Figure 4.66 shows the superposition of Na I D2 and Fe II 5169.03Å for the second and third day of CFHT with the original resolution. The two Na I D2 lines have the same RV, exactly the same core profile but the line from the second day of CFHT has a higher emission in the red wing. A possible interstellar component is at 2 km s^{-1}.

Figure 4.64 show the difference between the sum of the doublet components of the third day at CFHT and the sum of the components of the first day at CFHT. This kind of plot shows if there are some changes in the line structure between these two days. The core is very stable, but there is a small variation in the emission peaks. This variation can be explained by a perturbation in the region where the line is emitting.
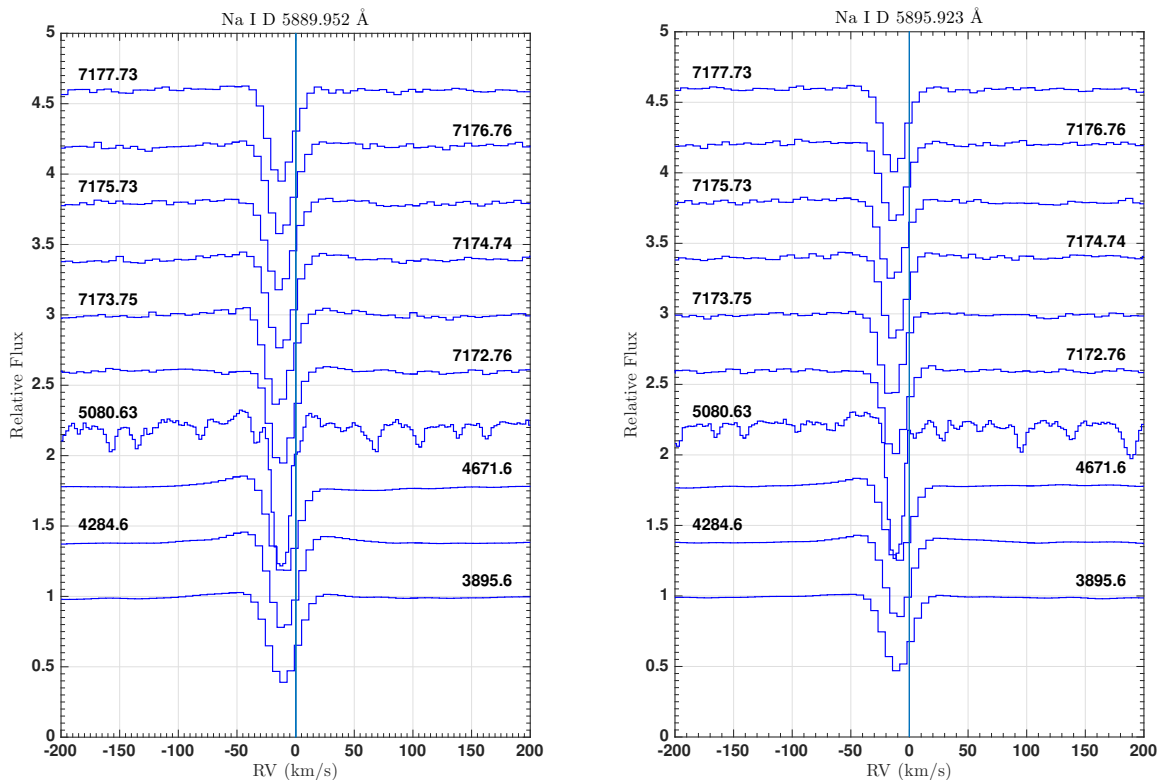
Figure 4.62: Na I D. Left: Velocity line profile of the Na I D 5889.952Å line. Right: Velocity line profile of the Na I D 5895.952Å line. Spectra taken from the observatories of McDonald, CFHT and San Pedro Martir. The number on each spectrum is the MJD.
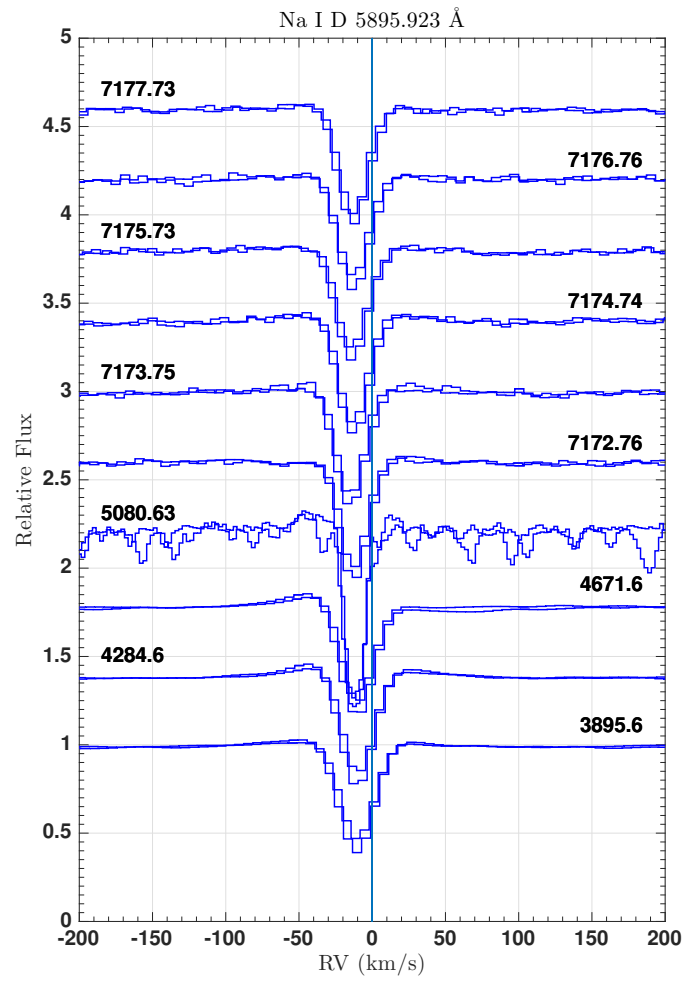
Figure 4.63: Superposition of the Na I D lines.
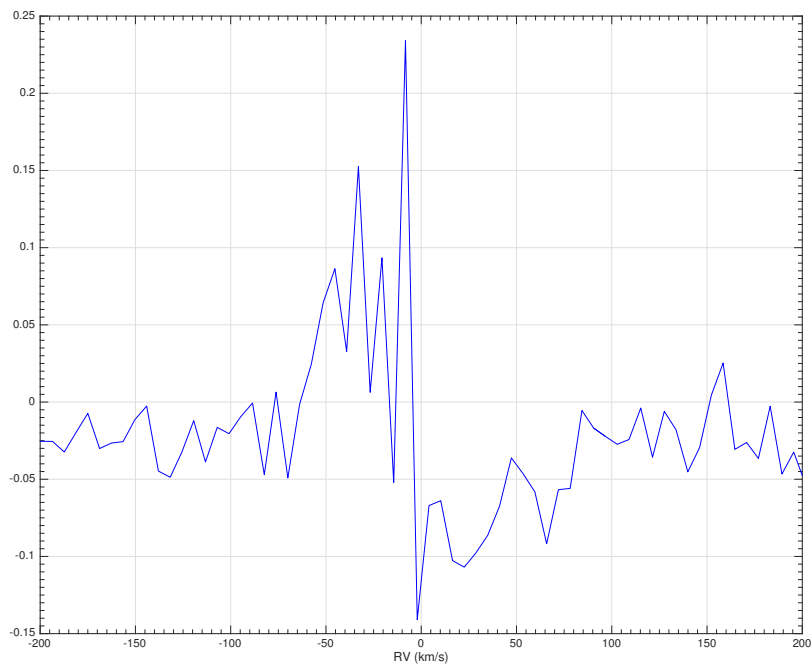
Figure 4.64: Difference between the sum of the doublet components of the third day at CFHT and the sum of the components of the first day at CFHT.
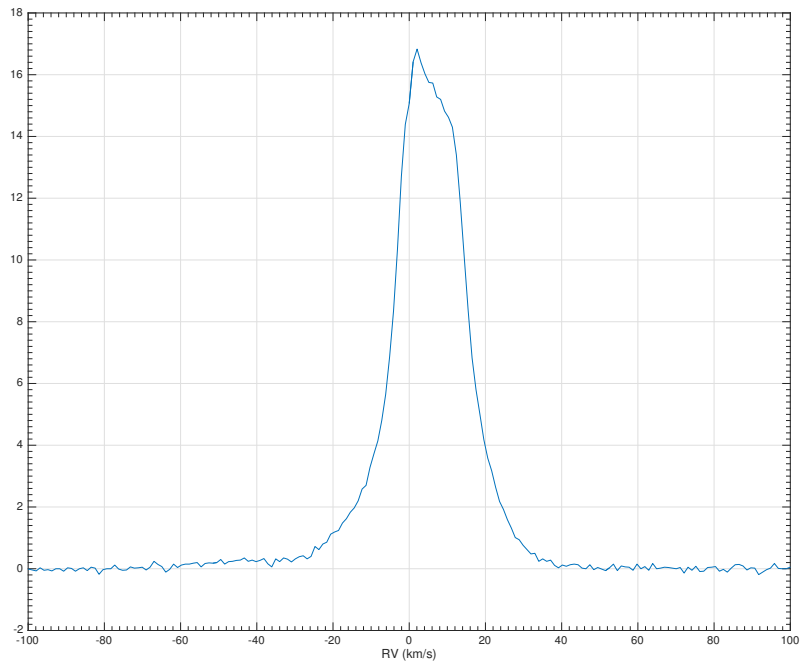
Figure 4.65: Radial velocity profile of the neutral hydrogen (21 cm) from the LAB survey ([31]) in the direction of IRAS $17449 + 2320$.

4.4.7 Fe II $\lambda\lambda$ 4923.921, 5018.434, 5169.03Å

The Fe II $\lambda\lambda$ 4923.921, 5018.434, 5169.03Å absorption lines come from the transitions between the same lower level $^6S_{5/2}$ with $E_l = 2.891eV$ and the upper level, respectively, $^6P_{3/2}^o$ with $E_u = 5.408eV$, $^6P_{5/2}^o$ with $E_u = 5.361eV$ and $^6P_{7/2}^o$ with $E_u = 5.289eV$. The multiplet is the 42. I choose to show the lines from this multiplet because of their interesting line profile. Their velocity line profiles are shown in figure 4.67 (respectively top left, top right and bottom). The data are from from McDonald, CFHT and San Pedro Martir. The line profile looks the same as Na I D, i.e. core in absorption and wings in emission (see figure 4.66) and the absorption core varies during time (figure 4.67) . An explanation of this profile can be the UV pumping from the 2343Å transition.

Figure 4.66 shows the superposition of Na I D2 and Fe II 5169.03Å for the second and third day of CFHT. The two Fe II lines have the same RV peaked at 17 ± 1 km s^{-1} but different residual flux and different emission component. The line from the second day of CFHT has a lower residual flux but higher emission in the red wing. The residual flux of Fe II are in antiphase with He I and I discuss this behaviour in paragraph 4.4.11.
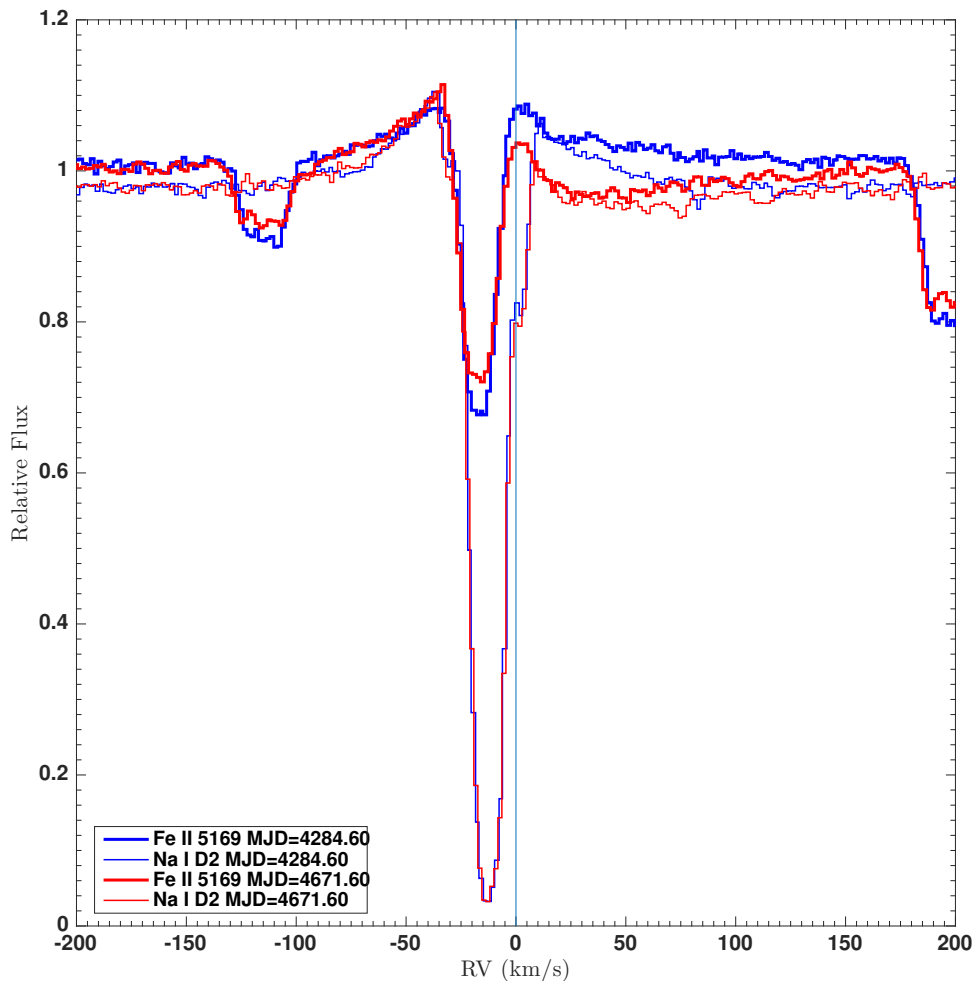
Figure 4.66: Superposition between the Fe II 5169.03Å and Na I D 5889.952Å for the second and third day of CFHT observations. The data are shown with the original resolution.
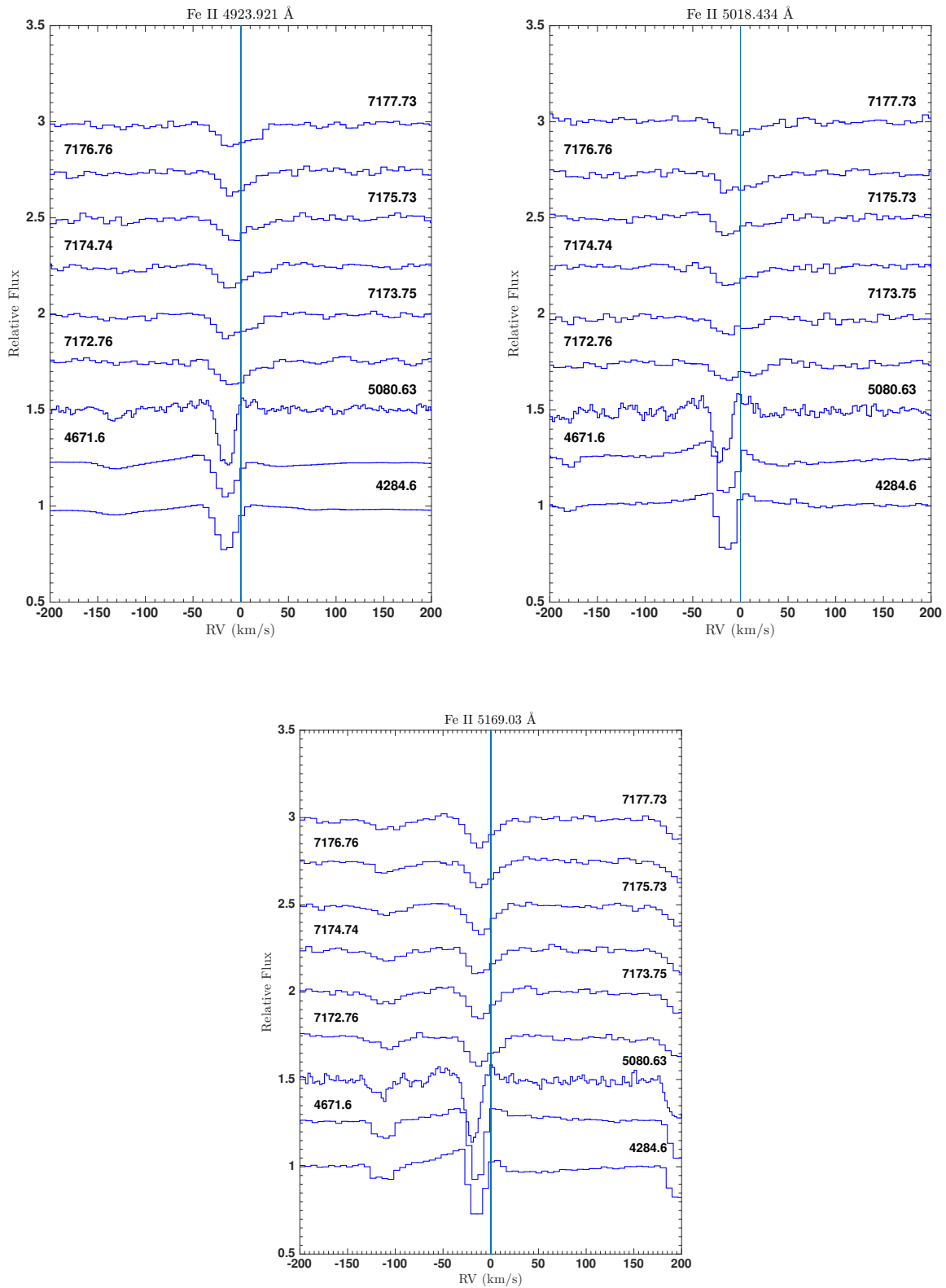
Figure 4.67: Fe II multiplet 42. Line profile variations of the Fe II $\lambda\lambda$ 4923.921, 5018.434, 5169.03Å lines respectively top left, top right and bottom. Spectra taken from the observatories of McDonald, CFHT and San Pedro Martir. The number on each spectrum is the MJD. In the top right plot, the Fe II absorption line at MJD= 5080.63 is shifted from the others because it is from the peripheral pixels of the McDonald CCD. In the bottom plot, the absorption features at ≈ -110 and ≈ 200 km s^{-1} are two Mg I lines.

Figures 4.68 shows the Grotrian diagram for Fe II lines. The Fe II lines studied here have the common upper level which could be pumped by a UV transition from the ground state.
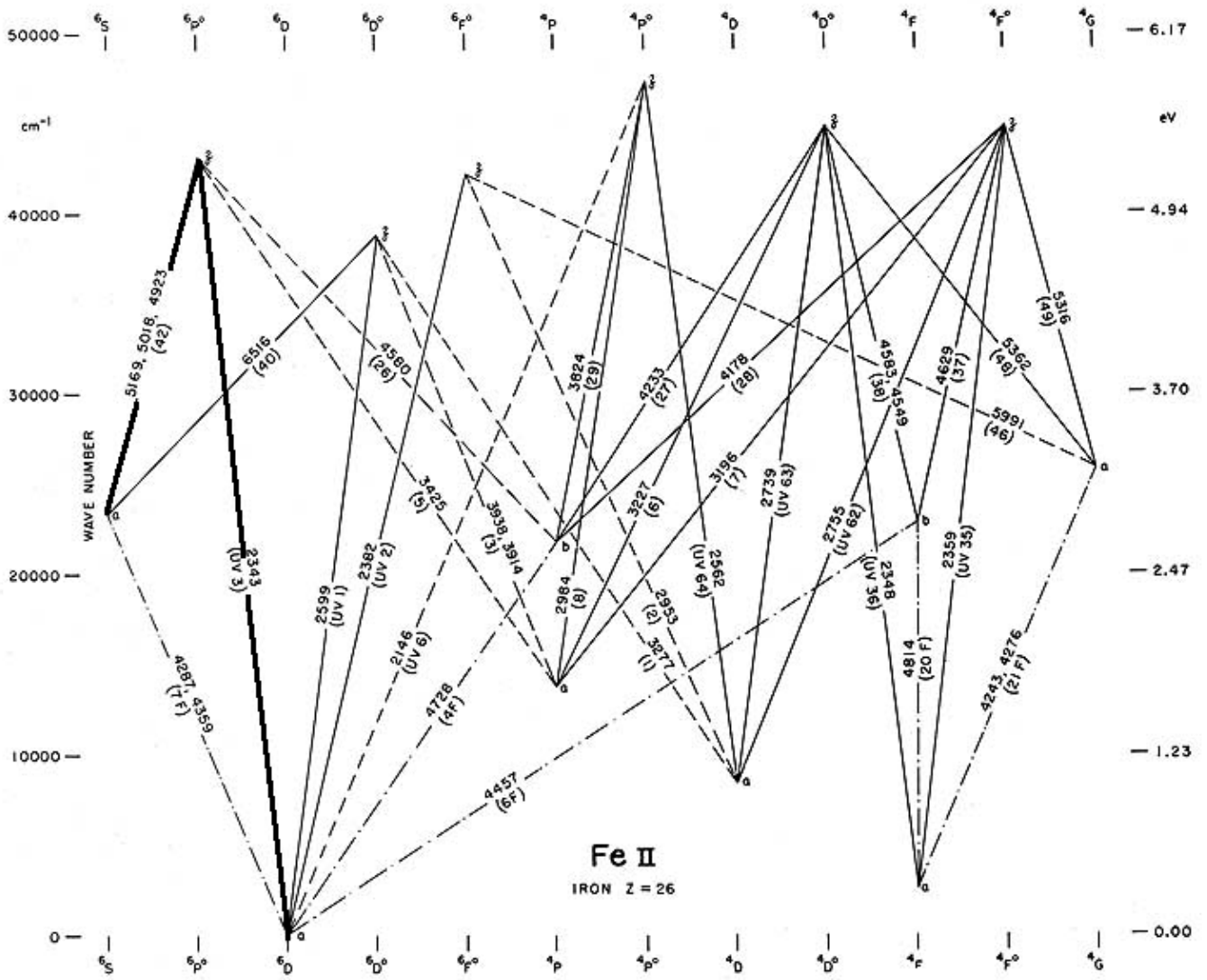
Figure 4.68: The Grotrian diagram for Fe II. For each transition the wavelength in Å is indicated. On the right and left columns the energy is indicated, repectively in cm^{-1} and in eV. On the bottom and upper lines, the electronic configuration in spectroscopic notation is shown. Diagram from [56].

4.4.8 Ca II

The Ca II $\lambda\lambda$ 3933.664, 3968.470Å absorption lines come from the transition between the same lower energy level, i.e. the ground level $^2S_{1/2}$, and the doublet $^2P^o$. The line at shorter wavelength has energy $E_u = 3.151eV$ and configuration $^2P^o_{3/2}$, instead the other line has energy $E_u = 3.123eV$ and configuration $^2P^o_{1/2}$. The multiplet is the number 1.

The velocity line profiles of Ca II 3933.664Å taken from CFHT and SPM are shown on the left side of figure 4.69. The right side of figure 4.69 shows the velocity line profile of the Ca II 3968.470Å taken from the two CFHT spectra. I show only these spectra because the SPM spectra are very noisy in the region of this line and McDonald does not cover this region. Ca II $\lambda\lambda$ 3933.664, 3968.470Å lines have a variable core in absorption but wings in emission like Na I D and Fe II from multiplet 42.
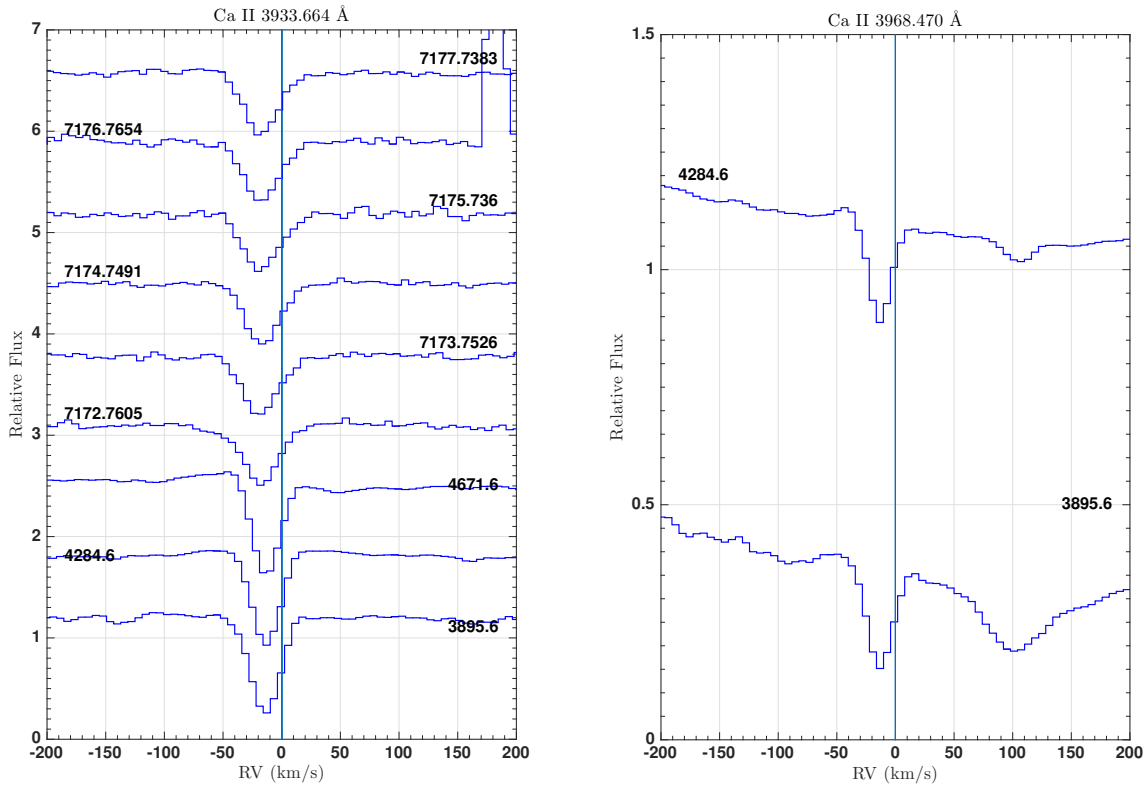
Figure 4.69: Ca II $\lambda\lambda$ 3933.664, 3968.470Å. Left: Velocity line profile of the Ca II 3933.664Å line. Right: Velocity line profile of the Ca II D 3968.470Å line. Spectra taken from the observatory of CFHT . The number on each spectrum is the MJD. In the right plot, the absorption feature at ≈ 100 km s^{-1} is Hϵ.

The Ca II $\lambda\lambda$ 8498.02, 8542.09, 8662.14Å absorption lines comes from from the transition between the $^2D_{3/2}$ level with energy $E_l = 1.692eV$ and the $^2P^o_{1/2}$ level with energy $E_u = 3.123eV$. The multiplet is the number 2. Figure 4.70 shows the velocity line profile of Ca II 8662.14Å (spectra are taken from CFHT observatory). The line has the core in absorption but the wings in emission like Ca II $\lambda\lambda$ 3933.664, 3968.470Å lines.
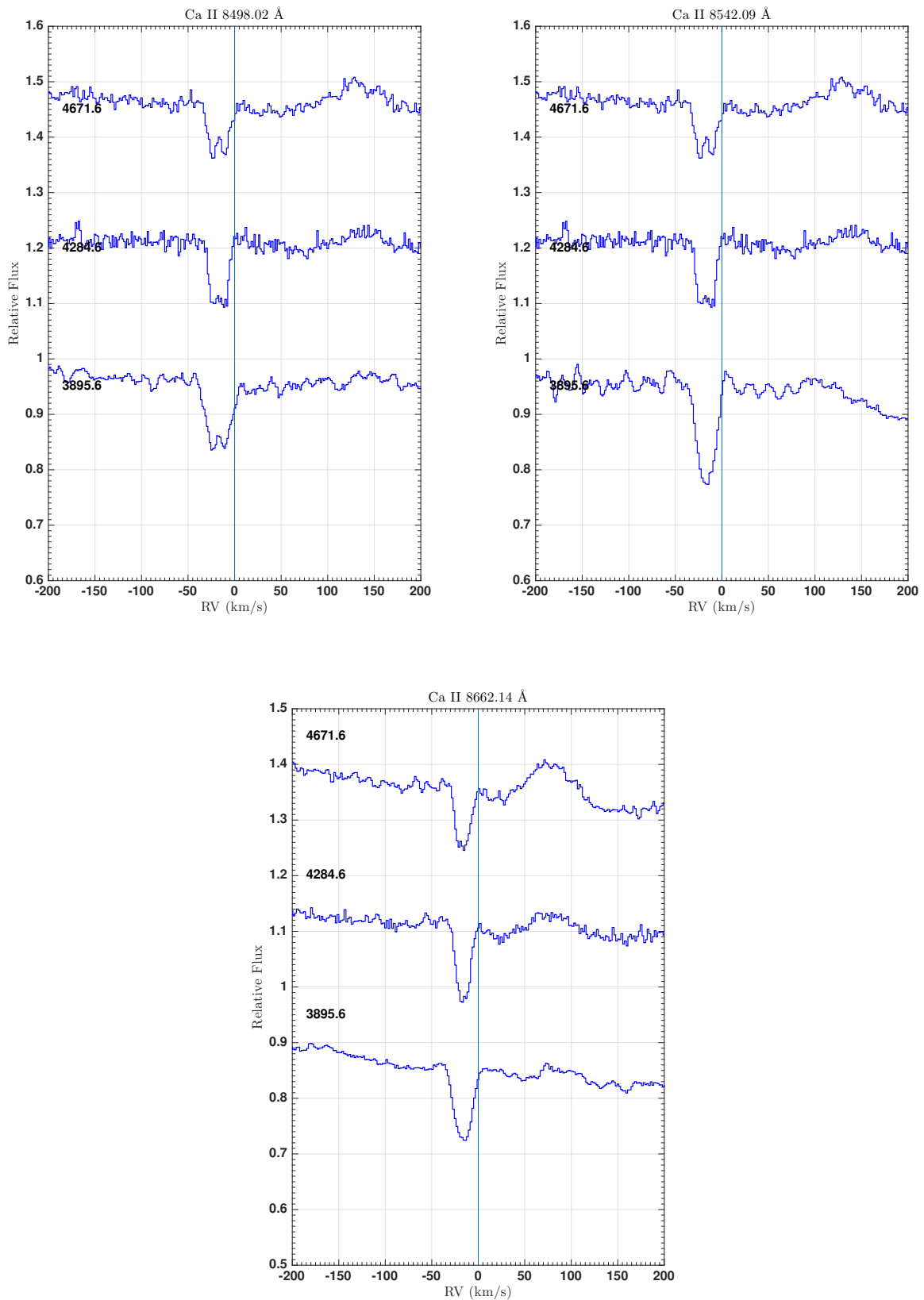
Figure 4.70: Ca II $\lambda\lambda$ 8498.02, 8542.09, 8662.14Å. Left: velocity line profile of Ca II 8498.02Å. Right: velocity line profile of Ca II 8542.09Å. Bottom: velocity line profile of Ca II 8662.14Å; the emission feature at ≈ 80 km s^{-1} is Pa13. Spectra taken from the observatory of CFHT. The number on each spectrum is the MJD.

Figures 4.71 shows the Grotrian diagram for Ca II lines. The Ca II lines studied here have the common upper level which could be pumped by UV radiation field.
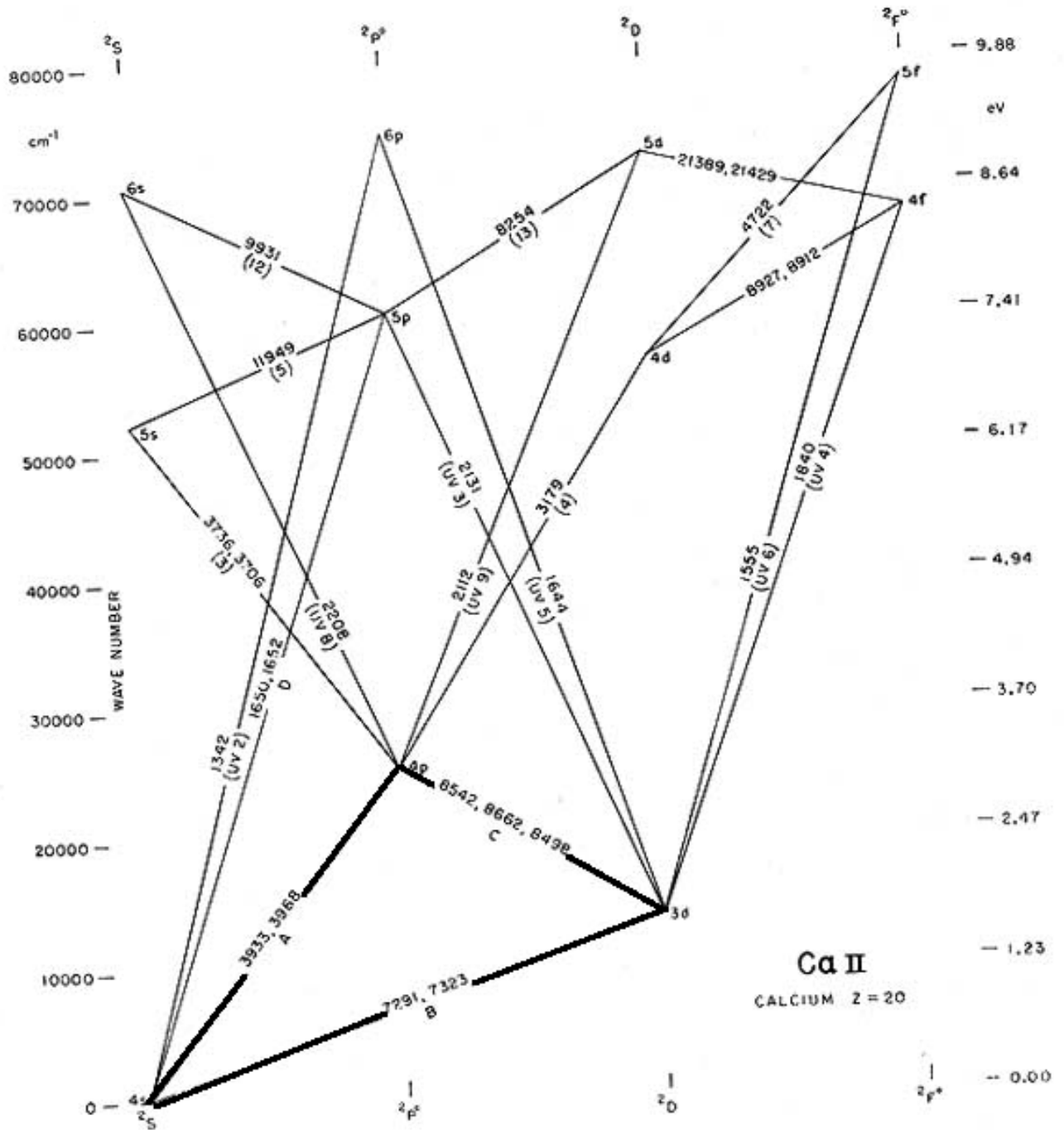
Figure 4.71: The Grotrian diagram for Ca II. For each transition the wavelength in Å is indicated. On the right and left columns the energy is indicated, repectively in cm^{-1} and in eV. On the bottom and upper lines, the electronic configuration in spectroscopic notation is shown. Diagram from [56].

4.4.9   Si II $\lambda\lambda$ 6347.091, 6371.359Å

The velocity line profiles for the Si II $\lambda\lambda$ 6347.091, 6371.359Å of the spectra taken from the observatories of Ondřejov, McDonald, CFHT and San Pedro Martir are shown in figure 4.72. These lines are in absorption and the line profile is asymmetric with a sharper decrease in the flux in the blue side than the red.

     Table 4.9 shows the equivalent width and the radial velocity for the Si II $\lambda\lambda$ 6347.091, 6371.359Å lines for CFHT and SPM observatories. RV as a function of the MJD is shown in figures 4.22 and 4.23 and discussed in paragraph 4.3.3.
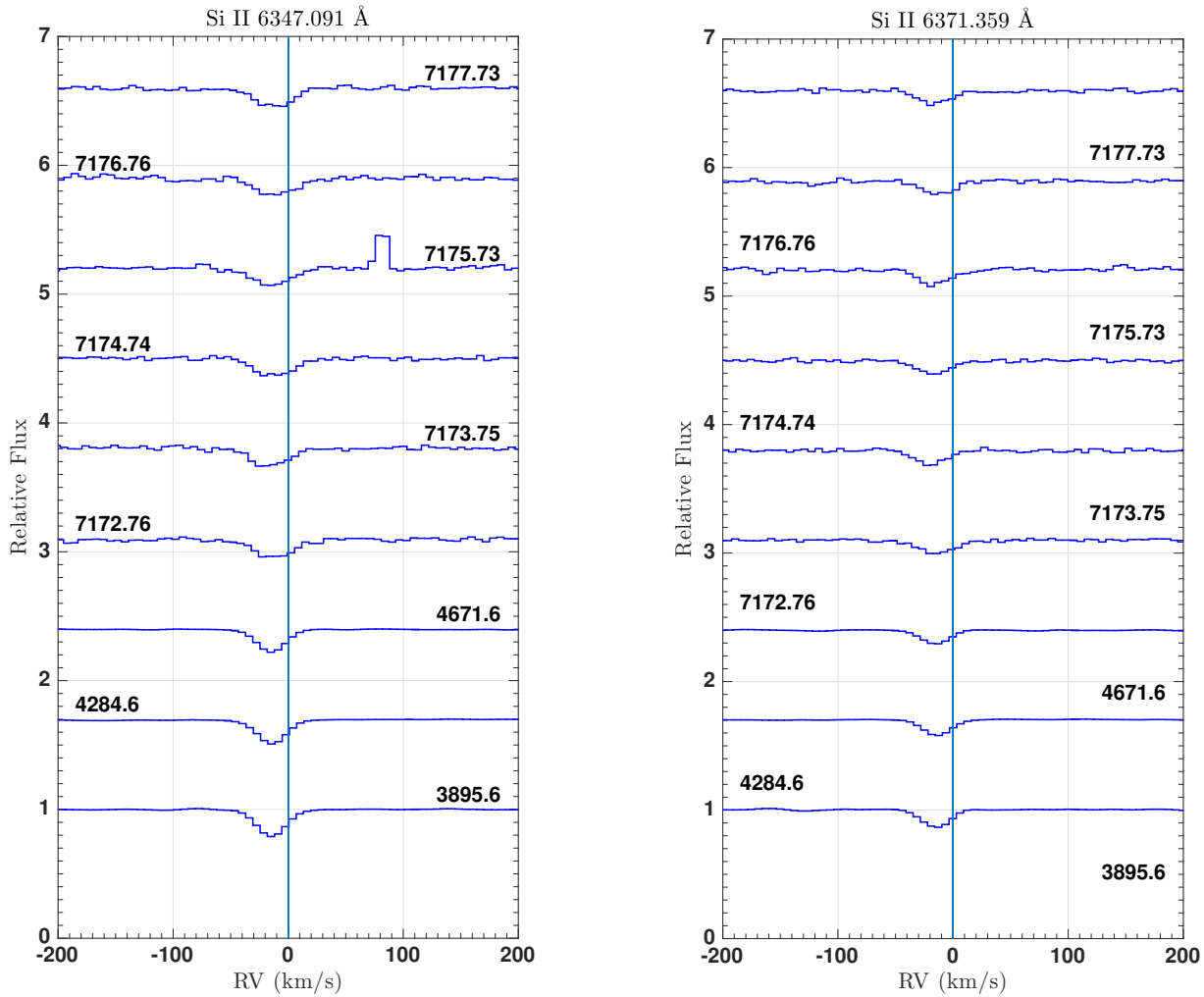
Figure 4.72: Si II $\lambda\lambda$ 6347.091, 6371.359Å. Left: velocity line profile variability of Si II 6347.091Å line. Right: velocity line profile variability of Si II 6371.359Å line. Spectra taken from the observatories of CFHT and San Pedro Martir. The number on each spectrum is the MJD.

MJD	EW$_{6347}$ (mÅ)	EW$_{6371}$ (mÅ)	RV$_{6347}$ (km s^{-1})	RV$_{6371}$ (km s^{-1})
3895.60	132.2 ± 25.0	86.8 ± 16.7	-19.5 ± 0.9	-19.1 ± 0.9
4284.60	132.7 ± 23.4	75.7 ± 14.9	-30.0 ± 0.9	-18.1 ± 0.9
4585.47	142 ± 41.6	86.6 ± 42.9	-14.9 ± 3.9	-10.5 ± 8.8
4603.44	102.4 ± 28.6	72.7 ± 37.1	-13.3 ± 3.3	-8.03 ± 6.7
4671.60	117.7 ± 20.7	69.9 ± 12.7	-20.3 ± 0.9	-17.8 ± 0.9
4940.44	117 ± 98.1	65.0 ± 61.6	-18.7 ± 8.6	-18.0 ± 6.2
5080.63	120.9 ± 25.7	86.0 ± 17.8	-19.7 ± 1.2	-21.7 ± 1.2
5616.64	117.6 ± 34.0	74.9 ± 29.5	-18.4 ± 2.5	-20.1 ± 4.4
5618.59	120.5 ± 35.1	50.6 ± 17.7	-18.7 ± 3.8	-19.0 ± 5.4
5642.61	104.4 ± 35.5	59.0 ± 20.3	-14.7 ± 3.9	-20.5 ± 3.3
5662.51	146.8 ± 29.2	69.9 ± 30.8	-14.7 ± 4.0	-14.5 ± 2.9
5671.55	138.3 ± 22.8	90.0 ± 26.8	-18.9 ± 1.7	-15.6 ± 4.2
5674.44	129.5 ± 29.4	112.4 ± 37.3	-16.2 ± 1.6	-13.8 ± 3.9
5688.59	120.4 ± 47.9	72.0 ± 42.6	-19.7 ± 3.3	-17.4 ± 5.6
5808.44	136.4 ± 19.5	95.1 ± 20.1	-14.9 ± 5.1	-16.4 ± 2.9
5839.36	144.6 ± 32.1	69.5 ± 27.7	-16.2 ± 3.7	-10.7 ± 4.0
5991.60	124.8 ± 67.7	129.4 ± 67.5	-23.0 ± 5.9	-23.2 ± 10.7
6011.61	117.4 ± 45.0	87.7 ± 38.8	-16.6 ± 3.3	-20.7 ± 7.1
6012.54	118.7 ± 35.9	76.3 ± 29.2	-18.4 ± 5.0	-22.5 ± 4.6
6132.39	135.8 ± 29.1	92.7 ± 21.9	-18.2 ± 3.5	-13.9 ± 2.7
6135.40	151.9 ± 41.2	86.4 ± 24.7	-19.8 ± 3.4	-16.7 ± 3.2
6154.35	117.2 ± 25.5	77.4 ± 22.1	-15.6 ± 1.8	-17.2 ± 2.3
6158.36	107.4 ± 21.7	80.7 ± 22.1	-18.6 ± 2.0	-16.0 ± 2.8
6187.34	126.5 ± 26.9	83.0 ± 37.1	-17.0 ± 2.2	-16.6 ± 4.6
6212.33	150.4 ± 46.7	93.7 ± 55.0	-15.3 ± 2.6	-17.1 ± 7.2
6400.49	141.0 ± 61.1	93.2 ± 55.7	-21.1 ± 3.4	-19.7 ± 4.7
6406.46	104.0 ± 40.4	58.8 ± 41.5	-13.1 ± 3.1	-14.8 ± 3.4
6421.40	123.7 ± 34.9	91.2 ± 40.7	-19.9 ± 7.8	-16.3 ± 3.6
6428.42	138.4 ± 29.9	88.5 ± 20.0	-20.1 ± 5.7	-17.0 ± 2.6
6457.45	142.0 ± 22.5	86.7 ± 23.2	-17.1 ± 2.1	-18.2 ± 3.9
6489.42	141.8 ± 25.6	86.6 ± 26.3	-18.6 ± 1.7	-17.7 ± 2.1
6521.41	103.0 ± 18.9	72.7 ± 19.3	-20.1 ± 1.6	-17.7 ± 2.9
6572.31	117.0 ± 25.5	63.7 ± 12.7	-15.7 ± 2.4	-15.1 ± 5.0
6592.24	117.6 ± 29.7	74.7 ± 25.9	-15.5 ± 1.9	-18.3 ± 2.7
6712.57	120.5 ± 28.5	50.6 ± 14.4	-17.7 ± 1.89	-14.3 ± 2.8
6718.63	104.4 ± 31.0	59.0 ± 17.7	-17.3 ± 2.3	-13.1 ± 4.2
6774.42	150.3 ± 38.3	69.9 ± 33.1	-17.4 ± 2.7	-16.9 ± 6.4
6809.51	138.3 ± 38.6	90.0 ± 45.3	-12.4 ± 3.7	-15.2 ± 5.0
6817.47	129.5 ± 30.2	109.4 ± 34.5	-16.3 ± 3.7	-15 ± 3.3
6854.40	120.4 ± 35.1	72.0 ± 31.2	-17.7 ± 1.8	-20.1 ± 3.2
6856.41	140.1 ± 22.3	95.1 ± 18.8	-19.3 ± 2.2	-12.6 ± 3.5
6861.44	144.6 ± 33.1	69.6 ± 28.5	-18.3 ± 2.2	-13.2 ± 2.5
6878.36	216.0 ± 26.9	46.7 ± 6.0	-16.6 ± 1.8	-17.1 ± 2.3
6900.36	124.8 ± 20.7	129.4 ± 20.6	-18.4 ± 5.0	-16.4 ± 2.1
6950.23	120.0 ± 31.8	87.7 ± 23.9	-18.3 ± 1.3	-17.1 ± 4.1
7172.76	138.4 ± 30.5	85.2 ± 20.6	-16.5 ± 3.1	-17.3 ± 3.1
7173.75	110.5 ± 27.4	81.1 ± 20.9	-22.5 ± 3.1	-19.6 ± 3.1
7174.74	116.6 ± 28.1	85.2 ± 20.9	-15.0 ± 3.1	-9.8 ± 3.1
7175.73	118.7 ± 27.1	80.2 ± 20.8	-21.1 ± 3.1	-12.9 ± 3.1
7176.76	121.0 ± 27.7	83.8 ± 20.9	-8.7 ± 3.1	-13.1 ± 3.1
7177.73	123.6 ± 29.7	74.3 ± 19.7	-20.0 ± 3.1	-23.0 ± 3.1

Table 4.9: EW$_\lambda$ and radial velocity of Si II $\lambda\lambda$ 6347.091, 6371.359Å lines

4.4.10   Superposition of emission lines

Some species have composite profiles with both emission and absorption. Figure 4.73 shows the superposition of Hβ(minus β Leo), Fe II 5169.03Å, Na I D2, O I 7774.18Å and O I 8446.36Å taken from CFHT MJD= 4671.60. The emission is extend in the range of velocity $[-300, 300]$ km s^{-1} meaning that all of these transitions are forming in the same environment. In the case of Fe II and Na I D, the wings are contaminated by the presence of other absorption lines and so their extension in velocity seems to be shorter.
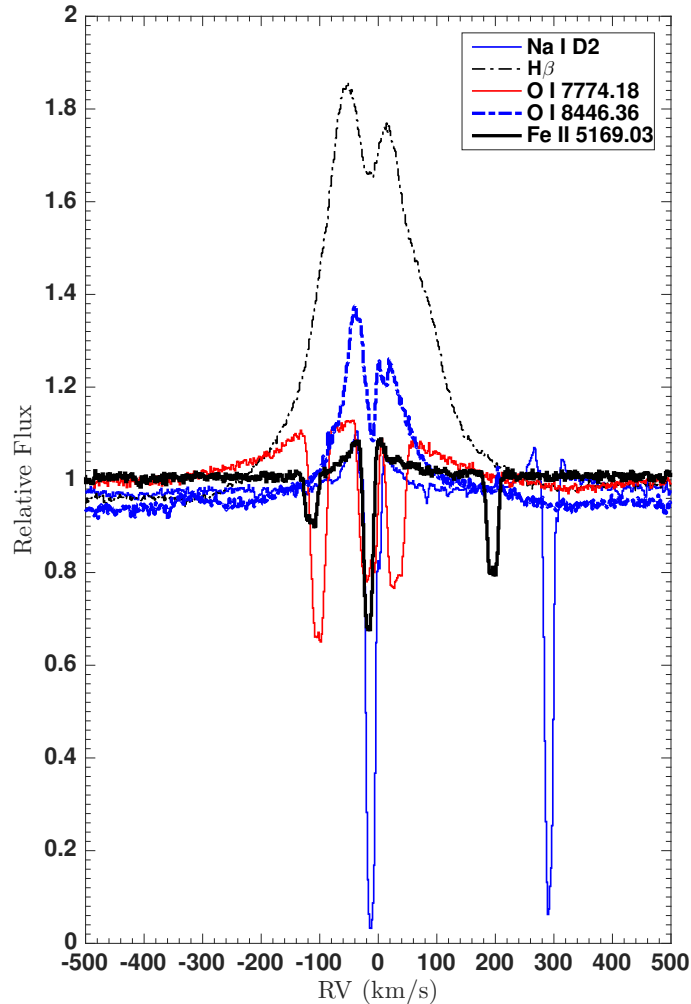
Figure 4.73: Superposition of Hβ(minus β Leo), Fe II 5169.03Å, Na I D2, O I 7774.18Å and O I 8446.36Å. Spectra from CFHT MJD= 4671.60.

4.4.11   Antiphase variability of He I and Fe II RMT 42

Looking at the CFHT spectra at the original resolution, I found trace of a variation in the residual flux in He I and Fe II. Between the first and the second day of CFHT (MJD= 3895.6 and MJD= 4284.6) there is no evident change. There is a variation in the residual between the second (or the first) and the third (MJD= 4671.6). There is an antiphase in the line profile variation between the two species, i.e. when He I has stronger absorption (third day), the Fe II has weaker absorption (third day) and viceversa (first and second days). Figure 4.74 shows the antiphase between Fe II 5169.03Å and He I 5875.621Å. In paragraph 4.6 I will discuss this behaviour.
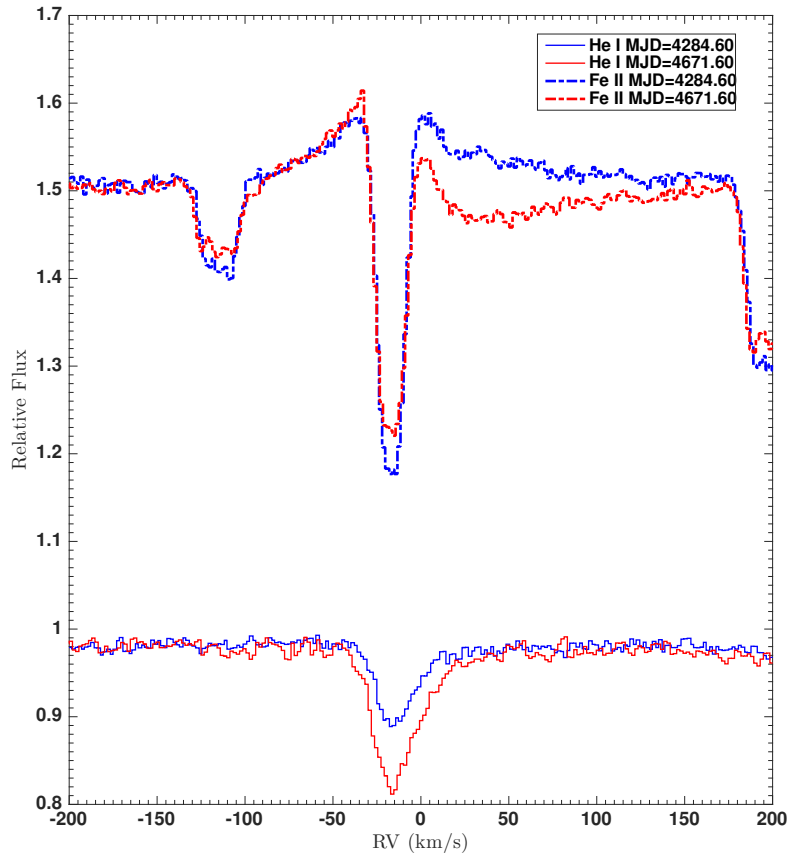
Figure 4.74: He I - Fe II antiphase. Spectra from CFHT MJD= 4284.60 and MJD= 4671.60.

4.5 UV map from GALEX

The Galaxy Explorer survey (GALEX) was a space mission with the aim of investigating how star formation in galaxies evolved from the early Universe up to the present and it provides NUV field maps. Figure 4.75 shows the NUV map in the neighborhood of IRAS $17449 + 2320$. The symbol V is placed on IRAS $17449 + 2320$ that is not detected by GALEX. This confirms the idea of Miroshnichenko ([51]) that FS CMa objects are located outside star forming regions.

4.6 Summary

After the summary on the Balmer lines (paragraph 4.4.1.10), I am going to report a summary on the other studied lines and the implications of the observed properties on the physical conditions of IRAS $17449 + 2320$.

The object of this thesis shows the B[e] phenomenon. In the spectroscopic analysis I found the presence of forbidden emission lines ([O I]), permitted emission lines (Fe II from multiplet 42, Na I D and Ca II from multiplet 1), absorption lines (Fe II, Ca II, Ti II, Mg II, Na I D, He I etc.) but also Balmer lines in emission (Hα in particular). These results are in accord with at least some observational criteria for the B[e] phenomenon. In particular I found evidence of circumstellar material composed of an optically thin region (presence of emission lines) and an optically thick region (presence of non photospheric absorption lines).

Some B[e] objects are binaries. They are composed by two stars, one in the spectral range O9 - A2 and a colder and fainter, or degenerate companion (white dwarf). A companion signal by a composite spectrum with spectral lines typical of another star with different spectral type or double peak profiles in the lines that are symptom of two radial velocity components. None of these observables were found in the spectra (see paragraph 6.6 for the discussion).

In paragraph 4.4.4, I said that O I emission lines could be pumped by radiative decay of the $^3D^o$ level, which is created by the absorption of photons in the UV with wavelength $\lambda = 1025.762$Å. At almost the same
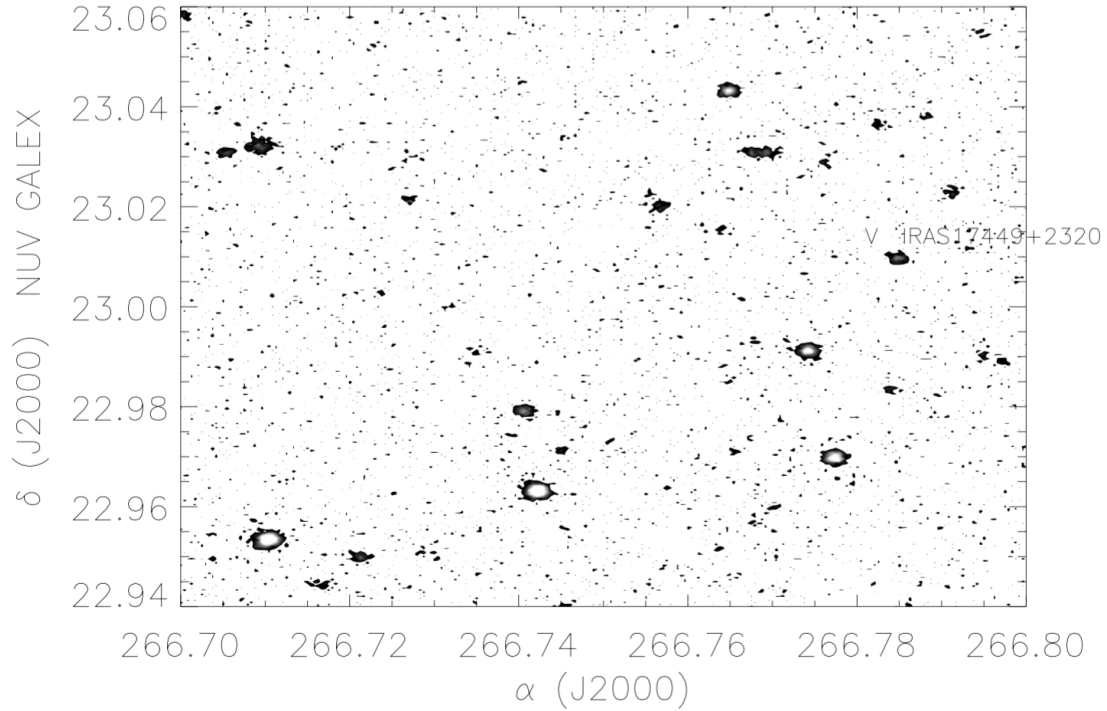
Figure 4.75: UV map in the neighborhood of IRAS 17449+2320. The symbol *V* is placed on IRAS 17449+2320.

wavelength, there is the Lyβ ($\lambda = 1025.728$Å). Hence the fact that photons are available in this spectral region, could also explain the Hα emission. Lyβ in absorption means that electrons are excited from the ground state ($n = 1$) to the $n = 3$ state then the decay to $n = 2$ to form Hα emission. The UV radiation field could also pump Ca II and Fe II from different transitions (see figures 4.68 and 4.71) but, unfortunately, I cannot investigate in this interesting spectral region for lack of available UV spectra.

The presence of He I, even if weak, can be used as an indicator of the stellar spectral type. Its strength indicates that IRAS $17449 + 2320$ is a late B-type main sequence star, in particular a B9V. Also the presence of Paschen lines confirm the hypothesis of a MS star.

In paragraph 4.4.11, I found trace of antiphase between the residual of He I and Fe II. The phenomenon behind this variation is not clear, a redistribution in the UV flux could explain this, but unfortunately, UV spectra are not available. The antiphase also suggests that the helium is partially photospheric and without models it is not possible to separate the circumstellar from the photospheric contribution. This does, however, rule out an A0 V classification since the He I wouldn't be excited or appear in the spectrum at its detected EW.

Chapter 5

Spectroscopy in a nutshell

Spectroscopy is the study of the interaction between matter and radiation field. Studying the intensity of the incoming light from an object at different wavelength, it is possible to get information about the source and the physical processes like rotation, wind, eruptions and jets, the chemical composition and its abundance, physical properties like temperatures, densities, the presence of magnetic fields, the presence of a companion, a disk and so on. In this chapter, I introduce spectroscopic notation, the electric transitions in atoms, the selection rules for the creation of a line, the mechanisms that can form a line profile and the principles of line radiative transfer.

5.1 Spectroscopic notation of the energy levels of atoms

Electrons are fermions and hence they must obey at the Pauli exclusion principle that forbids two electrons from sharing the same wave function. The wave function is characterized by four quantum numbers: the principal quantum number n, that is integer and defines the number of the radial nodes of the wave function ($n \geq 1$); the quantum number l that is the orbital angular momentum in units of $\hbar$ and $0 \leq l < n$; the m_z quantum number that represents the projection of the angular momentum onto the z axis and it can take $2l + 1$ values from $-l$ to l, and the projection of the spin onto the z axis, m_s, that can take only two values because of the nature of the electrons ($m_s = \pm 1/2$ in units of $\hbar$). If an orbital has more than one and less than $4l + 1$ electrons, then there is more than one way in which the orbital and the spin angular momentum vectors can add. In the so called $L - S$ coupling approximation, the individual spin angular momenta add vectorially to give a total spin $\mathbf{S}$, and orbital angular momentum combine separately to give the total orbital angular momentum $\mathbf{L}$. The vectorial sum of $\mathbf{S}$ and $\mathbf{L}$ gives the total angular momentum $\mathbf{J} = \mathbf{S} + \mathbf{L}$. Because of the possibility of multiple values of the total angular momentum, the terms are referred as multiplets (singlet, doublet, triplet and so on).

The multiplicity of a term with total spin S and totat orbital angular momentum L is $g_m = (2S+1)(2L+1)$. When the spin-orbit coupling is taken into account, these states are split into distinct fine-structure levels, each with a definite value of J and a degeneracy $g = 2J + 1$.

The parity p of an energy level is

$$p = \begin{cases} \text{even if} & \prod_i (-1)^{l_i} = 1 \\ \text{odd if} & \prod_i (-1)^{l_i} = -1 \end{cases} \tag{5.1}$$

and is even or odd depending on whether the electronic wave function changes sign under reflection of all of the electron positions.

In the followinf I will consistently use spectroscopic notation assuming $L - S$ coupling

$$^{2S+1}\mathcal{L}_J^p \tag{5.2}$$

If the parity is odd p is replaced with o, otherwise it is left blank.

5.2 Transitions

Call X_l an absorber in the lower energy level, if there are photons having energy equal to $h\nu = E_u - E_l$, where E_u is the energy of the upper level and E_l the energy of the lower level, then the absorber can absorb a photon and undergo an upward transition

$$\text{absorption} \quad X_l + h\nu \to X_u \tag{5.3}$$

Be n_l the number density of X_l, then the rate per volume at which the absorbers absorb photons is proportional to n_l and to the energy density of the photons

$$R_{lu}^{stim} = n_l B_{lu} u_\nu \tag{5.4}$$

where u_ν is the radiation energy density per unit frequency and the B_{lu} is the Einstein absorption coefficient for the transition $l \to u$.

Now, the absorber (the electron) X is in the excited energy level u and it can decay to a lower energy level l with emission of a photon. It can happen in two different ways: with a spontaneous emission or with a stimulated emission.

In the case of the spontaneous emission

$$\textbf{spontaneous emission} \quad X_u \to X_l + h\nu \tag{5.5}$$

where the electron in the upper level, after a certain time, emits a photon of energy equals to the difference $E_u - E_l$ and the electron decays into the lower energy level.

The spontaneous emission is a random process, and it is independent from the radiation field. The probability per unit time A_{ul} that the electron decays from the upper to the lower energy level is called Einstein spontaneous emission coefficient.

In the case of stimulated emission

$$\textbf{stimulated emission} \quad X_u + h\nu \to X_l + 2h\nu \tag{5.6}$$

where the electron in the upper level interacts with a photon of energy equals to the difference $E_u - E_l$ and decays into lower energy level emitting two identical photons, also identical respect to the one that interacts with the electron. The stimulated emission process depends on the radiation field, on the electronic density in the upper level and on a coefficient called Einstein stimulated emission coefficient B_{ul}. Hence the total rate of population of the upper level is

$$R_{ul}^{stim} + R_{ul}^{spon} = n_u \left(A_{ul} + B_{ul} u_\nu \right) \tag{5.7}$$

If there is thermal equilibrium, the radiation field source is a black body and hence the radiation source function is the Planck function

$$\mathscr{B}_\nu(T) = \frac{2h\nu^3}{c^2(e^{h\nu/kT} - 1)} \tag{5.8}$$

The relation between the Planck function and the photon energy density is

$$u_\nu^{LTE} = \frac{4\pi}{c} \mathscr{B}_\nu(T) = \frac{8\pi h\nu^3}{c^3(e^{h\nu/kT} - 1)} \tag{5.9}$$

Using equation 5.9, the net rate of density population of level l is

$$\frac{dn_l}{dt} = -R_{lu}^{stim} + \left(R_{ul}^{stim} + R_{ul}^{spon} \right) =$$
$$= -\frac{8\pi h\nu^3 n_l B_{lu}}{c^3(e^{h\nu/kT} - 1)} + n_u \left(A_{ul} + \frac{8\pi h\nu^3 B_{ul}}{c^3(e^{h\nu/kT} - 1)} \right) \tag{5.10}$$

If the absorbers are in equilibrium with the radiation, then the upper and the lower energy levels are populated following the relation

$$\frac{n_u}{n_l} = \frac{g_u}{g_l} e^{-(E_u - E_l)/kT} \tag{5.11}$$

the detailed balance

$$\frac{dn_l}{dt} = 0 \tag{5.12}$$

Using equations 5.10, 5.11 and 5.12 we can write the emitted intensity at frequency ν

$$I_\nu = \frac{A_{ul}}{B_{ul} \left[(n_l B_{lu}/n_u B_{ul}) - 1 \right]} =$$
$$= \frac{A_{ul}}{B_{ul}} \left(e^{\Delta E_{lu}/kT} \frac{g_l B_{lu}}{g_u B_{ul}} - 1 \right)^{-1} \tag{5.13}$$

the enenrgy distribution is a Planck function and hence the relations between the Einsten coefficients are

$$B_{ul} = \frac{c^3}{8\pi h \nu^3} A_{ul} \tag{5.14}$$

$$B_{lu} = \frac{g_u}{g_l} B_{ul} = \frac{g_u}{g_l} \frac{c^3}{8\pi h \nu^3} A_{ul} \tag{5.15}$$

5.2.1 Absorption cross section and profile function

Let $\sigma_{lu}(\nu)$ be the cross section for absorborption of a photon of frequency ν in the $l \to u$ transition. The absorption rate is now

$$\left(\frac{dn_u}{dt}\right)_{l \to u} = n_l \int \sigma_{lu}(\nu) c \frac{u_\nu}{h\nu} d\nu \approx n_l c \frac{u_\nu}{h\nu} \int \sigma_{lu}(\nu) d\nu \tag{5.16}$$

where it is possible to assume that u_ν/ν does not vary appreciably over the line profile. Thus

$$B_{lu} = \frac{c}{h\nu} \int \sigma_{lu}(\nu) d\nu \tag{5.17}$$

Using equation 5.15 the integral of the absorption cross section is

$$\int \sigma_{lu}(\nu) d\nu = \frac{g_u}{g_l} \frac{c^2}{8\pi \nu_{lu}^2} A_{ul} \tag{5.18}$$

It is possible to write the monochromatic absorption cross section as a function of the spontaneous emission coefficient, and of a normalized function, called the normalized line profile function ϕ_ν

$$\sigma_{lu}(\nu) = \frac{g_u}{g_l} \frac{c^2}{8\pi \nu^2} A_{ul} \phi_\nu \tag{5.19}$$

where ϕ_ν is the normalized profile function,

$$\int_{-\infty}^{+\infty} \phi_\nu d\nu = 1 \tag{5.20}$$

The intrinsic profile function is a Lorentzian

$$\phi_\nu^{intr} = \frac{4\gamma_{ul}}{16\pi^2(\nu - \nu_{ul})^2 + \gamma_{ul}^2} \tag{5.21}$$

where

$$\gamma_{ul} = 2\pi \Delta \nu_{FWHM}^{intr} \tag{5.22}$$

with $\Delta \nu_{FWHM}^{intr}$ as the full width at half maximum of the line profile. The intrinsic width of the absorption line reflects the widths of the energy of levels u and l due to the finite lifetimes of these levels against transitions to all other levels, both radiative and collisional. If spontaneous decay dominates the lifetime,

$$\gamma_{ul} \equiv \gamma_{lu} = \sum_{E_j < E_u} A_{uj} + \sum_{E_j < E_l} A_{lj} \tag{5.23}$$

Since the atoms are in motion and assuming thermal motion, their velocity distribution is a Maxwellian (only Gaussian for radial velocity) function. Hence the line profile function is distorted by the motion and the real profile function is the convolution of the intrinsic line profile (Lorentzian $\mathscr{L}$) with a Gaussian function $\mathscr{G}$ to form the *Voigt line profile*

$$\phi_\nu^{Voigt} \equiv \mathscr{L} \star \mathscr{G} = \frac{1}{\sqrt{2\pi}} \int \frac{dv}{\sigma} e^{-v^2/2\sigma^2} \frac{4\gamma_{ul}}{16\pi^2 \nu^2 + \gamma_{ul}^2} \tag{5.24}$$

Generally, the thermal velocity dispersion is greater than the intrinsic line width $\sigma_v \gg \Delta v_{FWHM}^{intr}$, and the core of the line profile is well-approximated by treating the intrinsic line profile as a δ-function. Hence the core of the line has a Maxwellian profile

$$\phi_\nu \approx \frac{c}{\sqrt{2\pi}\nu_{ul}\sigma_v} e^{-v^2/2\sigma_v^2} \tag{5.25}$$

5.2.2 Life time of a level and oscillator strength

The spontaneous emission coefficient A_{ul} is the inverse of the life time of the upper level

$$A_{ul} = \tau_{ul}^{-1} \tag{5.26}$$

and the greater the spontaneous emission coefficient, the greater the strength of the radiative transition. The oscillator strength f_{ul} is defined as

$$f_{lu} \equiv \frac{m_e c}{\pi e^2} \int \sigma_{lu}(\nu) d\nu \tag{5.27}$$

Using equations 5.18 and 5.19, is related to the spontaneous emission coefficient by

$$A_{ul} = \frac{8\pi e^2 \nu^2}{m_e c^3} \frac{g_l}{g_u} f_{lu} = \frac{0.6670 \ \text{cm}^2\text{s}^{-1}}{\lambda^2} \frac{g_l}{g_u} f_{lu} \tag{5.28}$$

The absorption cross section is then given by

$$\sigma_{lu}(\nu) = \frac{\pi e^2}{m_e c} f_{lu} \phi_\nu \tag{5.29}$$

The oscillator strength has the property that the one for the downward transition is negative, instead the one for the upward transition is positive and it is true that

$$g_l f_{lu} = -g_u f_{ul} \tag{5.30}$$

5.2.3 Selection rules for radiative transitions

Not all the radiative transitions are permitted, this depends on the selection rules. The strongest transitions are electric dipole transitions and are the allowed ones. They satisfy the selection rules for $L - S$ coupling:

1. Parity must change

2. $\Delta L = 0, \pm 1$

3. $\Delta J = 0, \pm 1$, but the $J_l = 0 \leftrightarrow J_u = 0$ is forbidden

4. Only one single electron nl changes, with $\Delta l = \pm 1$

5. $\Delta S = 0$, so spin does not change

A permitted transition is not denoted with square brackets, an example is

$$\text{Si II} \ \ 6347.11 \ \text{\AA} \ \ {}^2 S_{1/2} \ \ - \ \ {}^2 P^o_{3/2}$$
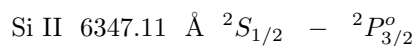
This transition has $A_{ul} = 5.84 \cdot 10^7 \ s^{-1}$ hence a the lifetime is $\tau_{ul} \approx 0.17 \ ns$.

Than, there are the spin-forbidden transitions, also called semiforbidden transitions. These kind of transitions follow the rules from 1 to 4 but the spin changes, so $\Delta S \neq 0$. A semiforbidden transition is denoted with a single right square bracket as follow

$$\text{O I]} \ \ 1641.305 \ \text{\AA} \ \ {}^1 D_2 \ \ - \ \ {}^3 S^o_1$$

This transition has $A_{ul} = 1.83 \cdot 10^3 \ s^{-1}$ hence a the lifetime is $\tau_{ul} \approx 0.55 \ ms$.

The third is forbidden, and is an electric quadrupole or magnetic dipole transitions. A forbidden transition is denoted with two square brackets,

$$\text{[O I]} \ \ 6300.304 \ \text{\AA} \ \ {}^3 P_2 \ \ - \ \ {}^1 D_2$$

This is a magnetic dipole transition with $A_{ul} = 5.63 \cdot 10^{-3} \ s^{-1}$.

There is a hierarchy in the transition probability: semiforbidden transitions are $\sim 10^{-6}$ than the permitted, and the forbidden are $\sim 10^{-2} - 10^{-6}$ than the semiforbidden. Forbidden transitions are very important in astrophysics because of their long lifetime. At high density, such excited states are depopulated by collisions, but at very low densities, collisions are infrequent enough that radiative transitions occur.

5.2.4 Collisional processes

Collisional processes are important for two reason:

a) Collisions excite atoms that then can decay radiatively. These processes lead to a cooling process of the medium.

b) Collisions puts species into excited states that may serve as diagnostics of the physical conditions such as the density, the temperature and the radiation field in the medium.

5.2.5 Nomenclature for line formation

5.2.5.1 Resonance line scattering

In this case, the emitted photon has almost the same energy of the absorbed photon, apart from the Doppler shift due to the thermal motion of the atom. This process is called *resonance line scattering* because the photon was only scattered in another direction. If the line transition is from the ground state, the line is called 'resonance line' and the process 'resonance scattering'. The process is coherent, hence the emission will be polarized. Scattering process can give rise to emission lines from stellar winds.

5.2.5.2 Line emission by recombination

Usually, recombination of an ambient electron with an ion proceeds directly to the ground state of the atom, but the ion can also recombine to an excited state. The resulting excited atom leads to a cascade by line emission from photo-de-excitation.

5.2.5.3 Line emission from photo or collisional excitation

A way to convert kinetic energy into photon energy is by collisional excitation and the subsequent photo-de-excitation. This process is efficient when the collisions are frequent and energetic as in a hot plasma. This is responsible for the emission lines from hot cromospheres and coronae.

5.2.5.4 Pure absorption

Photo-excitation of an excited atom into a higher excited state can be followed by collisional de-excitation to another lower level. This results in the destruction of the photons of the first transition and the creation of photons in the second transition.

5.3 Radiative Transfer

The radiative transfer theory describes the propagation of radiation through absorbing and emitting media. Let $I_\nu(\nu)$ be the specific intensity, hence the electromagnetic power per unit area, with frequencies in the range $[\nu, \nu + d\nu]$ propagating in the direction $\hat{\mathbf{n}}$ in the solid angle $d\Omega$ in the point $(\mathbf{r}, t)$ is

$$I_\nu(\nu, \hat{\mathbf{n}}, \mathbf{r}, t)d\nu d\Omega \tag{5.31}$$

In the special case of locat thermodynamic equilibrium LTE, the intensity is equal to that of a blackbody so recalling equation 5.8

$$(I_\nu)_{LTE} = \mathscr{B}_\nu \equiv \frac{2h\nu^3}{c^2(e^{h\nu/kT} - 1)} \tag{5.32}$$

If a beam enters a slab of material, the specific intensity exiting from the slab is different from the entering intensity. Considering only absorptions and emissions, the radiative transfer equation is

$$dI_\nu = -I_\nu \kappa_\nu ds + j_\nu ds \tag{5.33}$$

where ds is the path of the propagation, κ_ν is the attenuation coefficient (dimensions 1/length) and j_ν is the emissivity at frequency ν (dimensions power per unit of volume per unit of frequency per unit of solid angle). The term $-I_\nu \kappa_\nu ds$ is the net change of the specific intensity due to absorption and stimulated emission, and $j_\nu ds$ is the net change due to spontaneous emission.

The emissivity j_ν depends on the frequency, on the Einstein spontaneous coefficient, on the population of the upper level and on the profile function as follow:

$$j_\nu = \frac{1}{4\pi} n_u A_{ul} h\nu \phi_\nu \tag{5.34}$$

Instead the attenuation coefficient κ_ν is proportional to the net absorptions hence absorption minus the stimulated emission:

$$\kappa_\nu = n_l \sigma_{lu}(\nu) - n_u \sigma_{ul}(\nu) \tag{5.35}$$

Using equation 5.11 and considering a maxwellian distribution for the absorbers:

$$\kappa_\nu = n_l \sigma_{lu}(\nu) \left[1 - e^{-h\nu/kT} \right] \tag{5.36}$$

The optical depth at frequency ν is dimensionless quantity that quantifies how opaque a medium is to radiation passing through it

$$d\tau_\nu = \kappa_\nu ds \tag{5.37}$$

With this definition, the radiation escapes in the direction of decreasing optical depth. Now equation 5.33 can be written as:

$$dI_\nu = -I_\nu d\tau_\nu + S_\nu d\tau_\nu \tag{5.38}$$

where $S_\nu \equiv J_\nu/\kappa_\nu$ is called the source function. The formal solution to equation 5.38 is integrating from the value $\tau_\nu = 0$ where the intensity is $I_\nu(0)$ to a generical value we obtain the former solution to the equation of radiative transfer in integral form:

$$I_\nu(\tau_\nu) = I_\nu(0)e^{-\tau_\nu} + \int_0^{\tau_\nu} e^{-(\tau_\nu - \tau_\nu')} S_\nu(\tau_\nu') d\tau_\nu' \tag{5.39}$$

The interpretation of this quation is that the intensity I_ν at optical depth τ_ν is the initial specific intensity $I_\nu(0)$ attenuated by a factor $e^{-\tau_\nu}$ plus the integral over the emission S_ν attenuated by the factor $e^{-(\tau_\nu - \tau_\nu')}$.

5.4 Spectral Line Shape

The spectral line profile is not a delta function and several mechanisms contribute to its form, from microscopic to large scale phenomena. Each leads to a different shape and, in principle, it is possible to understand the physical processes around the region in which the lines form.

5.4.1 Intrinsic and Thermal Broadening

First of all, there is the natural broadening due to the uncertainty principle. The principle says that there is an uncertainty measuring two complementary variables, in this case the energy of the level and its lifetime

$$E_i \cdot \tau_i \geq \frac{\hbar}{2} \tag{5.40}$$

This leads to a broadening in the profile function giving a Lorentzian profile described by equation 5.21.

As I said before, atoms, ions and molecules are in motion and hence there is a doppler broadening due to the thermal radial velocity field. Be

$$v_{th,i} = \sqrt{\frac{2k_B T}{m_i}} \tag{5.41}$$

the thermal velocity of species i. Then the Doppler width due to this velocity is

$$\Delta \nu_D \equiv \nu_0 \frac{v_{th,i}}{c} = \frac{\nu_0}{c} \sqrt{\frac{2k_B T}{m}} \tag{5.42}$$

This broadening changes the profile line function, giving as the final profile line function the convolution between the Lorenztian function (natural broadening) and the Gaussian function (thermal motion), called Voigt profile function as described in equation 5.24.

5.4.2 Turbulent Broadening

Microturbulence is a broadening mechanism that acts within the source, where the scale length for the (assumed homogeneous and isotropic) mass motioins is shorter than the pressure or density scale height. But turbulence broadening is much more difficult to handle because of a persistent ignorance regarding the probability distribution of the velocity field. It is possible to consider the turbulence introducing a component in the velocity field for modifying the Doppler width. Defining v_{turb} as the turbulence velocity, we get

$$\Delta \nu_D^{eff} = \frac{\nu_0}{c} \sqrt{v_{th}^2 + v_{turb}^2} \tag{5.43}$$

5.4.3   Rotation Broadening

An extrinsic broadening mechanism is due to rotation of the object relative to an external observer. When an object rotates, we see some parts of the star moving toward us and others in the opposite direction so a line broadens. This mechanism does not change the equivalent width. Measuring the HWZI of a line, it is possible to estimate the projected rotational velocity of an object toward the observer

$$v_{eq}\sin(i) = \frac{HWZI}{\lambda_0}c \tag{5.44}$$

where λ_0 is the wavelength at rest, v_{eq} is the equatorial rotational velocity and i is the inclination of the rotation axis to the line of sight assuming rigid body rotation.

5.4.4   Pressure Broadening

Collisions between the absorbing atom or ion and the other atoms or ions alter the level energies and lifetimes, thus producing collisional broadening or pressure broadening. The magnitude of this effect depends on the rate with which collisions occur with ambient particles depending on the thermal velocity, density n and on the collisional cross section σ_{col} as follows

$$\nu_{col} = v_{th}n\sigma_{col} \tag{5.45}$$

Then combining the natural and the collisional broadening gives an effective width

$$\Gamma = \gamma - 2\nu_{col} \tag{5.46}$$

and the natural plus collisionally broadened line profile is

$$\phi_\nu = \frac{\Gamma}{4\pi^2[(\nu - \nu_0)^2 + (\Gamma/4\pi)^2]} \tag{5.47}$$

An other form of line broadening is due to the interaction of the stochastic ambient fluctuating electric field with the medium. This is called *Stark* effect. When an electric field $\mathbf{E}_0$ interacts with the medium, the Hamiltonian gains a term V_E that represents the interaction. The tolal Hamiltonian becomes:

$$H = H_0 + V_E \tag{5.48}$$

where H_0 is the unperturbed Hamiltonian, $V_E = -\boldsymbol{\mu}_d \cdot \mathbf{E}_0$ is the interaction potential and $\boldsymbol{\mu}_d$ is the electric dipole moment.

Chapter 6

Physical Processes behind the B[e] Phenomenon

In this chapter I will describe the physical processes that occour in the objects that show the B[e] phenomenon trying to pointing out which phenomena are playing a role in IRAS 17449 + 2320. Hence the spherical symmetry breaking, the formation of the sorrounding disk, the origin of the Balmer instabilities and the possibility of binarity.

6.1   B[e] classical picture

As said in chapter 1, B[e] objects are stars that show forbidden and permitted emission lines with an IR excess. These phenomena are due to the presence of a gaseous and dusty envelope around the star, usually forming a disk-like or ring-like structure. Because it is an heterogeneous group of objects in different evolutive phases with different masses, these object can present the same phenomenon but caused by different physical triggering phenomena like like wind, rotation, mass loss and binarity.

6.2   Main characteristics of stellar winds

Stars emit radiation but also particles. The emission of the particles is called stellar winds. In case of IRAS $17449 + 2320$ there is no clear evidence of it. This can be consistent with the fact that late B and early A type stars have weak stellar wind. However, I discuss briefly the main properties and parametrization of a stellar wind because even a weak wind with the presence of rotation can lead to formation of a disk. The two main parameters regarding a stellar winds that can be derived from observations are the amount of mass lost by the star per unit time $\dot{M}$ and the terminal velocity v_∞ which is the wind velocity at very large distance from the star $(v_\infty = v(r \to \infty))$. Usually $\dot{M}$ is expressed in units of solar masses per year with 1 $M_\odot$ yr^{-1} = 6.303$\cdot 10^{25}$ g s^{-1}, instead v_∞ is expressed in units of km s^{-1}. $\dot{M}$ is important because it describes how much material is lost by the star per unit of time and this is important for the evolution of the stars. Different stellar wind theories predict different mass loss rates and different terminal velocities for a given star. So by comparing the observed values with the predictions, we can learn which mechanism is responsible for the mass loss from a star.

The ejection of material from a star carries kinetic energy to the ISM. This amount of kinetic energy per unit of time is $E_k = 0.5\dot{M}v_\infty^2$. We can write the amount of mass loss rate for a stationary spherically symmetric wind:

$$\dot{M} = 4\pi r^2 \rho(r) v(r) \tag{6.1}$$

where r, $\rho(r)$, and $v(r)$ are respectively the distance from the center of the star, the density and the velocity as a fuction of the distance r. This equation is important because it states that no material is destroyed nor created in the stellar wind, so the same amount of gas flows per second through a sphere at any radial distance from the center of the star. The material that escapes from the outer layers of the stars is accelerated outwards until $v(r)$ asymptotically approaches the terminal velocity v_∞. The distribution of the velocity of the wind with radial distance from the star is called velocity law. Observations and models of the stellar winds indicate that this law can often be approximated by a $\beta - law$ (see [40]):

$$v(r) \simeq v_0 + (v_\infty - v_0) \left(1 - \frac{R_\star}{r}\right)^\beta \tag{6.2}$$

This law says that the velocity increases with distance from v_0 at $r = R_\star$ and the parameters β describes how steep the velocity law is. Hot stars, like O stars, have winds with a $\beta \approx 0.8$ and their winds experience a

fast acceleration and reach 80% of their v_∞ at $r = 4.1R_\star$. Instead, winds of cool stars accelerate more slowly, corresponding to larger values of β.

There is an alternative form of the $\beta - law$ that has the advantage that it is easier to handle in integral equations:

$$v(r) \simeq v_\infty \left(1 - \frac{r_0}{r}\right)^\beta \tag{6.3}$$

with

$$r_0 = R_\star \left(1 - \left(\frac{v_0}{v_\infty}\right)^{1/\beta}\right) \tag{6.4}$$

In figure 6.1 we can see the variation of the $v(r)$ as a function of the distance r for different values of β.
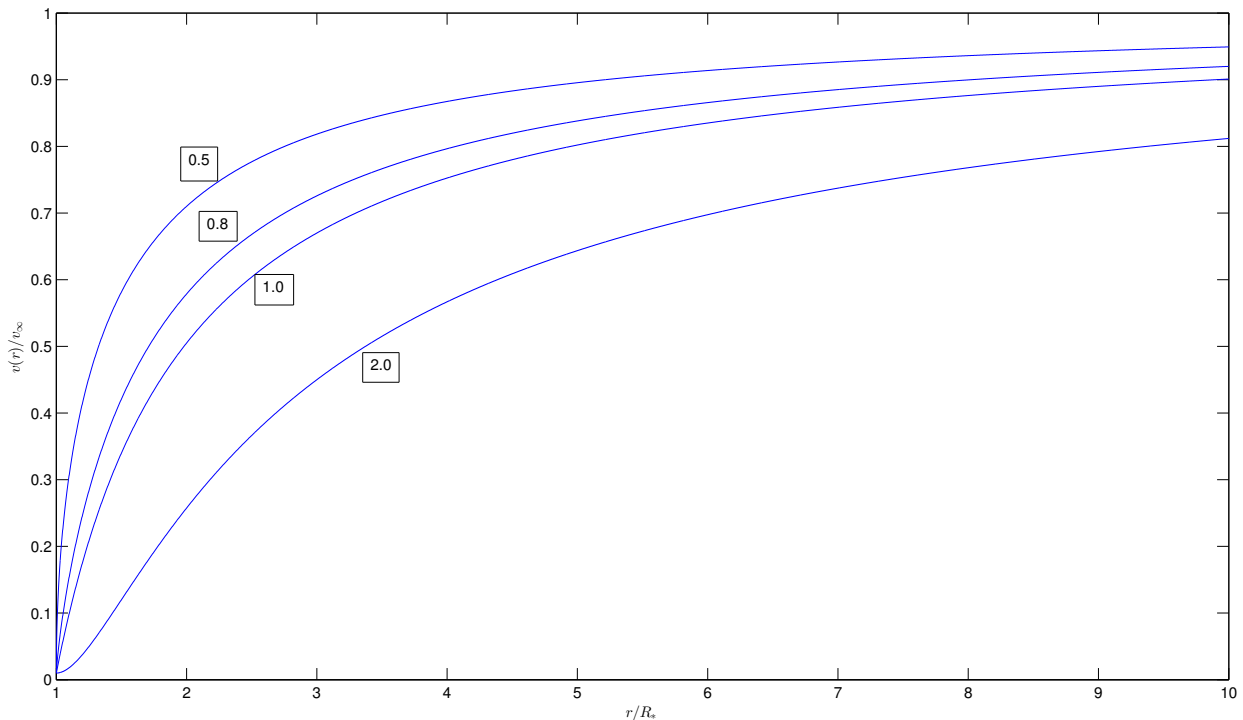
Figure 6.1: β-law for stellar winds for several values of β (in the boxes), with $v_0 = 10^{-2} \, v_\infty$.

6.3 Rotation and decretion disk

I found that IRAS 17449+2320 has a projected rotational velocity of about 200 km s^{-1}. Early-type stars usually show rotationally broadened photospheric lines that indicates that their rotational velocity is up few hundreds of kilometers per second ([40]). The rotation brings interesting effects, like the formation of an outflowing disk (also called decretion disk) in the equatorial plane and the broadening of absorption and emission lines. Two examples of early-type emission line stars that show the presence of an equatorially enhanced winds are the Be and the B[e] stars. These two kind of stars have a much stronger emission from Balmer lines and a much stronger infrared excess due to the free-free emission than normal early-type stars. The emissivity is proportional to the square of the density and hence the presence of strong Balmer emission means that there must be a region in the wind with a much higher density than normal wind.

The presence of a double peaked profile in the Balmer emission lines means rotation and rather small outflow velocity of few hundreds of kilometers per second. This means that the high density region is in the equatorial plane and also that the outflow velocity in this plane is smaller than that at higher latitudes. A confirm of this picture is given by the study of the polarization from this kind of stars. If the wind is spherically symmetric, then the light is not polarized, because the polarized intensity produced in a region will be deleted from the light formed in a 90 degree sector away. Instead, if the star rotates, most of the scattering of the photons occur in the regions containing the equatorial plane. This enhancement in the scattering can produce a net polarization

of the radiation. So empirical models of Be and B[e] stars must take into account the two components of the wind. There is a fast component consistent with a line driven model and a second slow and dense equatorial component moving outward.

In the next paragraphs, I will introduce the effect of rotation and two models for describing the wind, even if weak, in a presence of a decretion disk. These models are the *Rotation Induced Bi-stability* model and the *Wind Compression* model.

6.3.1   Effects of rotation

Rotation breaks the spherical symmetry and hence the structure of the atmosphere and wind. Using a Roche model, where the hydrostatic photospheric region of a star is rotating as a solid body with angular velocity Ω and the gravitational force is assumed to be radial. The hydrostatic equilibrium equation is

$$\frac{1}{\rho}\nabla P = -\nabla\left(\Phi_G + \Phi_\Omega\right) = -\nabla\Phi \tag{6.5}$$

where Φ_G and Φ_Ω are the gravitational potential and the centrifugal potential. Assuming a solid body rotation, we get

$$\Phi = \frac{GM_\star}{r} - \frac{1}{2}\left(r\Omega\sin\theta\right)^2 \tag{6.6}$$

where θ is the polar angle starting from the pole. So the rotation distorts the equipotential surfaces. Setting the potential $\Phi = \Phi(R_0)$, where R_0 is the polar radius of the isopotential surface where $\Phi = GM_\star/R_0 = constant$, and using equation 6.6 it is possible to write the following equation

$$R^3(\theta) - \frac{2GM_\star}{R_0\Omega^2\sin^2\theta}R(\theta) + \frac{2GM_\star}{\Omega^2\sin^2\theta} = 0 \tag{6.7}$$

where the solutions describe the equipotential surfaces as shown in figure 6.2.
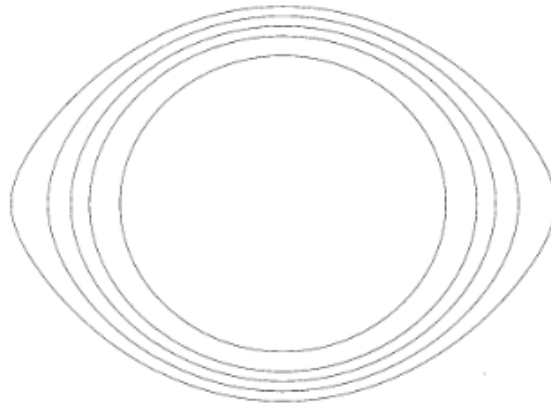
Figure 6.2: Projected equipotential surfaces satisfying the Roche model. In this case $\Omega R_0 = 0.54\sqrt{GM_\star/R_0}$. Image taken from Lamers and Cassinelli ([40]).

Because of equation 6.5, the pressure gradient is perpendicular to equipotential surfaces and hence these surfaces are equipressure surfaces. Also, taking the curl of equation 6.5 and applying the property that the curl of a gradient of any scalar field is the zero vector field, it is possible to find that

$$\nabla\rho \wedge \nabla P = 0 \tag{6.8}$$

hence the equipotential surfaces are also surfaces at constant density. If we assume a perfect gas law equation of state, we get that the equipotential surfaces are also equitemperature surfaces. Hence the radiation field is a function of latitude. Taking the Planck function $\mathscr{B}_\nu$ as the radiation field source function, with the property that $\mathscr{B}_\nu$ is constant at equipotential surfaces, it is possible to write the flux like a diffusion equation

$$\mathscr{F} = -\frac{4\pi}{3\kappa\rho}\frac{d\mathscr{B}}{d\Phi}\|\nabla\Phi\| \tag{6.9}$$

where κ is the Rosseland mean opacity and $\mathscr{B}$ is the integrated Planck function and hence is proportional to T^4. Knowing that the local net gravity is proportional to the opposite of the potential gradient, we obtain that the flux $\mathscr{F}$ is proportional to the local net gravity $\mathbf{g}_{net} = -\nabla\Phi$. This is the *Von Zeipel theorem*.

Looking better at figure 6.2, it is possible to note that, near the pole, the equipotential surfaces are closer than at the equator. This means that the temperature gradient is steeper in the pole respect to the temperature gradient in the equatorial zone. Hence, the radiative flux is larger at the pole. This phenomenon is called *polar brightening* or *gravity darkening*. Another effect of rotation is that the star has a larger radius at the equator than at the pole. There is a critical velocity for the rotation

$$v_{cri} = \left(\frac{GM_\star}{R_\star} \right)^{1/2} \tag{6.10}$$

but it is useful to define an adimensional parameter ω for describing the rotational speed

$$\omega = \frac{v_{rot}}{v_{cri}} \tag{6.11}$$

where ω has a maximum value of unity. Putting an estimate for the $M_\star \approx 2.3$ M$_\odot$ and $R_\star \approx 3$ R$_\odot$, I obtain $\omega \approx 0.55$ (neglecting $\sin(\theta)$ in the projected rotational velocity).

6.3.2 Rotation Induced Bi-stability mechanism

Due to the rotation, the gravity depends on latitude θ and hence there is a reduction in the effective gravity from poles to equator. This enhances the optical depth in the wind toward the equator, and if the optical depth changes from a value smaller than one near the pole to a value greater than one near the equator, then the bi-stability jump occurs at a specific latitude. The bi-stability jump forms a slower and denser wind in the equatorial region respect to the one in the pole regions. The net gravity depends on the latitude as

$$g_{net} = \frac{GM_\star (1 - \Gamma_e)}{R^2(\theta)} \left(1 - \omega^2 \sin^2 \theta \right) \tag{6.12}$$

The wind speed in radiation driven wind theory is proportional to the escape speed, hence

$$v_\infty(\theta) \propto v_{esc}(\theta) \propto \sqrt{R(\theta) g_{net}(\theta)} \propto \sqrt{\frac{(1 - \omega^2 \sin^2 \theta)}{R(\theta)}} \tag{6.13}$$

So the wind speed decreases from the pole to the equator, but the mass flux increases.

6.3.3 Wind Compression Disk Model

Taking two parcels of wind of a rotating star at opposite latitude and same longitude starting from the photosphere at the same time, they will follow a trajectory in a plane that includes the launch point and the center of the star. Hence, the two planes have a common point in which the two parcels of wind collide. This point in in the equatorial plane. But the parcels are launched from every longitude and latitude, hence a compression region will form at the equator. This is at the base of the wind compression model developed by Bjorkman and Cassinelli ([10]). In case that this density enhancement creates shocks then the model is called *Wind Compressed Disk or WCD*.

From a dynamical point of view there are four forces to take into account due to: radiation, pressure gradient, gravity and rotation. In a rotating star, beyond the sonic point, the gravity exceeds the force due to radiation, hence there is a net component of the radial force toward the equator and the parcel of gas is not pushed away totally. So, if the gas has a supersonic component of velocity in the direction of the equator, a shock zone or disk will develope. The shock leads to a significant enhancement in density in this region and also in temperature. Figure 6.3 illustrates the formation of a shock region and a dense disk in a WCD fashion.

The material that passes through the shock and enters in the equatorial region, the material becomes subsonic and the gas pressure gradient determines the streamlines of the flow. The shock leads, also to an inflow plus outflow velocity structure of the disk. There is a stagnation point $r_{v=0}$ where for $r < r_{v=0}$ the gas velocity has negative values and hence there is an inflow stream, instead for $r > r_{v=0}$, the gas velocity has positive values and hence there is an outflow stream.

6.3.4 Differences between RIB and WCD model

There are two main differences between RIB and WCD model:

a) In the RIB model, the formation of the disk is due to the enhancement of the mass flux in the equatorial plane, instead in the WCD model, the disk formation is due to the compression of the wind toward the equator.
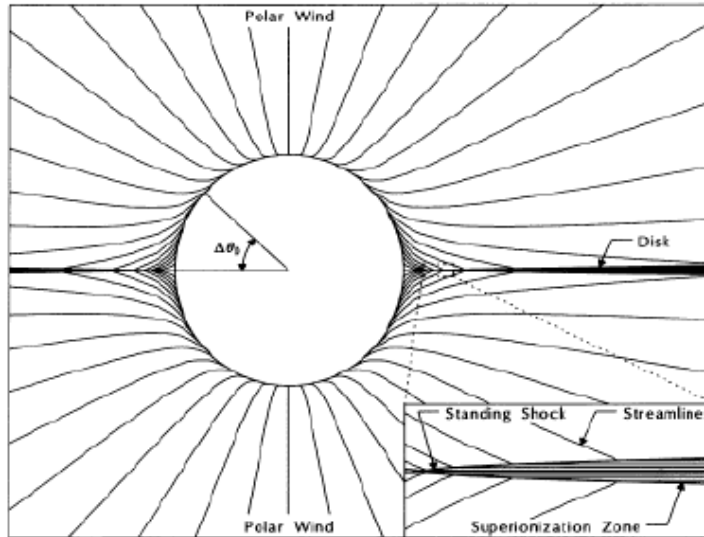
Figure 6.3: Illustration of WCD model that leads to a formation of a shock and a disk. Image taken from Lamers and Cassinelli ([40]).

b) Numerically, the RIB model gives at most a factor of ten in the density contrast between the pole and the equator, and this seems to be good for B supergiants with high mass loss rates. Instead the WCD model can produce a higher density contrast and this does not depends on the mass loss rate.

Hence a combination of the two models will leads to a higher density contrast producing a higher mass loss rate in the equatorial plane and concentrating the flow toward the equator.

6.4 Fe II, Na I D, O I and Ca II profiles

B[e] objects have disk and it is inclined respect the direction toward us, part of the light that would have not reached us could interact with the disk and being scattered toward us. Translating this into a spectroscopic effect, part of the flux will be absorbed by the gaseous part of the disk, but other part of the flux will be scattered forming emission lines. The sum of the two components gives a profile with core in absorption and wings in emission explaining the peculiar profile of Na I D, Fe II, O I and Ca I. If wee see reflection from a disk but also absorption lines formed through the disk, this put a constrain on the angle between the rotational axis of the star and us. In particular, this means that this angle must be greater than 50 degree, because we must see the disk both in absorption and in emission.

Another explaination to the Fe II, Na I D, Ca II and O I profiles is the UV pumping but unfortunately the spectra do not cover that range in wavelength.

6.5 Lines variation

As said before, I found variation in Balmer lines but also in the other lines even if weak. It is clear the presence of transient composite absorption features moving from the blue to the red side of the line. The phenomenon behind this variation is appreciable within few days. In different systems, some authors put the origin of similar variation to a presence of transient structures orbitinig around the center of mass.

Okazaki ([58], [57]) constructed a model first suggested by Kato ([33]) in which the long-term V/R variations are due to global one-armed (i.e. azimuthal wave number $m = 1$) oscillations in the equatorial discs of Be stars. The model is based on the theoretical result that the low-frequency, one-armed oscillations are the only possible global oscillations in geometrically thin (i.e. near Keplerian) discs (Kato [33], Okazaki and Kato [59], Adams et al. [2]). Studying the linear m = 1 eigenmodes in isothermal equatorial discs, Okazaki found that the one-armed oscillation model well explains the observed periodicity of the long-term V/R variations.

Lecavelier Des Etangs et al. ([42], [43]) studying the spectral variation of β Pic pointed out the possibility of the evaporation of a planet forming a multi-cometary tail.

For IRAS 17449+2320, the cause of the line variation is not clear . The perturbation induces a change in the optical depth and consequently, when it moves, forms composite absorption features in the spectrum. A rough estimation of the distance, the period and the subtended angle of the perturbation (solid bodies or spiral arm)

can be done assuming Keplerian motion. Putting $\Delta v \approx 150$ km s^{-1} as a variation in velocity of the absorption features, $\Delta t \approx 5$ days the timescale for the variation and $M_\star \approx 2.3$ M$_\odot$ the mass of the star, I obtain

$$D = \left(\frac{GM_\star \Delta t}{\Delta v} \right)^{1/2} \approx 0.2 \text{ AU} \qquad (6.14)$$

where D is the rough estimate of the distance of the perturbation from the star. It this transient structure is orbiting around the star, the period of the orbit is

$$P = 2\pi \left(\frac{D \Delta t}{\Delta v} \right)^{1/2} \approx 21 \text{ days} \qquad (6.15)$$

and the subtended angle by the transition of the structure respect the star is

$$\theta = \frac{\Delta t}{P} \cdot 360 \text{ degree} \approx 85 \text{ degree} \qquad (6.16)$$

The lengthscale D indicates that the perturbation is occouring in the inner region of the disk, where the radiaiton field has a temperature of $T_{rad} \approx 2900$ K ($T_\star \approx 11000$ K). In this region dust can not exist but a gaseous environment composed by singly ionized species with low energy excitation level does. Infact all the line transitions of singly ionized species found are from low energy excitation level. This is in agree with the classical picture of a disk in the B[e] object.

Hα has a different behaviour than other Balmer lines. I found a double peak profile where the V/R ratio is the most variable quantity. Reipurth et al. ([68]) studied the variation of Hα profile in a survey on pre main sequence star (T Tauri, Herbig Ae/Be and FU Orionis objects). This kind of objects presents a similar geometry structure as B[e]. They found evidence that Hα line might result from the combined contribution of more than one regions, and that the variable component of the line affects mainly the blue side and the central region of the profile and has to be produced in a relatively narrow and dense region, close to the stellar surface. This can explain the strong correlation between the V/R ratio and the central depression residual during SPM2015.

6.6   Binarity

Binarity is one of the key to understand the B[e] phenomenon. A system composed by (at least) two stars can undergoes to phenomena like mass transfer, changing the fate of the two components. It is possible to observe binarity in the spectrum looking for lines that clearly indicate two different spectral types and with different radial velocity. But if the companion is a low mass MS star, e.g. M$_{sec} = 0.5$ M$_\odot$, the luminosity depends on the mass as $L_{sec}/L_\odot = (M_{sec}/M_\odot)^4$ (see [70]) and so the luminosity ratio between the secondary and the primary is $L_{sec}/L_{pri} \approx 2 \cdot 10^{-3}$ and with veiling the lines could be missed. Alternatively, there could be a substellar mass companion (a brown dwarf or planetary mass body) that's responsible for driving a disk instability by tidal resonances. Another scenario is the evolution of a binary system in which an AGB star starts to expand its cool envelope beyond the Roche lobe forming a circumstellar envelope. The remaining core is a degenerate star of ≈ 0.8 M$_\odot$ becoming the secondary star of the system. Hence binarity cannot be ruled out.

6.7   Reddening

Interstellar medium (ISM) alters the light from the stars. Through scattering and absorptions due to gas and dust, the photons are lesser and reddened. IS Na I D lines are used to quantify this reddening. Since V= (10.01 ± 0.02) mag and B= (10.04 ± 0.02) mag ([24]), $(B - V)_{obs} = (0.03 \pm 0.03)$ mag. Integrating the profile of the 21 cm H I (see figure 4.65) and we can get an estimate of the neutral hydrogen column density $N_H = 7.2 \cdot 10^{19}$ cm^{-2} and then calculate the correction for the interstellar reddening $(B - V)_{cor} = 0.01$ mag. So the intrinsic reddening of IRAS $17449 + 2320$ is $(B - V)_{obs} - (B - V)_{cor} \approx 0.02 \pm 0.03$ mag. This value says that the object is essentially unreddened, hence the dust does not lie along the line of sight.

6.8   Analogy with Seyfert Galaxies

Seyfert objects are a group of active galaxies showing high ionization emission lines. The spectra of Seyfert galaxies type I show broad lines that include both allowed lines, like H I, He I or He II and narrower forbidden lines, like O III. Broad lines have widths in the range $[10^3, 10^4]$ km s^{-1}, instead narrow lines have a width up to 10^3 km s^{-1}. The broad lines originate above the accretion disc of the supermassive black hole, while the narrow lines occur beyond the broad line region of the accretion disc ([60]). Substituting the supermassive black hole

with a B type star and rescaling the size, we get the same geometrical picture of an object that shows the B[e] phenomenon. In case of IRAS $17449 + 2320$, the emission lines are from low ionized and neutral species and have widths much lower than Seyfert galaxies type I, but broad lines (up to 300 km s^{-1}) are from permitted transitions and seems to form in the near the central object, instead narrow lines are from forbidden transitions ([O I] has a widths up to 30 km s^{-1}) and form in a wider environment.

Chapter 7

Conclusions

In this thesis, I have analyzed the spectra of a B[e] object called IRAS $17449 + 2320$. The object was classified as a 10 mag A0V star and a possible FS CMa object and it was first discovered by IRAS telescope, so identified as infrared source. This excess in IR spectrum is due to the presence of dust in the environment around the star, because the B[e] stars are good dust producer.

IRAS $17449 + 2320$ was monitored by four observatory: the CFHT for three non consecutive nights, the Ondřejov for a period of eight years, the McDonald for one night and the SPM for six consecutive days. From the data of these observatories, I have done a spectroscopic analysis focused on the line profile variability of several lines (e.g. Balmer lines, O I, Si II, Ca II, Mg II, Fe II, Na I, He I etc.) trying to infer the physical phenomena and structure at different distance from the central object.

The Balmer lines have broad wings in absorption wide 3600 km s^{-1} (FWZI) but the core is composite by emission and absorption features. The variation of Balmer lines is only in the core and in the range of velocity of $[-300, 300]$ km s^{-1}, this means that the dynamical phenomena that are affecting these lines are playing at a distance lesser than an AU. Ca II, O I, Na I D, Fe II (multiplet 42) have an absorption core and emission wings. These wings are broad as the range of velocity where the dynamical phenomena are affecting the Balmer lines. This can suggest that these lines are forming in the same region of the perturbations and they are perturbed too, even if with weaker variations. I found in the Balmer lines, the presence of composite absorption features moving from the blue to the red side with a time scale of few days, changing their velocity of 200 km s^{-1}. This can be explained by the presence of coherent but temporary structures that are orbiting around the star at about 0.2 AU where the radiation has a temperature of about $\approx$ 2900 K. These rotating coherent structures change the optical depth and so the central depression residual and hence the violet peak, this leads to a V/R ratio variability seen in the Hα. Infact I found a high correlation between the central depression residual and the V/R ratio. But looking at all the data available for the V/R ratio, it is clear that the object passes through different phases, in which sometimes these coherent structures are formed and orbit around the star. The nature of this perturbation is not clear, although for other stellar systems Okazaki ([58], [57]) suggests the hypothesis of global one-armed oscillations and Lecavelier Des Etangs et al. ([42], [43]) pointed out the possibility of the evaporation of a planet forming a multi-cometary tail. Returning to Ca II, O I, Na I D, Fe II (multiplet 42), their emission wings can be explained by two different scenarios: one is the scattering from the disk and the second is the UV pumping. From the O I Grotrian diagram (figure 4.60), I found that Lyβ and nearby photons can pump the O I lines and the Hα but the hypothesis that [O I] are pumped by collisions cannot be ruled out.

[O I] emission lines are forming in a wider region in which the dynamical phenomena do not vary the line. Hence it is possible to use the doppler shift of these lines as an indicator of the radial velocity of the system that is RV= (-16 ± 2) km s^{-1}. An anlogy with Seyfert galaxies type I can be done rescaling the size and the strength of the phenomena but also substituting the supermassive black hole with a B type star. The broad emission lines are formed near the central object, instead the narrow emission lines are from a wider region.

The comparison between a rotated Vega line profile and Balmer lines suggests that IRAS $17449 + 2320$ has a projected rotational velocity about $v_{eq} \sin(\theta) \approx 200$ km s^{-1}. Hence the star is a fast rotator. Unfortunately, the angle θ between us and the rotational axis of the star is not known. The presence of the He I lines, even if they are weak, and Paschen lines are an indicator of the spectral type of the star. This means that the star could be earlier than it thought in the literature (A0V) but not earlier than a B8V type ([20]).

From CFHT spectra, the ones used for the lines identification, a variation in the shape of Fe II and He I lines emerges. In the third CFHT spectrum (MJD= 4671.60), the flux residual of the Fe II lines are stronger than the ones from the other two CFHT spectra but the He I is weaker. It seems that the behaviour of Fe II and He I is in antiphase. This could be related to a variation in the radiation field of the central source, especially in the UV part of the spectrum that unfortunately is not covered by the available observations. Multi timescale for line variations is found: few days for Balmer lines, and month or years for the other lines. FS CMa objects show sometimes binarity, but I do not find evident trace of spectral lines referable to a companion. But this

is not enough to rule out the binarity. Infact, in the case of a low mass MS star (e.g. $M_{sec} = 0.5\ M_\odot$), the luminosity ratio between the secondary and the primary is $L_{sec}/L_{pri} \approx 2 \cdot 10^{-3}$ and with veiling the lines could be missed. Alternatively, there could be a substellar mass companion (a brown dwarf or planetary mass body) that's responsible for driving a disk instability by tidal resonances. Another scenario is the evolution of a binary system in which an AGB star starts to expand its cool envelope beyond the Roche lobe forming a circumstellar envelope. The remaining core is a degenerate star of $\approx 0.8\ M_\odot$ becoming the secondary star of the system. Hence binarity cannot be ruled out.

I found that the central object is, within the errors, unreddened and hence the dust does not lie in the line of sight. After this spectroscopic analysis of IRAS $17449 + 2320$ open questions still exist and further analysis should be done. What are the physical phenomena that produce the Balmer variability? Is it a planet or global one-arm oscillations? Does this system show binarity? And what about photospheric and/or wind magnetic structures? Could these phenomena lead to transient structures in the circumstellar environment? What is the dust production rate? What causes the antiphase between He I and Fe II? Why are [Fe II] lines absent? Unfortunately, this object is too faint for optical and IR interferometry. But time-dependent IR, UV, optical and spectropolarimetric observations are possible and needed to study these coherent structures, the geometrical distribution around the star, the possible binarity, the presence of dust and of a magnetic field.

Bibliography

[1]   In: *IAU Colloq. 70: Be and Shell Stars*. Vol. 70. Jan. 1976, b1–b1. DOI: 10.1017/S0074180900011633. URL: http://journals.cambridge.org/article_S0074180900011633.

[2]   F. C. Adams, S. P. Ruden, and F. H. Shu. "Eccentric gravitational instabilities in nearly Keplerian disks". In: *ApJ* 347 (Dec. 1989), pp. 959–976. DOI: 10.1086/168187.

[3]   D. A. Allen and J. P. Swings. "The spectra of peculiar Be stars with infrared excesses". In: *A&A* 47 (Mar. 1976), pp. 293–302.

[4]   V. Antoci. "Stochastically excited oscillations in the upper main sequence". In: *Precision Asteroseismology*. Ed. by J. A. Guzik et al. Vol. 301. IAU Symposium. Feb. 2014, pp. 333–340. DOI: 10.1017/S1743921313014543. arXiv: 1311.1149 [astro-ph.SR].

[5]   A. Aret, M. Kraus, and M. Šlechta. "Spectroscopic survey of emission-line stars - I. B[e] stars". In: *MNRAS* 456 (Feb. 2016), pp. 1424–1437. DOI: 10.1093/mnras/stv2758. arXiv: 1511.07270 [astro-ph.SR].

[6]   J. P. Aufdenberg et al. "First Results from the CHARA Array. VII. Long-Baseline Interferometric Measurements of Vega Consistent with a Pole-On, Rapidly Rotating Star". In: *ApJ* 645 (July 2006), pp. 664–675. DOI: 10.1086/504149. eprint: astro-ph/0603327.

[7]   H. H. Aumann. "IRAS observations of matter around nearby stars". In: *PASP* 97 (Oct. 1985), pp. 885–891. DOI: 10.1086/131620.

[8]   D. Baade. "Non-radial pulsations in relation to wind variability in early-type stars". In: *Cyclical Variability in Stellar Winds*. Ed. by L. Kaper and A. W. Fullerton. Springer-Verlag, 1998, p. 415.

[9]   J. E. Bjorkman. "Circumstellar Disk Models for B[e] Supergiants". In: *Stars with the B[e] Phenomenon*. Ed. by M. Kraus and A. S. Miroshnichenko. Vol. 355. Astronomical Society of the Pacific Conference Series. Dec. 2006, p. 231.

[10]   J. F. Bjorkman and J. P. Cassinelli. "The Wind Compressed Disk Model of Be Stars (Invited Paper)". In: *Nonisotropic and Variable Outflows from Stars*. Ed. by L. Drissen, C. Leitherer, and A. Nota. Vol. 22. Astronomical Society of the Pacific Conference Series. 1992, p. 88.

[11]   H. Cao and J. Dachs. "Stellar wind variability of Be star FY CMa". In: *Cyclical Variability in Stellar Winds*. Ed. by L. Kaper and A. W. Fullerton. Springer-Verlag, 1998, p. 415.

[12]   A. C. Carciofi, A. S. Miroshnichenko, and J. E. Bjorkman. "Toward Understanding the B[e] Phenomenon. IV. Modeling of IRAS 00470+6429". In: *ApJ* 721 (Oct. 2010), pp. 1079–1089. DOI: 10.1088/0004-637X/721/2/1079. arXiv: 1007.4709 [astro-ph.SR].

[13]   P. W. Cauley and C. M. Johns-Krull. "Optical Mass Flow Diagnostics in Herbig Ae/Be Stars". In: *ApJ* 810, 5 (Sept. 2015), p. 5. DOI: 10.1088/0004-637X/810/1/5. arXiv: 1506.07546 [astro-ph.SR].

[14]   C. de Jager and G. Israelian. "Rapid variations of narrow absorption line components in the spectrum of P Cygni". In: *NA* 8 (July 2003), pp. 475–479. DOI: 10.1016/S1384-1076(03)00018-6. eprint: astro-ph/0304357.

[15]   D. de la Fuente et al. "First detections of FS Canis Majoris stars in clusters. Evolutionary state as constrained by coeval massive stars". In: *A&A* 575, A10 (Mar. 2015), A10. DOI: 10.1051/0004-6361/201425371. arXiv: 1412.7988 [astro-ph.SR].

[16]   J.-F. Donati. "ESPaDOnS: An Echelle SpectroPolarimetric Device for the Observation of Stars at CFHT". In: *Solar Polarization*. Ed. by J. Trujillo-Bueno and J. Sanchez Almeida. Vol. 307. Astronomical Society of the Pacific Conference Series. 2003, p. 41.

[17]   B. T. Draine. *Physics of the Interstellar and Intergalactic Medium*. Princeton University Press, 2011, p. 560.

[18]   J. A. Eaton. "Variations of winds of cool giants in Hα". In: *Cyclical Variability in Stellar Winds*. Ed. by L. Kaper and A. W. Fullerton. Springer-Verlag, 1998, p. 415.

[19]   S. L. Geisel. "Infrared Excesses, Low-Excitation Emission Lines, and Mass Loss". In: *ApJ* 161 (Aug. 1970), p. L105. DOI: `10.1086/180580`.

[20]   R. O. Gray and J. C. Corbally. *Stellar Spectral Classification*. Princeton University Press, 2009, p. 592.

[21]   V. Grinin. "Anisotropic outflows from Herbig Ae/Be stars". In: *Cyclical Variability in Stellar Winds*. Ed. by L. Kaper and A. W. Fullerton. Springer-Verlag, 1998, p. 415.

[22]   A. F. Gulliver, G. Hill, and S. J. Adelman. "Vega: A rapidly rotating pole-on star". In: *ApJL* 429 (July 1994), pp. L81–L84. DOI: `10.1086/187418`.

[23]   G. Hill, A. F. Gulliver, and S. J. Adelman. "A Study of Vega: A Rapidly Rotating Pole-On Star". In: *ApJ* 712 (Mar. 2010), pp. 250–259. DOI: `10.1088/0004-637X/712/1/250`.

[24]   E. Høg et al. "The Tycho-2 catalogue of the 2.5 million brightest stars". In: *A&A* 355 (Mar. 2000), pp. L27–L30.

[25]   I. D. Howarth et al. "Time-Series Observations of O Stars. III. IUE and HST Spectroscopy of zeta Ophiuchi and Implications for the "Photospheric Connection"". In: *ApJ* 417 (Nov. 1993), p. 338. DOI: `10.1086/173316`.

[26]   G. Israelian. "Rotating loops in the atmosphere of Rigel (β Orionis A)". In: *Cyclical Variability in Stellar Winds*. Ed. by L. Kaper and A. W. Fullerton. Springer-Verlag, 1998, p. 415.

[27]   G. Israelian. "Rotating loops in the atmosphere of Rigel (β Orionis A)". In: *Cyclical Variability in Stellar Winds*. Ed. by L. Kaper and A. W. Fullerton. Springer-Verlag, 1998, p. 415.

[28]   G. Israelian et al. "The variable mass loss of the peculiar supergiant P Cygni." In: *MNRAS* 283 (Nov. 1996), pp. 119–136. DOI: `10.1093/mnras/283.1.119`.

[29]   T. Jeřábková et al. "Time-dependent spectral-feature variations of stars displaying the B[e] phenomenon. III. HD 50138". In: *A&A* 586 (Feb. 2016), A116. DOI: `10.1051/0004-6361/201526290`. arXiv: `1512.02506` `[astro-ph.SR]`.

[30]   C. M. Johns-Krull. "Wind and accretion variability in T Tauri stars". In: *Cyclical Variability in Stellar Winds*. Ed. by L. Kaper and A. W. Fullerton. Springer-Verlag, 1998, p. 415.

[31]   P. M. W. Kalberla et al. "The Leiden/Argentine/Bonn (LAB) Survey of Galactic HI. Final data release of the combined LDS and IAR surveys with improved stray-radiation corrections". In: *A&A* 440 (Sept. 2005), pp. 775–782. DOI: `10.1051/0004-6361:20041864`. eprint: `astro-ph/0504140`.

[32]   L. Kaper et al. "Cyclical variability in O star winds". In: *Cyclical Variability in Stellar Winds*. Ed. by L. Kaper and A. W. Fullerton. Springer-Verlag, 1998, p. 415.

[33]   S. Kato. "Low-frequency, one-armed oscillations of Keplerian gaseous disks". In: *PASJ* 35 (1983), pp. 249–261.

[34]   A. Kaufer. "Cyclic variability in BA-type supergiants". In: *Cyclical Variability in Stellar Winds*. Ed. by L. Kaper and A. W. Fullerton. Springer-Verlag, 1998, p. 415.

[35]   A. B. Kaye and D. R. Gies. "On the Line Profile Variations and Nonradial Pulsation Modes of ζ Tauri (HD 37202)". In: *ApJ* 482 (June 1997), pp. 1028–1037.

[36]   A. Kramida, Yu. Ralchenko, and J. Reader. *NIST Atomic Spectra Database*. 2015. URL: `http://physics.nist.gov/asd`.

[37]   J. Krempec-Krygier, M. Schmidt, and K. Gesicki. "Variability of the circumstellar shell of 89 Herculis". In: *Cyclical Variability in Stellar Winds*. Ed. by L. Kaper and A. W. Fullerton. Springer-Verlag, 1998, p. 415.

[38]   B. Kučerová et al. "Time-dependent spectral-feature variations of stars displaying the B[e] phenomenon. II. MWC 342". In: *A&A* 554, A143 (June 2013), A143. DOI: `10.1051/0004-6361/201117437`.

[39]   A. M. Lagrange et al. "GHRS Observations of the Extrasolar Protoplanetary System βPictoris". In: *Science with the Hubble Space Telescope - II*. Ed. by P. Benvenuti, F. D. Macchetto, and E. J. Schreier. 1996, p. 532.

[40]   H. J. G. L. M. Lamers and J. P. Cassinelli. *Introduction to Stellar Winds*. Cambridge University Press, 1999, p. 452.

[41]   H. J. G. L. M. Lamers et al. "An improved classification of B[e]-type stars". In: *A&A* 340 (Dec. 1998), pp. 117–128.

[42]   A. Lecavelier Des Etangs, A. Vidal-Madjar, and R. Ferlet. "Dust distribution in disks supplied by small bodies: is the β Pictoris disk a gigantic multi-cometary tail?" In: *A&A* 307 (Mar. 1996), pp. 542–550. eprint: `astro-ph/9508035`.

[43] A. Lecavelier des Etangs et al. "Perturbations of a Planet on the β Pictoris Circumstellar Dust Disk. 3. Time Scale of Collisional Destruction versus Resonance Time Scale". In: *ICARUS* 123 (Sept. 1996), pp. 168–179. DOI: `10.1006/icar.1996.0147`.

[44] N. Markova. "New aspects of line-profile variability in P Cygni's optical spectrum". In: *A&AS* 144 (June 2000), pp. 391–404. DOI: `10.1051/aas:2000217`.

[45] D. Massa, A. W. Fullerton, and R. K. Prinja. "Rotational modulation of B supergiants winds". In: *Cyclical Variability in Stellar Winds*. Ed. by L. Kaper and A. W. Fullerton. Springer-Verlag, 1998, p. 415.

[46] P. Massey. *A user's guide to CCD reductions with IRAF*. 1997. URL: `http://iraf.noao.edu`.

[47] P. Massey, F. Valdes, and Barnes J. *A user's guide to reducing slit spectra with IRAF*. 1992. URL: `http://iraf.noao.edu`.

[48] P. J. McGregor, A. R. Hyland, and D. J. Hillier. "Atomic and molecular line emission from early-type high-luminosity stars". In: *ApJ* 324 (Jan. 1988), pp. 1071–1098. DOI: `10.1086/165964`.

[49] Y. J. L. Michaux et al. "On the origin of variable structures in the winds of hot luminous stars". In: *MNRAS* 440 (May 2014), pp. 2–9. DOI: `10.1093/mnras/stt2102`. arXiv: `1312.2864 [astro-ph.SR]`.

[50] A. S. Miroshnichenko. "Galactic B[e] Stars: A Review of 30 Years of Investigation". In: *Stars with the B[e] Phenomenon*. Ed. by M. Kraus and A. S. Miroshnichenko. Vol. 355. Astronomical Society of the Pacific Conference Series. Dec. 2006, p. 13.

[51] A. S. Miroshnichenko. "Toward Understanding the B[e] Phenomenon. I. Definition of the Galactic FS CMa Stars". In: *ApJ* 667 (Sept. 2007), pp. 497–504. DOI: `10.1086/520798`.

[52] A. S. Miroshnichenko et al. "Toward Understanding the B[e] Phenomenon. II. New Galactic FS CMa Stars". In: *ApJ* 671 (Dec. 2007), pp. 828–841. DOI: `10.1086/523094`.

[53] A. S. Miroshnichenko et al. "Toward Understanding the B[e] Phenomenon. III. Properties of the Optical Counterpart of IRAS 00470+6429". In: *ApJ* 700 (July 2009), pp. 209–220. DOI: `10.1088/0004-637X/700/1/209`. arXiv: `0906.0722 [astro-ph.SR]`.

[54] A. S. Miroshnichenko et al. "Toward Understanding the B[e] Phenomenon: V. Nature and Spectral Variations of the MWC 728 Binary System." In: *ApJ* 809, 129 (Aug. 2015), p. 129. DOI: `10.1088/0004-637X/809/2/129`. arXiv: `1508.00950 [astro-ph.SR]`.

[55] C. E. Moore. "A Multiplet Table of Astrophysical Interest. Revised Edition. Part I - Table of Multiplets". In: *Contributions from the Princeton University Observatory* 20 (1945), pp. 1–110.

[56] C. E. Moore and P. W. Merrill. *Partial Grotrian diagrams of astrophysical interest*. 1968.

[57] A. T. Okazaki. "On the confinement of one-armed oscillations in discs of Be stars." In: *A&A* 318 (Feb. 1997), pp. 548–560.

[58] A. T. Okazaki. "Theory of Global Disk Oscillations". In: *IAU Colloq. 175: The Be Phenomenon in Early-Type Stars*. Ed. by M. A. Smith, H. F. Henrichs, and J. Fabregat. Vol. 214. Astronomical Society of the Pacific Conference Series. 2000, p. 409.

[59] A. T. Okazaki and S. Kato. "One-armed adiabatic oscillations of a nonself-gravitating polytropic disk. I - A disk with constant thickness". In: *PASJ* 37 (1985), pp. 683–696.

[60] D. E. Osterbrock and G. J. Ferland. *Astrophysics of gaseous nebulae and active galactic nuclei*. 2006.

[61] S. P. Owocki. "Modelling variability in Hot star winds". In: *Cyclical Variability in Stellar Winds*. Ed. by L. Kaper and A. W. Fullerton. Springer-Verlag, 1998, p. 415.

[62] G. J. Peters. "Cyclic variability in Be star winds: the observations". In: *Cyclical Variability in Stellar Winds*. Ed. by L. Kaper and A. W. Fullerton. Springer-Verlag, 1998, p. 415.

[63] M. Pogodin. "Wind variability in PMS stars". In: *Cyclical Variability in Stellar Winds*. Ed. by L. Kaper and A. W. Fullerton. Springer-Verlag, 1998, p. 415.

[64] J. Polster et al. "Time-dependent spectral-feature variations of stars displaying the B[e] phenomenon. I. V2028 Cygni". In: *A&A* 542, A57 (June 2012), A57. DOI: `10.1051/0004-6361/201117210`. arXiv: `1208.4003 [astro-ph.SR]`.

[65] R. K. Prinja. "Systematic variability in OB star winds". In: *Cyclical Variability in Stellar Winds*. Ed. by L. Kaper and A. W. Fullerton. Springer-Verlag, 1998, p. 415.

[66] W. Pych. "A Fast Algorithm for Cosmic-Ray Removal from Single Images". In: *PASP* 116 (Feb. 2004), pp. 148–153. DOI: `10.1086/381786`. eprint: `astro-ph/0311290`.

[67] A. H. N. Reid et al. "Time-Series Observations of O Stars. II. Optical Observations of zeta Ophiuchi". In: *ApJ* 417 (Nov. 1993), p. 320. DOI: `10.1086/173315`.

[68] B. Reipurth, A. Pedrosa, and M. T. V. T. Lago. "Hα emission in pre-main sequence stars. I. an atlas of line profiles." In: *A&AS* 120 (Dec. 1996), pp. 229–256.

[69] T. Rivinius, A. C. Carciofi, and C. Martayan. "Classical Be stars. Rapidly rotating B stars with viscous Keplerian decretion disks". In: *A&ARv* 21, 69 (Oct. 2013), p. 69. DOI: 10.1007/s00159-013-0069-0. arXiv: 1310.3962 [astro-ph.SR].

[70] M. Salaris and S. Cassisi. *Evolution of Stars and Stellar Populations*. Wiley-VCH, 2005, p. 400.

[71] G. J. Savonije. "Long-term cyclic V/R variations in Be stars". In: *Cyclical Variability in Stellar Winds*. Ed. by L. Kaper and A. W. Fullerton. Springer-Verlag, 1998, p. 415.

[72] S. N. Shore. *The Tapestry of Modern Astrophysics*. Wiley-Interscience, 2002, p. 888.

[73] S. N. Shore and G. M. Wahlgren. "The O I] 1641 Å line as a probe of symbiotic star winds". In: *A&A* 515, A108 (June 2010), A108. DOI: 10.1051/0004-6361/201014271. arXiv: 1004.2532 [astro-ph.SR].

[74] S. N. Shore et al. "Goddard high-resolution spectrograph observations of narrow discrete stellar wind absorption features in the ultraviolet spectrum of the O7.5 III star XI Persei". In: *ApJ* 411 (July 1993), pp. 864–868. DOI: 10.1086/172889.

[75] J. Silaj et al. "Investigating the Circumstellar Disk of the Be Shell Star 48 Librae". In: *ApJ* 826, 81 (July 2016), p. 81. DOI: 10.3847/0004-637X/826/1/81. arXiv: 1608.00943 [astro-ph.SR].

[76] P. Skoda and M. Slechta. "Reduction of spectra exposed by the 700mm CCD camera of the Ondřejov telescope coudé spectrograph". In: *Publications of the Astronomical Institute of the Czechoslovak Academy of Sciences* 90 (2002), pp. 22–35.

[77] M. Slechta and P. Skoda. "2-meter telescope devices: coudé slit spectrograph and HEROS". In: *Publications of the Astronomical Institute of the Czechoslovak Academy of Sciences* 90 (2002), pp. 1–4.

[78] O. Stahl et al. "Long-term spectroscopic monitoring of P Cygni-type stars. II. Spectroscopic variations of P Cygni during 1990-1992." In: *A&AS* 107 (Oct. 1994).

[79] S. Stefl. "Disks of classical Be stars". In: *Variable and Non-spherical Stellar Winds in Luminous Hot Stars*. Ed. by B. Wolf, O. Stahl, and A. W. Fullerton. Vol. 169. IAU Coll. 1999.

[80] J. Telting and C. Schrijvers. "Line-profile variability as a diagnostic for non-radial pulsation mode identification". In: *Cyclical Variability in Stellar Winds*. Ed. by L. Kaper and A. W. Fullerton. Springer-Verlag, 1998, p. 415.

[81] G. B. Thompson and N. D. Morrison. "Variability in Optical Spectra of epsilon Orionis". In: *AJ* 145, 95 (Apr. 2013), p. 95. DOI: 10.1088/0004-6256/145/4/95. arXiv: 1301.5368 [astro-ph.SR].

[82] R. Townsend. "The Coupling Between Pulsation and Mass Loss in Massive Stars". In: *Unsolved Problems in Stellar Physics: A Conference in Honor of Douglas Gough*. Ed. by R. J. Stancliffe et al. Vol. 948. American Institute of Physics Conference Series. Nov. 2007, pp. 345–356. DOI: 10.1063/1.2818992. arXiv: 0709.0761.

[83] R. G. Tull et al. "The high-resolution cross-dispersed echelle white-pupil spectrometer of the McDonald Observatory 2.7-m telescope". In: *PASP* 107 (Mar. 1995), pp. 251–264. DOI: 10.1086/133548.

[84] F. Valdes. *Guide to the slit spectra reduction task DOECSLIT*. 1993. URL: http://iraf.noao.edu.

[85] R. H. van Gent and H. J. G. L. M. Lamers. "Periodicity of the radial-velocity and brightness variations of the hypergiant P Cygni (B1 Ia+), and origin of the shell ejections". In: *A&A* 158 (Apr. 1986), pp. 335–350.

[86] K. Vollmann and T. Eversberg. "Remarks on statistical errors in equivalent widths". In: *Astronomische Nachrichten* 327 (Nov. 2006), p. 862. DOI: 10.1002/asna.200610645. eprint: astro-ph/0606341.

[87] D. Willmarth and Barnes J. *A user's guide to reducing echelle spectra with IRAF*. 1994. URL: http://iraf.noao.edu.

[88] F. Zickgraf. "The Connection with B[e] stars". In: *IAU Colloq. 175: The Be Phenomenon in Early-Type Stars*. Ed. by M. A. Smith, H. F. Henrichs, and J. Fabregat. Vol. 214. Astronomical Society of the Pacific Conference Series. 2000, p. 26. eprint: astro-ph/9912093.

Appendix A

Journal of observations

Table A.1 shows the journal of observation of the object IRAS 17449 + 2320. It reports the date of observation, the reduced Heliocentric Julian Date ($\mathrm{HJD}_{red} = \mathrm{HJD} - 2450000$), the observatory, the type of the spectrograph with its resolution and wavelength range and the exposure time of the observation. In the case of CFHT spectra, the exposure time is not available (N.A.) because the FITS header was not write in a proper manner.

Date (year/month/day)	HJD_{red}	Observatory	Spectrograph	$R = \lambda/\Delta\lambda$	wavelength range (Å)	$t_{exp}(s)$
2006/06/09	3895.600	CFHT	Échelle	80000	[3700,10500]	N.A.
2007/07/02	4284.60	CFHT	Échelle	80000	[3700,10500]	N.A.
2008/04/28	4585.47	Ondřejov	Grating	13000	[6250,6750]	3600
2008/05/16	4603.44	Ondřejov	Grating	13000	[6250,6750]	4200
2008/07/24	4671.60	CFHT	Échelle	80000	[3700,10500]	N.A.
2009/04/18	4940.44	Ondřejov	Grating	13000	[6250,6750]	5400
2009/09/05	5080.63	McDonald	Échelle	60000	[3400,10000]	900
2011/02/24	5616.65	Ondřejov	Grating	13000	[6250,6750]	4000
2011/02/26	5618.56	Ondřejov	Grating	13000	[6250,6750]	3695
2011/03/22	5642.61	Ondřejov	Grating	13000	[6250,6750]	4200
2011/04/10	5662.52	Ondřejov	Grating	13000	[6250,6750]	5035
2011/04/20	5671.55	Ondřejov	Grating	13000	[6250,6750]	3630
2011/04/22	5674.44	Ondřejov	Grating	13000	[6250,6750]	3001
2011/05/07	5688.59	Ondřejov	Grating	13000	[6250,6750]	3206
2011/09/03	5808.44	Ondřejov	Grating	13000	[6250,6750]	3600
2011/10/04	5839.36	Ondřejov	Grating	13000	[6250,6750]	3650
2011/11/11	5877.22	Ondřejov	Grating	13000	[6250,6750]	3600
2012/03/05	5991.60	Ondřejov	Grating	13000	[6250,6750]	3600
2012/03/25	6011.61	Ondřejov	Grating	13000	[6250,6750]	3600
2012/03/26	6012.54	Ondřejov	Grating	13000	[6250,6750]	3600
2012/07/23	6132.39	Ondřejov	Grating	13000	[6250,6750]	5400
2012/07/26	6135.40	Ondřejov	Grating	13000	[6250,6750]	3000
2012/08/14	6154.35	Ondřejov	Grating	13000	[6250,6750]	3600
2012/08/18	6158.36	Ondřejov	Grating	13000	[6250,6750]	4500
2012/09/16	6187.34	Ondřejov	Grating	13000	[6250,6750]	3600
2012/09/21	6192.30	Ondřejov	Grating	13000	[6250,6750]	4800
2012/10/08	6209.27	Ondřejov	Grating	13000	[6250,6750]	2400
2012/10/11	6212.33	Ondřejov	Grating	13000	[6250,6750]	5320
2013/04/17	6400.49	Ondřejov	Grating	13000	[6250,6750]	3838
2013/04/23	6406.46	Ondřejov	Grating	13000	[6250,6750]	5400
2013/05/08	6421.40	Ondřejov	Grating	13000	[6250,6750]	3600
2013/05/15	6428.42	Ondřejov	Grating	13000	[6250,6750]	3000
2013/06/13	6457.45	Ondřejov	Grating	13000	[6250,6750]	4201
2013/07/15	6489.42	Ondřejov	Grating	13000	[6250,6750]	4201
2013/08/16	6521.41	Ondřejov	Grating	13000	[6250,6750]	3601
2013/10/06	6572.31	Ondřejov	Grating	13000	[6250,6750]	5401
2013/10/26	6592.24	Ondřejov	Grating	13000	[6250,6750]	3601
2014/02/24	6712.57	Ondřejov	Grating	13000	[6250,6750]	5001
2014/03/02	6718.63	Ondřejov	Grating	13000	[6250,6750]	7607

2014/04/26	6774.42	Ondřejov	Grating	13000	[6250,6750]	4601
2014/05/31	6809.51	Ondřejov	Grating	13000	[6250,6750]	6148
2014/06/08	6817.47	Ondřejov	Grating	13000	[6250,6750]	2033
2014/07/15	6854.40	Ondřejov	Grating	13000	[6250,6750]	3355
2014/07/17	6856.41	Ondřejov	Grating	13000	[6250,6750]	3601
2014/07/22	6861.44	Ondřejov	Grating	13000	[6250,6750]	5051
2014/08/08	6878.36	Ondřejov	Grating	13000	[6250,6750]	4201
2014/08/30	6900.36	Ondřejov	Grating	13000	[6250,6750]	4201
2014/10/19	6950.23	Ondřejov	Grating	13000	[6250,6750]	4201
2015/05/29	7172.76	SPM	Échelle	18000	[3500,7300]	1200
2015/05/30	7173.75	SPM	Échelle	18000	[3500,7300]	1200
2015/05/31	7174.74	SPM	Échelle	18000	[3500,7300]	1200
2015/06/01	7175.73	SPM	Échelle	18000	[3500,7300]	1200
2015/06/02	7176.75	SPM	Échelle	18000	[3500,7300]	1200
2015/06/03	7177.73	SPM	Échelle	18000	[3500,7300]	1200

Table A.1: Journal of observation.

Appendix B

Matlab and Python scripts

B.1 specnorm.py

The python routine called specnorm.py has been used for the normalization of the echelle spectra.

```python
import pylab as plt
import numpy as np
from scipy.interpolate import splrep,splev
import sys
import os

def onclick(event):
    # when none of the toolbar buttons is activated and the user clicks in the
    # plot somewhere, compute the median value of the spectrum in a 10angstrom
    # window around the x-coordinate of the clicked point. The y coordinate
    # of the clicked point is not important. Make sure the continuum points
    # 'feel' it when it gets clicked, set the 'feel-radius' (picker) to 5 points
    toolbar = plt.get_current_fig_manager().toolbar
    if event.button==1 and toolbar.mode=='':
        window = ((event.xdata-0.1)<=wave) & (wave<=(event.xdata+0.1))
        y = np.median(flux[window])
        plt.plot(event.xdata,y,'rs',ms=10,picker=5,label='cont_pnt')
    plt.draw()

def onpick(event):
    # when the user clicks right on a continuum point, remove it
    if event.mouseevent.button==3:
        if hasattr(event.artist,'get_label') and event.artist.get_label()=='cont_pnt':
            event.artist.remove()

def ontype(event):
    # when the user hits enter:
    # 1. Cycle through the artists in the current axes. If it is a continuum
    #    point, remember its coordinates. If it is the fitted continuum from the
    #    previous step, remove it
    # 2. sort the continuum-point-array according to the x-values
    # 3. fit a spline and evaluate it in the wavelength points
    # 4. plot the continuum
    if event.key=='enter':
        cont_pnt_coord = []
        for artist in plt.gca().get_children():
            if hasattr(artist,'get_label') and artist.get_label()=='cont_pnt':
                cont_pnt_coord.append(artist.get_data())
            elif hasattr(artist,'get_label') and artist.get_label()=='continuum':
                artist.remove()
        cont_pnt_coord = np.array(cont_pnt_coord)[...,0]
        sort_array = np.argsort(cont_pnt_coord[:,0])
```

```python
        x,y = cont_pnt_coord[sort_array].T
        spline = splrep(x,y,k=3)
        continuum = splev(wave,spline)
        plt.plot(wave,continuum,'r-',lw=2,label='continuum')

    # when the user hits 'n' and a spline-continuum is fitted, normalise the
    # spectrum
    elif event.key=='n':
        continuum = None
        for artist in plt.gca().get_children():
            if hasattr(artist,'get_label') and artist.get_label()=='continuum':
                continuum = artist.get_data()[1]
                break
        if continuum is not None:
            plt.cla()
            plt.plot(wave,flux/continuum,'k-',label='normalised')

    # when the user hits 'r': clear the axes and plot the original spectrum
    elif event.key=='r':
        plt.cla()
        plt.plot(wave,flux,'k-')

    # when the user hits 'w': if the normalised spectrum exists, write it to a
    # file.
    elif event.key=='w':
        for artist in plt.gca().get_children():
            if hasattr(artist,'get_label') and artist.get_label()=='normalised':
                data = np.array(artist.get_data())
                np.savetxt(os.path.splitext(filename)[0]+'_n.dat',data.T)
                print('Saved to file')
                break
    plt.draw()


if __name__ == "__main__":
    # Get the filename of the spectrum from the command line, and plot it
    filename = sys.argv[1]
    wave,flux = np.loadtxt(filename).T
    spectrum, = plt.plot(wave,flux,'k-',label='spectrum')
    plt.title(filename)

    # Connect the different functions to the different events
    plt.gcf().canvas.mpl_connect('key_press_event',ontype)
    plt.gcf().canvas.mpl_connect('button_press_event',onclick)
    plt.gcf().canvas.mpl_connect('pick_event',onpick)
    plt.show() # show the window
```

B.2   lambda_EW_RV.m

The Matlab script called lambda_EW_RV.m has been used for the calculation of the radial velocity and the equivalent width of lines.

```
%First: Imports the data of a spectrum (wavelength w and flux f)
%Second: Calculates the Signal to Noise ratio
%Third: Calculates the Equivalent Width and the Radial Velocity of a line
%Fourth: Saves the results in a file
%Fifth: Iterates the third and the fourth passes for another line if you press 1
clear
%import data from one order-------------------------------------------
data=importdata('filename');
w=data(:,1);    %wavelength
f=data(:,2);     %flux
a=size(w);

plot(w,f)

%calculate the mean and the standard deviation for the Signal To Noise Ratio sn

%take from input the boundaries of the range where it calculates the sn----------------
left_snr=input('insert left boundary for the SNR ');
right_snr=input('insert right boundary for the SNR ');

%find the right-nearest point of the data for the boundaries and their
%indexes (ind_snr_l, ind_snr_r)-------------------------------------------------
for i=1:a-1

    if (w(i)<left_snr)&&(w(i+1)>left_snr)
        w_snr_l=w(i+1);
        ind_snr_l=i+1;
    end

    if(w(i)<right_snr)&&(w(i+1)>right_snr)
        w_snr_r=w(i+1);
        ind_snr_r=i+1;
    end

end

%The standard deviation from the mean is used as the error on the fluxes
mu=mean(f(ind_snr_l:ind_snr_r));
dmu=std(f(ind_snr_l:ind_snr_r));
sn=mu/dmu;
df=dmu;
dw=(w(5)-w(4))/2;


h=1;
while h==1

    %take from input the boundaries for the integration----------------------
    left=input('insert left boundary ');
    right=input('insert right boundary ');
    %find the right-nearest point of the data for the boundaries and their
    %indexes (indl, indr)-------------------------------------------------
    for i=1:a-1

        if (w(i)<left)&&(w(i+1)>left)
            wl=w(i+1);
```

```matlab
            indl=i+1;
        end

        if(w(i)<right)&&(w(i+1)>right)
            wr=w(i+1);
            indr=i+1;
        end

    end

    %calculate the mean lambda of the line (w_mean)
    %and the equivalent width (EW)---------------------------------------
    for j=indl:indr-1

        up_p(j)= (f(j+1)*w(j+1)+f(j)*w(j))*(w(j+1)-w(j))/2;
        down_p(j)=(f(j+1)+f(j))*(w(j+1)-w(j))/2;

        ew_partial(j)=(2-f(j+1)/mu-f(j)/mu)*(w(j+1)-w(j))/2;
        dB=dw*sqrt(2);
        dC(j)=df/mu*sqrt(2+((f(j+1)+f(j))/mu)^2);
        dew_partial(j)=0.5*(((w(j+1)-w(j))*dC(j))^2 + ((2-f(j+1)-f(j))*dB)^2)^0.5;
    end

    up=sum(up_p(indl:indr-1));
    down=sum(down_p(indl:indr-1));
    w_mean=up/down;

    EW=sum(ew_partial(indl:indr-1));
    dEW=(sum(dew_partial(indl:indr-1).^2))^0.5;
    %ask for the wavelength at rest (lambda_0) and calculate the radial
    %velocity(RV)----------------------------------------------------------
    c=299792.458;
    lambda_0=input('insert lambda at rest ');
    RV=(w_mean-lambda_0)*c/lambda_0;
    diff=w_mean-lambda_0;
    dRV=dw*c/lambda_0;

    %write lambda_0, w_mean, EW and RV into a file-------------------------------------
    lan=round(lambda_0);
    filename=strcat('w0_w_EW_RV_',int2str(lan));
    fid=fopen(filename,'w');
    line_data=[lambda_0,w_mean,dw,EW,dEW,RV,dRV,sn];
    fprintf(fid,'%f %f %f %f %f %f %f %f\n',line_data);
    fclose(fid);
    h=input('if you want to analyze another line press 1 ');
end
```

B.3   EW_RV_F.py

The python routine called EW_RV_F.py has been used for the calculation of the equivalent width, radial velocity and flux for Hα, [O I] λλ 6300, 6364.

```
#===============================================================================
# EW, RV and F for lines Halpha, [O I] 6300, [O I] 6364
# basic: fit Gaussian function, polynomials - 2 and 5 grade
#redraw using p
#finding min and  max of polynomial using min and max of chosen field
#new--------------------------------------------------------------------------
#MC errors of RV and rel. fluxes
#===============================================================================
from scipy import optimize
from pylab import *
import os,sys,string
from turtle import RawPen
import codecs
from functools import partial
from scipy.optimize import leastsq
from scipy.optimize import fsolve
import numpy as np
import matplotlib.pyplot as plt
from scipy.optimize import curve_fit
import math
import pylab
import scipy.optimize as optimization
from Tkinter import  * # Tk, Canvas, Button, Label
import math
#=======================================================
#turn off matplotlib shortcuts (may be edit globaly in matplotlib
#source file)
#keymap.pan : p                         # pan mnemonic
#keymap.zoom : o                        # zoom mnemonic
#keymap.save : s                        # saving current figure
#keymap.quit : q                        # close the current figure
#keymap.grid : g                        # switching on/off a grid in current axes
#keymap.yscale : l                      # toggle scaling of y-axes ('log'/'linear')
#keymap.xscale : L, k                   # toggle scaling of x-axes ('log'/'linear')
plt.rcParams['keymap.pan'] = ''
plt.rcParams['keymap.zoom'] = ''
plt.rcParams['keymap.save'] = ''
plt.rcParams['keymap.grid'] = ''
plt.rcParams['keymap.home'] = ''
plt.rcParams['keymap.yscale']=''
plt.rcParams['keymap.xscale']=''
#print rcParams.keys()
#=======================================================
class Parameter:
    def __init__(self, value):
            self.value = value

    def set(self, value):
            self.value = value

    def __call__(self):
            return self.value
tmx=[]
tmy=[]
nmax=5
#=======================================================
```

```
def click(btn):
# test the button command click
    global koren_vyb
    koren_vyb=btn
#=======================================================
def vyberkorenu(maxkor):
    korenu=len(maxkor)
    root = Tk()
    canvas = Canvas(root,width=30,height=10*korenu)
    canvas.pack()
    lf = LabelFrame(root, bd=1)
    lf.pack(padx=1, pady=korenu)
    L_popis = Label(root, width=30,
  text="vyber koren",
  font = ("Courier",14,"bold") )
    L_popis.pack()
    btn = list(range(len(maxkor)))
    n=0
    c=0
    for label in maxkor:
# partial takes care of function and argument
cmd = partial(click, label)
# create the button
btn[n] = Button(lf, text=label, width=30, command=cmd)
# position the button
btn[n].grid(row=n, column=c)
# increment button index
n += 1
# update row/column position
#c += 1
    raw_input("Press ENTER to exit")
#=============================================================
def pkey(event):
        global maxkor,xmeze,sn,chyba_rv_a, chyba_rv_b,chyba_ew_a,
        chyba_ew_b,ew_a, ew_b, rv_a, rv_b, ymax_a, ymax_b,xmax_a,
         xmax_b, chybah_a, chybah_b, lam_l, er_lam_l, f_l, er_f_l, lam_m, er_lam_m,
         f_m, er_f_m, lam_r,er_lam_r , f_r, er_f_r, koren_vyb, hod_koren_vyb,
         hod_koren_chyba, koren_chyba, lam_s1, er_lam_s1, f_s1, er_f_s1,
         lam_s2, er_lam_s2, f_s2, er_f_s2, lam_h, er_lam_h, f_h, er_f_h
        if (event.key=='p'):
          # provede vymaz
          print "Drawing spectra"
          clf()
          plot(x1,y1,'r-')
          plot(x1,y1,'b+')
          xmeze=[np.min(x),np.max(x)]
          draw()
        elif (event.key=='n'):
            print "Computin S/N"
            # podvyber dat
            tmsk=np.ma.masked_inside(x,np.min(xmeze),np.max(xmeze))
            pocn=len(x)-np.ma.count(tmsk)
            tmx=np.zeros([pocn],float)
            tmy=np.zeros([pocn],float)
            cnt=0
            for j in range(len(x)):
                if (tmsk.mask[j]==True):
                    tmx[cnt]=x[j]
                    tmy[cnt]=y[j]
                    cnt+=1
            p=[0,1]
```

```
        nhodnot = len(tmy)
        [a,b], covar = curve_fit(lin,tmx,tmy,p)
        #S/N (mean variance points from fit fuction - from definition (IRAF))
        sn=(nhodnot/sum((lin(tmx,a,b)-tmy)**2))**(0.5)
        print sn
        plot(tmx,lin(tmx,a,b),'-')
        draw()
#-------------------------------------------------------------------------------
#[O I] 6300.304 #===============================================================
#-------------------------------------------------------------------------------
    elif (event.key=='a'):
        tmsk=np.ma.masked_inside(x,np.min(xmeze),np.max(xmeze))
        pocn=len(x)-np.ma.count(tmsk)
        tmx=np.zeros([pocn],float)
        tmy=np.zeros([pocn],float)
        nhodnot=len(tmy)
        cnt=0
        for j in range(len(x)):
            if (tmsk.mask[j]==True):
                tmx[cnt]=x[j]
                tmy[cnt]=y[j]
                cnt+=1
        orezx = []
        orezy = []
        p0 = [len(tmy),tmx[int(len(tmx)/2.0)],len(tmx)/2.0,1]
        j=-1
        for jj in range(30):
            orezx.append(tmx[len(tmx)/2]-(1000+jj)*abs(p0[2]))
            orezy.append(1.0)
        for jj in tmx:
            j=j+1
            orezx.append(tmx[j])
            orezy.append(tmy[j])
        for jj in range(30):
            orezx.append(tmx[len(tmx)/2]+(1000+jj)*abs(p0[2]))
            orezy.append(1.0)
        [height,mu,sigma,const], covar = curve_fit(f, orezx, orezy,p0)
        obl=arange(tmx[len(tmx)/2]-(15+100)*abs(sigma),tmx[len(tmx)/2]+
        (15+100)*abs(sigma),0.01)
        plot(obl,f(obl,height,mu,sigma,const),'-',c='blue')
        plot(orezx,orezy,'+')
#RV#---------------------------------------------------------------   -------
        rv_a = (mu-6300.304)*299792.458/6300.304
        v,w = linalg.eig(covar)
        par_mu=np.zeros([100],float)
        par_y = np.zeros([100],float)
        for j in range(100):
            noise=np.random.normal(loc=0,scale=1.0/(2.355*sn),size=len(orezy))
            tmy_noise=orezy+noise
            [height,mu,sigma,const], covar = curve_fit(f, orezx, tmy_noise,p0)
            par_mu[j]=mu
            par_y[j]=f(mu,height,mu,sigma,const)
        chybafit = ((covar[1,1]+(max(par_mu)-min(par_mu))**2)**(0.5))*299792.458/6300.304
        chyba_rv_a=chybafit
        xmax_a=mu
        print rv_a, chyba_rv_a
#intensity#---------------------------------------------------------------
        ymax_a=height+1
        chybah_a = sqrt(covar[0,0]+(max(par_y)-min(par_y))**2)
        print ymax_a, chybah_a
#EW#---------------------------------------------------------------------------
```

```
            ew_a = height*sigma*(pi)**(0.5)
            F = sum(tmy)/len(tmy)
            dellam = tmx[len(tmx)-1]-tmx[0]
            chyba_ew_a = (1+1/F)**(0.5)*((dellam-ew_a)/(sn))
            print ew_a, chyba_ew_a
            pylab.axvline(xmax_a, c='blue', label='extrem')
            pylab.axvline(xmax_a+chybafit*6300.304/299792.458, c='blue', label='extrem')
            pylab.axvline(xmax_a-chybafit*6300.304/299792.458, c='blue', label='extrem')
            p = plt.axvspan(xmax_a-chybafit*6300.304/299792.458,
            xmax_a+chybafit*6300.304/299792.458,facecolor='blue',alpha=0.5)
            draw()


#--------------------------------------------------------------------------------
#[O I] 6363.776 #================================================================
#--------------------------------------------------------------------------------
        elif (event.key=='b'):
            tmsk=np.ma.masked_inside(x,np.min(xmeze),np.max(xmeze))
            pocn=len(x)-np.ma.count(tmsk)
            tmx=np.zeros([pocn],float)
            tmy=np.zeros([pocn],float)
            nhodnot=len(tmy)
            cnt=0
            for j in range(len(x)):
                if (tmsk.mask[j]==True):
                    tmx[cnt]=x[j]
                    tmy[cnt]=y[j]
                    cnt+=1
            orezx = []
            orezy = []
            p0 = [len(tmy),tmx[int(len(tmx)/2.0)],len(tmx)/2.0,1]
            j=-1
            for jj in range(30):
                orezx.append(tmx[len(tmx)/2]-(1000+jj)*abs(p0[2]))
                orezy.append(1.0)
            for jj in tmx:
                j=j+1
                orezx.append(tmx[j])
                orezy.append(tmy[j])
            for jj in range(30):
                orezx.append(tmx[len(tmx)/2]+(1000+jj)*abs(p0[2]))
                orezy.append(1.0)
            [height,mu,sigma,const], covar = curve_fit(f, orezx, orezy,p0)
            obl=arange(tmx[len(tmx)/2]-(15+100)*abs(sigma),tmx[len(tmx)/2]+(15+100)*abs(sigma),0.01)
            plot(obl,f(obl,height,mu,sigma,const),'-',c='red')
            plot(orezx,orezy,'+')
#RV#--------------------------------------------------------------------------
            rv_b = (mu-6363.776)*299792.458/6363.776
            v,w = linalg.eig(covar)
            par_mu=np.zeros([100],float)
            par_y = np.zeros([100],float)
            for j in range(100):
                noise=np.random.normal(loc=0,scale=1.0/(2.355*sn),size=len(orezy))
                tmy_noise=orezy+noise
                [height,mu,sigma,const], covar = curve_fit(f, orezx, tmy_noise,p0)
                par_mu[j]=mu
                par_y[j]=f(mu,height,mu,sigma,const)
            chybafit = ((covar[1,1]+(max(par_mu)-min(par_mu))**2)**(0.5))*299792.458/6363.776
            chyba_rv_b=chybafit
            xmax_b=mu
            print rv_b, chyba_rv_b
#intensity#-------------------------------------------------------------------
```

```
        ymax_b=height+1
        chybah_b = sqrt(covar[0,0]+(max(par_y)-min(par_y))**2)
        print ymax_b, chybah_b
#EW#------------------------------------------------------------------------------
        ew_b = height*sigma*(pi)**(0.5)
        F = sum(tmy)/len(tmy)
        dellam = tmx[len(tmx)-1]-tmx[0]
        chyba_ew_b = (1+1/F)**(0.5)*((dellam-ew_b)/(sn))
        print ew_b, chyba_ew_b
        pylab.axvline(xmax_b, c='red', label='extrem')
        pylab.axvline(xmax_b+chybafit*6363.776/299792.458, c='red', label='extrem')
        pylab.axvline(xmax_b-chybafit*6363.776/299792.458, c='red', label='extrem')
        p = plt.axvspan(xmax_b-chybafit*6363.776/299792.458,
        xmax_b+chybafit*6363.776/299792.458,facecolor='red',alpha=0.5)
        draw()
#------------------------------------------------------------------------------
#Halpha   #=====================================================================
#------------------------------------------------------------------------------
      elif (event.key=='h'):
        tmsk=np.ma.masked_inside(x,np.min(xmeze),np.max(xmeze))
        pocn=len(x)-np.ma.count(tmsk)
        tmx=np.zeros([pocn],float)
        tmy=np.zeros([pocn],float)
        nhodnot=len(tmy)
        cnt=0
        for j in range(len(x)):
            if (tmsk.mask[j]==True):
                tmx[cnt]=x[j]
                tmy[cnt]=y[j]
                cnt+=1
#------------------------------------------------------------------------------
        nmax=5
        p=np.polyfit(tmx,tmy,nmax) #first parameter estimation by polyfit
        koef=[]
        koef=p
        ft=np.poly1d(p)
#        ftdat=ft(tmx)
        mups=tmx[int(len(tmx)/2.0)] #extreme position guess
        if (tmy[0] < tmy[int(len(tmx)/2.0)]):
            for index, item in enumerate(tmy):
                    if (item == max(tmy)):
                        mup=tmx[index]
        if (tmy[0] > tmy[int(len(tmx)/2.0)]):
            for index, item in enumerate(tmy):
                    if (item == min(tmy)):
                        mup=tmx[index]
        #parameter guess prepared for curve_fit
        ap=5*koef[0]
        bp=4*koef[1]+mup*ap
        cp=3*koef[2]+mup*bp
        dp=2*koef[3]+mup*cp
        ep=koef[5]
        polpar = [mup,ap,bp,cp,dp,ep]
        [mu,a,b,c,d,e], covar = curve_fit(p5, tmx, tmy,polpar) #curve fit
        hod_koren_vyb=p5(mu,mu,a,b,c,d,e)
        hodnoty_fit=p5(tmx,mu,a,b,c,d,e)
        nhodnot=len(tmy)
        koren_chyba1=covar[0,0]**(0.5)
        koren_vyb = mu
        print covar
        #terka-carlo
```

```
        #----------------------------------------------------------------
        par_mu=np.zeros([100],float)
        par_y = np.zeros([100],float)
        for j in range(100):
            noise=np.random.normal(loc=0,scale=1.0/(2.355*sn),size=len(tmy))
            tmy_noise=tmy+noise
            [mu,a,b,c,d,e], covar = curve_fit(p5, tmx, tmy_noise,polpar)
            par_mu[j]=mu
            par_y[j]=p5(mu,mu,a,b,c,d,e)
        print koren_vyb, min(par_mu), max(par_mu)
        koren_chyba=(koren_chyba1**2+(max(par_mu)-min(par_mu))**2)**(0.5)
        #----------------------------------------------------------------
        cnt=0
        print '################################################'
        print 'extreme position:', koren_vyb, 'error:',
         koren_chyba, 'error_FIT:', koren_chyba1
        print '################################################'
        #the third round of fitting - see manual
        plot(tmx,p5(tmx,mu,a,b,c,d,e),'p-')
        mu = 0 #
        [mu,a,b,c,d,e], covar = curve_fit(p5, tmx-koren_vyb, tmy)
        hod_koren_chyba=sqrt(covar[5,5]+(max(par_y)-min(par_y))**2)
        hod_chyba1=covar[5,5]**(0.5)
        print '################################################'
        print 'extr. position value:', hod_koren_vyb, 'error:',
        hod_koren_chyba, 'error_FIT', hod_chyba1
        print '################################################'
        print covar
        pylab.axvline(koren_vyb, c='red', label='extrem')
        pylab.axvline(koren_vyb+koren_chyba, c='red', label='extrem')
        pylab.axvline(koren_vyb-koren_chyba, c='red', label='extrem')
        p = plt.axvspan(koren_vyb-koren_chyba,
        koren_vyb+koren_chyba, facecolor='red', alpha=0.5)
        draw()
        print 'write l,m, or r for Halpha, c,v for Si II and e for He I'
    elif (event.key=='g'):
        tmsk=np.ma.masked_inside(x,np.min(xmeze),np.max(xmeze))
        pocn=len(x)-np.ma.count(tmsk)
        tmx=np.zeros([pocn],float)
        tmy=np.zeros([pocn],float)
        nhodnot=len(tmy)
        cnt=0
        for j in range(len(x)):
            if (tmsk.mask[j]==True):
                tmx[cnt]=x[j]
                tmy[cnt]=y[j]
                cnt+=1
#-------------------------------------------------------------------------------
        nmax=3
        p=np.polyfit(tmx,tmy,nmax)
        koef=[]
        koef=p
        print koef
        ft=np.poly1d(p)
        ftdat=ft(tmx)
        #plot(tmx,ftdat,'b--')
        mups=tmx[int(len(tmx)/2.0)] #extreme position guess
        if (tmy[0] < tmy[int(len(tmx)/2.0)]):
            for index, item in enumerate(tmy):
                    if (item == max(tmy)):
                        mup=tmx[index]
```

```
        if (tmy[0] > tmy[int(len(tmx)/2.0)]):
            for index, item in enumerate(tmy):
                        mup=tmx[index]
        #-----------------------------------------------------------------
        ap=3*koef[0]
        bp=2*koef[1]+mup*ap
        cp=koef[3]
        polpar = [mup,ap,bp,cp]
        [mu,a,b,c], covar = curve_fit(p3, tmx, tmy,polpar)
        koren_vyb = mu
        hod_koren_vyb=p3(mu,mu,a,b,c)
        hodnoty_fit=p3(tmx,mu,a,b,c)
        koren_chyba1=covar[0,0]**(0.5)
        #terka-carlo
        #-----------------------------------------------------------------
        par_mu=np.zeros([100],float)
        par_y = np.zeros([100],float)
        for j in range(100):
            noise=np.random.normal(loc=0,scale=1.0/(2.355*sn),size=len(tmy))
            tmy_noise=tmy+noise
            [mu,a,b,c], covar = curve_fit(p3, tmx, tmy_noise,polpar)
            par_mu[j]=mu
            par_y[j]=p3(mu,mu,a,b,c)
#          print koren_vyb, min(par_mu), max(par_mu)
        koren_chyba=(koren_chyba1**2+(max(par_mu)-min(par_mu))**2)**(0.5)
        #-----------------------------------------------------------------

        print '#################################################'
        print 'extreme position:', koren_vyb, 'error:',
        koren_chyba, 'error_FIT:', koren_chyba1
        print '#################################################'
        #the third round of fitting
        plot(tmx,p3(tmx,mu,a,b,c),'p-')
        mu=0
        [mu,a,b,c],covar=curve_fit(p3,tmx-koren_vyb,tmy)
        hod_chyba1=covar[3,3]**(0.5)
        hod_koren_chyba = sqrt(covar[3,3]+(max(par_y)-min(par_y))**2)
        print '#################################################'
        print 'extr. position value:', hod_koren_vyb, 'error:',
         hod_koren_chyba, 'error_FIT:', hod_chyba1
        print '#################################################'
        print covar
        #-----------------------------------------------------------------
        nhodnot=len(tmy)
        cnt=0
#          v,w=linalg.eig(covar)
#           print covar
#           print v
#           print mu,a,b,c
        pylab.axvline(koren_vyb, c='green', label='extrem')
        pylab.axvline(koren_vyb+koren_chyba, c='green', label='extrem')
        pylab.axvline(koren_vyb-koren_chyba, c='green', label='extrem')
        p = plt.axvspan(koren_vyb-koren_chyba,koren_vyb+koren_chyba,
        facecolor='green', alpha=0.5)
        draw()
        print 'write l,m, or r for Halpha, c,v for Si II and e for He I'

    elif (event.key=='d'):
        tmsk=np.ma.masked_inside(x,np.min(xmeze),np.max(xmeze))
        pocn=len(x)-np.ma.count(tmsk)
        tmx=np.zeros([pocn],float)
```

```
        tmy=np.zeros([pocn],float)
        nhodnot=len(tmy)
        cnt=0
        for j in range(len(x)):
            if (tmsk.mask[j]==True):
                tmx[cnt]=x[j]
                tmy[cnt]=y[j]
                cnt+=1
#-------------------------------------------------------------------------------
        nmax=2
        p=np.polyfit(tmx,tmy,nmax)
        koef=[]
        koef=p
        print 'koef:',koef
        ft=np.poly1d(p)
        ftdat=ft(tmx)
        #plot(tmx,ftdat,'b--')
        mups=tmx[int(len(tmx)/2.0)] #extreme position guess
        if (tmy[0] < tmy[int(len(tmx)/2.0)]):
            for index, item in enumerate(tmy):
                    if (item == max(tmy)):
                        mup=tmx[index]
        if (tmy[0] > tmy[int(len(tmx)/2.0)]):
            for index, item in enumerate(tmy):
                        mup=tmx[index]
        #------------------------------------------------------------------
        ap=2*koef[0]
        bp=koef[2]
        polpar = [mup,ap,bp]
        [mu,a,b], covar = curve_fit(p2, tmx, tmy,polpar)
        print 'mu,a,b,covar:',mu,a,b,covar
        koren_vyb = mu
        hod_koren_vyb=p2(mu,mu,a,b)
        hodnoty_fit=p2(tmx,mu,a,b)
        koren_chyba1=covar[0,0]**(0.5)
        #terka-carlo
        #------------------------------------------------------------
        par_mu=np.zeros([100],float)
        par_y = np.zeros([100],float)
        for j in range(100):
            noise=np.random.normal(loc=0,scale=1.0/(2.355*sn),size=len(tmy))
            tmy_noise=tmy+noise
            [mu,a,b], covar = curve_fit(p2, tmx, tmy_noise,polpar)
            par_mu[j]=mu
            par_y[j]=p2(mu,mu,a,b)
#          print koren_vyb, min(par_mu), max(par_mu)
        koren_chyba=(koren_chyba1**2+(max(par_mu)-min(par_mu))**2)**(0.5)
        #------------------------------------------------------------

        print '#############################################'
        print 'extreme position:', koren_vyb, 'error:',
        koren_chyba, 'error_FIT:', koren_chyba1
        print '#############################################'
        #the third round of fitting
        plot(tmx,p2(tmx,mu,a,b),'p-')
        mu=0
        [mu,a,b],covar=curve_fit(p2,tmx-koren_vyb,tmy)
        hod_chyba1=covar[2,2]**(0.5)
        hod_koren_chyba = sqrt(covar[2,2]+(max(par_y)-min(par_y))**2)
        print '#############################################'
        print 'extr. position value:', hod_koren_vyb, 'error:',
```

```
        hod_koren_chyba, 'error_FIT:', hod_chyba1
        print '#############################################'
        print covar
        #-----------------------------------------------------------------
        nhodnot=len(tmy)
        cnt=0
#        v,w=linalg.eig(covar)
#        print covar
#        print v
#        print mu,a,b
        pylab.axvline(koren_vyb, c='green', label='extrem')
        pylab.axvline(koren_vyb+koren_chyba, c='green', label='extrem')
        pylab.axvline(koren_vyb-koren_chyba, c='green', label='extrem')
        p = plt.axvspan(koren_vyb-koren_chyba,koren_vyb+
        koren_chyba, facecolor='green', alpha=0.5)
        draw()
        print 'write l,m, or r for Halpha, c,v for Si II and e for He I'


    elif (event.key=='j'):
        tmsk=np.ma.masked_inside(x,np.min(xmeze),np.max(xmeze))
        pocn=len(x)-np.ma.count(tmsk)
        tmx=np.zeros([pocn],float)
        tmy=np.zeros([pocn],float)
        nhodnot=len(tmy)
        cnt=0
        for j in range(len(x)):
            if (tmsk.mask[j]==True):
                tmx[cnt]=x[j]
                tmy[cnt]=y[j]
                cnt+=1
#-----------------------------------------------------------------------------
        nmax=4
        p=np.polyfit(tmx,tmy,nmax)
        koef=[]
        koef=p
        print koef
        ft=np.poly1d(p)
        ftdat=ft(tmx)
        #plot(tmx,ftdat,'b--')
        mups=tmx[int(len(tmx)/2.0)] #extreme position guess
        if (tmy[0] < tmy[int(len(tmx)/2.0)]):
            for index, item in enumerate(tmy):
                    if (item == max(tmy)):
                        mup=tmx[index]
        if (tmy[0] > tmy[int(len(tmx)/2.0)]):
            for index, item in enumerate(tmy):
                        mup=tmx[index]
        #-----------------------------------------------------------------
        ap=4*koef[0]
        bp=3*koef[1]+mup*ap
        cp=-koef[3]/mup
        dp=koef[4]
        polpar = [mup,ap,bp,cp,dp]
        [mu,a,b,c,d], covar = curve_fit(p4, tmx, tmy,polpar)
        koren_vyb = mu
        hod_koren_vyb=p4(mu,mu,a,b,c,d)
        hodnoty_fit=p4(tmx,mu,a,b,c,d)
        koren_chyba1=covar[0,0]**(0.5)
        #terka-carlo
        #-----------------------------------------------------------------
```

```python
    par_mu=np.zeros([100],float)
    par_y = np.zeros([100],float)
    for j in range(100):
        noise=np.random.normal(loc=0,scale=1.0/(2.355*sn),size=len(tmy))
        tmy_noise=tmy+noise
        [mu,a,b,c,d], covar = curve_fit(p4, tmx, tmy_noise,polpar)
        par_mu[j]=mu
        par_y[j]=p4(mu,mu,a,b,c,d)
    print koren_vyb, min(par_mu), max(par_mu)
    koren_chyba=(koren_chyba1**2+(max(par_mu)-min(par_mu))**2)**(0.5)
    #-------------------------------------------------------------

    print '################################################'
    print 'extreme position:', koren_vyb, 'error:',
    koren_chyba, 'error_FIT:', koren_chyba1
    print '################################################'
    #the third round of fitting
    plot(tmx,p4(tmx,mu,a,b,c,d),'p-',c='blue')
    mu=0
    [mu,a,b,c,d],covar=curve_fit(p4,tmx-koren_vyb,tmy)
    hod_koren_chyba = sqrt(covar[4,4]+(max(par_y)-min(par_y))**2)
    hod_chyba1=covar[4,4]**(0.5)
    print '################################################'
    print 'extr. position value:', hod_koren_vyb, 'error:',
     hod_koren_chyba, 'error_FIT:', hod_chyba1
    print '################################################'
    #--------------------------------------------------------------
    nhodnot=len(tmy)
    print covar
    cnt=0
#       v,w=linalg.eig(covar)
#       print covar
#       print v
#       print mu,a,b,c,d
    pylab.axvline(koren_vyb, c='blue', label='extrem')
    pylab.axvline(koren_vyb+koren_chyba, c='blue', label='extrem')
    pylab.axvline(koren_vyb-koren_chyba, c='blue', label='extrem')
    p = plt.axvspan(koren_vyb-koren_chyba,koren_vyb+
    koren_chyba, facecolor='blue', alpha=0.5)
    draw()
    print 'write l,m, or r for Halpha, c,v for Si II and e for He I'

elif (event.key=='l'):
    lam_l = (koren_vyb-6562.79)*299792.458/6562.79
    er_lam_l = koren_chyba*299792.458/6562.79
    f_l = hod_koren_vyb
    er_f_l = hod_koren_chyba
    print lam_l, er_lam_l, f_l,er_f_l
elif (event.key=='m'):
    lam_m = (koren_vyb-6562.79)*299792.458/6562.79
    er_lam_m = koren_chyba*299792.458/6562.79
    f_m = hod_koren_vyb
    er_f_m = hod_koren_chyba
    print lam_m, er_lam_m, f_m, er_f_m
elif (event.key=='r'):
    lam_r = (koren_vyb-6562.79)*299792.458/6562.79
    er_lam_r = koren_chyba*299792.458/6562.79
    f_r = hod_koren_vyb
    er_f_r = hod_koren_chyba
    print lam_r, er_lam_r, f_r, er_f_r
elif (event.key=='c'):
```

```
        lam_s1 = (koren_vyb-6347.10)*299792.458/6347.10
        er_lam_s1 = koren_chyba*299792.458/6347.10
        f_s1 = hod_koren_vyb
        er_f_s1 = hod_koren_chyba
        print lam_s1, er_lam_s1, f_s1,er_f_s1
      elif (event.key=='v'):
        lam_s2 = (koren_vyb-6371.36)*299792.458/6371.36
        er_lam_s2 = koren_chyba*299792.458/6371.36
        f_s2 = hod_koren_vyb
        er_f_s2 = hod_koren_chyba
        print lam_s2, er_lam_s2,f_s2,er_f_s2
      elif (event.key=='e'):
        lam_h = (koren_vyb-6679.676834)*299792.458/6679.676834
        er_lam_h = koren_chyba*299792.458/6679.676834
        f_h = hod_koren_vyb
        er_f_h = hod_koren_chyba
        print lam_h, er_lam_h, f_h, er_f_h
#------------------------------------------------------------------------
#close#==================================================================
#------------------------------------------------------------------------
      elif (event.key=='k'):
          close()
#======================================================
#======================================================
def zoomp(event):
    global xmeze
    tb = get_current_fig_manager().toolbar
    if event.button==1 and event.inaxes and tb.mode == 'zoom rect':
      xmeze[0] = event.xdata
#======================================================
def zoomr(event):
    global xmeze
    tb = get_current_fig_manager().toolbar
    if event.button==1 and event.inaxes and tb.mode == 'zoom rect':
      xmeze[1] = event.xdata
      print "zooomX = ",xmeze
#======================================================
####################################################################
# zadefinovani funkce pro fit
def f(x, height, mu, sigma, const):
      return height * exp(-((x-mu )/ sigma )**2) + const
def pol5(x,q,w,c,d,e,f):
       return q*x**5+w*x**4+c*x**3+d*x**2+e*x+f
def p5(x, mu,a,b,c,d,e):
      return (a/5.0)*x**5+((b-mu*a)/4.0)*x**4+((c-mu*b)/3.0)*x**3+
      ((d-mu*c)/2.0)*x**2-mu*d*x+e
def p3(x,mu,a,b,c):
      return (a/3)*x**3+((b-mu*a)/2)*x**2-mu*b*x+c
def p4(x,mu,a,b,c,d):
      return (a/4)*x**4+((b-mu*a)/3)*x**3+((c-mu*b)/2)*x**2-mu*c*x+d
def lin(x,a,b):
      return a*x +b
def p2(x,mu,a,b):
      return (a/2)*x**2-mu*a*x+b
####################################################################
# nacteni souboru se jmeny
def getfile(filename,results):
    f = open(filename)
    filecontents = f.readlines()
    for line in filecontents:
        foo = line.strip('\n')
```

```
        results.append(foo)
    return results
################################################################
#=======================================================
#inicialization
sn = 1
chyba_rv_a=1
chyba_rv_b=1
chyba_ew_a=1
chyba_ew_b=1
ew_a=1
ew_b=1
rv_a=1
rv_b=1
ymax_a=1
ymax_b=1
xmax_a=1
xmax_b=1
chybah_a=1
chybah_b=1
lam_l=1
er_lam_l=1
f_l=1
er_f_l=1
lam_m=1
er_lam_m=1
f_m=1
er_f_m=1
lam_r=1
er_lam_r=1
f_r=1
er_f_r=1
koren_vyb=1
hod_koren_vyb=1
hod_koren_chyba=1
koren_chyba=1
lam_s1=1
er_lam_s1=1
f_s1=1
er_f_s1=1
lam_s2=1
er_lam_s2=1
f_s2=1
er_f_s2=1
lam_h=1
er_lam_h=1
f_h=1
er_f_h=1
#=======================================================
radky=[]
getfile('spektra', radky)
data = []
s2 = open('OII', 'w')
s3 = open('Halpha', 'w')
s4 = open('SiII', 'w')
s5 = open('HeI', 'w')
s6 = open('sn', 'w')
t=-1
for radek in radky:
    t=t+1
    if (t==0):
```

```
            s2.write('#')
            s2.write('\t')
            s2.write('\t')
            s2.write('EW_6300')
            s2.write('\t')
            s2.write('EW_ER_6300')
            s2.write('\t')
            s2.write('F_6300')
            s2.write('\t')
            s2.write('F_ER_6300')
            s2.write('\t')
            s2.write('RV_6300')
            s2.write('\t')
            s2.write('RV_ER_6300')
            s2.write('\t')
            s2.write('EW_6364')
            s2.write('\t')
            s2.write('EW_ER_6364')
            s2.write('\t')
            s2.write('F_6364')
            s2.write('\t')
            s2.write('F_ER_6364')
            s2.write('\t')
            s2.write('RV_6364')
            s2.write('\t')
            s2.write('RV_ER_6364')
            s2.write('\n')
            s2.write('\n')
            s2.write('\n')
            s3.write('#')
            s3.write('\t')
            s3.write('RV_V')
            s3.write('\t')
            s3.write('RV_ER_V')
            s3.write('\t')
            s3.write('F_V')
            s3.write('\t')
            s3.write('F_ER_V')
            s3.write('\t')
            s3.write('RV_CD')
            s3.write('\t')
            s3.write('RV_ER_CD')
            s3.write('\t')
            s3.write('F_CD')
            s3.write('\t')
            s3.write('F_ER_CD')
            s3.write('\t')
            s3.write('RV_R')
            s3.write('\t')
            s3.write('RV_ER_R')
            s3.write('\t')
            s3.write('F_R')
            s3.write('\t')
            s3.write('F_ER_R')
            s3.write('\n')
            s3.write('\n')
    f2= open(radek, 'r')
    print radek
    for j in f2:
        if (j):
            tm=j.strip().split()
```

```
              data.append([float(tm[0]),float(tm[1])])
        f2.close()
        f2= open(radek, 'r')
        lines = f2.readlines()
        f2.close()
        ndata=len(data)
#======================================================
        x=np.zeros([ndata],float)
        y=np.zeros([ndata],float)
        for j in range(ndata):
           [x[j],y[j]]=data[j]
        xmeze=[np.min(x),np.max(x)]
        maxkor=[]
#======================================================
        x1 = []
        y1 = []
        data = []
        for line in lines:
              p = line.split()
              x1.append(float(p[0]))
              y1.append(float(p[1]))
####################################################################
        connect('button_press_event',zoomp)
        connect('button_release_event',zoomr)
        connect('key_press_event',pkey)
        show()
        raw_input("Press ENTER")
        s6.write(str(sn))
        s6.write('\n')
        s2.write(str(abs(ew_a)))
        s2.write('\t')
        s2.write(str(abs(chyba_ew_a)))
        s2.write('\t')
        s2.write(str(abs(ymax_a)))
        s2.write('\t')
        s2.write(str(abs(chybah_a)))
        s2.write('\t')
        s2.write(str(rv_a))
        s2.write('\t')
        s2.write(str(abs(chyba_rv_a)))
        s2.write('\t')
        s2.write(str(abs(ew_b)))
        s2.write('\t')
        s2.write(str(abs(chyba_ew_b)))
        s2.write('\t')
        s2.write(str(abs(ymax_b)))
        s2.write('\t')
        s2.write(str(abs(chybah_b)))
        s2.write('\t')
        s2.write(str(rv_b))
        s2.write('\t')
        s2.write(str(abs(chyba_rv_b)))
        s2.write('\n')
################################
        s3.write(str(lam_l))
        s3.write('\t')
        s3.write(str(er_lam_l))
        s3.write('\t')
        s3.write(str(f_l))
        s3.write('\t')
        s3.write(str(er_f_l))
```

```
      s3.write('\t')
      s3.write(str(lam_m))
      s3.write('\t')
      s3.write(str(er_lam_m))
      s3.write('\t')
      s3.write(str(f_m))
      s3.write('\t')
      s3.write(str(er_f_m))
      s3.write('\t')
      s3.write(str(lam_r))
      s3.write('\t')
      s3.write(str(er_lam_r))
      s3.write('\t')
      s3.write(str(f_r))
      s3.write('\t')
      s3.write(str(er_f_r))
      s3.write('\n')
################################
      s4.write(str(lam_s1))
      s4.write('\t')
      s4.write(str(er_lam_s1))
      s4.write('\t')
      s4.write(str(f_s1))
      s3.write('\t')
      s4.write(str(er_f_s1))
      s4.write('\t')
      s4.write(str(lam_s2))
      s4.write('\t')
      s4.write(str(er_lam_s2))
      s4.write('\t')
      s4.write(str(f_s2))
      s4.write('\t')
      s4.write(str(er_f_s2))
      s4.write('\n')
################################
      s5.write(str(lam_h))
      s5.write('\t')
      s5.write(str(er_lam_h))
      s5.write('\t')
      s5.write(str(f_h))
      s5.write('\t')
      s5.write(str(er_f_h))
      s5.write('\n')
      clf()
```

B.4   EW.m

The octave routine called EW.m has been used for the calculation of the Equivalent width for the Si II lines present in the Ondřejov spectra.

```
clear
#spocita ekvivalentni sirky lichobeznikovou metodou, chyby podle Vollman & Eversberg,
#jako hranicni bere prvni bod za hranici intervalu
# calculates equivalent widths by trapezium method, errors are after Vollman & Eversberg,
# boundary point is the first point behind the boundary of the interval
signalnoise='signalnoise43'; #list of signal to noise ratio
soubor='list43'; # list of incoming files (ASCII spekter)
dseznam='jd43';  # list of corresponding Julian dates-2450000
kontinuum='kont';  # file with the continuum intervals in the form of matrix  (n,2);
        #      not fundamental, could be done interactively
         #       first column = beginnings of intervals; second column = ends of intervals


aw=2.0;  # width of weight function


fid=fopen(soubor,'r');


d=0;
do
    soub=fgetl(fid);
    d=d+1;
until  soub==-1

fclose(fid);
d=d-1;

fid=fopen(soubor,'r');

sw=1.81280495411095;  # norm constant for  weight function
ekviv=zeros(1,3);

JD=load(dseznam);
kont=load(kontinuum);
S_N=load(signalnoise);

do
   #lambda1=input('wavelength for continuum fitting from: ');
   #lambda2=input('                                        to: ');    # do
    lambda1=6350;
    lambda2=6390;
until lambda1<lambda2

do
   #mez1=input('integration from: ');   # integrace od
   #mez2=input('              to: '); # do
    mez1=6365;
    mez2=6380;
until mez1<mez2

do
   hodnota=input('Take into account flux of  all values or >1, or  <1 ? (v/k/z): ','s');
until (hodnota=='v')|(hodnota=='k')|(hodnota=='z')

#vybrani useku k prolozeni kontinua
n=size(kont);

m=1; kz=0;
```

```
for k=1:n(1)

if (kont(k,1)>lambda1)&(kont(k,2)<lambda2)
    kon(m,:)=kont(k,:); m=m+1;
elseif (kont(k,1)<lambda1)&(kont(k,2)<lambda2)&(kont(k,2)>lambda1)
    kon(m,1)=lambda1; kon(m,2)=kont(k,2); m=m+1;
elseif (kont(k,1)>lambda1)&(kont(k,1)<lambda2)&(kont(k,2)>lambda2)
    kon(m,2)=lambda2; kon(m,1)=kont(k,1); m=m+1;
else
    kon(m,1)=lambda1; kon(m,2)=lambda2;
endif

endfor
n1=size(kon);
nn=zeros(n1);

for k=1:d

soub=fgetl(fid)
mat=load(soub);

l1=0;
for k1=1:n1(1)

    do l1=l1+1;
    until ((mat(l1,1))>=(kon(k1,1)))

    nn(k1,1)=l1;

    do l1=l1+1;
    until mat(l1,1)>kon(k1,2)

    nn(k1,2)=l1-1;

endfor

prokl=mat(nn(1,1):nn(1,2),:);

for k1=2:n1(1)

    prokl=[prokl;mat(nn(k1,1):nn(k1,2),:)];

endfor

#prolozeni kontinua
np=size(prokl);
N=np(1);

x=prokl(:,1); y=prokl(:,2);
X=sum(x); Y=sum(y); XY=x'*y; XX=x'*x;

a0=(Y*XX-X*XY)/(N*XX-X^2);
a1=(X*Y-N*XY)/(X^2-N*XX);
yp=a0+a1*x; dy=yp-y; dy=dy.*dy;
sigma1=sqrt(sum(dy)/(N-2));
nr=N;

do
    sigma=sigma1;
    w=1/(nr*sw*aw*sigma)*exp(-(dy/(aw*sigma)).^4); W=sum(w);
    nr=N*W;
```

```
    X=x'*w; Y=y'*w; XY=x.*y; XY=XY'*w; XX=x.*x; XX=XX'*w;
    a0=(Y*XX-X*XY)/(W*XX-X^2);
    a1=(X*Y-W*XY)/(X^2-W*XX);
    yp=a0+a1*x; dy=yp-y; dy=dy.*dy;
    sigma1=sqrt((dy'*w)/(W*(N-2)));

until abs(sigma1-sigma)<0.000001

#urceni pomeru S/N
RMS=sqrt((dy'*w)/W);
signal=mean(yp);
#SN=signal/RMS
SN=S_N(k)

W=max(w);
w=w/W;

plot(x,y,'-',x,yp,'-')
pause

#integrace ekvivalentnich sirek
do
zz2=[mez1;mez1];
zz3=[mez2;mez2];

EW=0;
l1=0;
presah=(mez2-mez1)/5;
do l1=l1+1;
until mat(l1,1)>=(mez1-presah)
mm1=l1;
do l1=l1+1;
until mat(l1,1)>=mez1
m1=l1;
do l1=l1+1;
until mat(l1,1)>=mez2
m2=l1-1;
do l1=l1+1;
until mat(l1,1)>=(mez2+presah)
mm2=l1-1;

obr=mat(mm1:mm2,:);
int=mat(m1:m2,:);
zz1=[min(obr(:,2));max(obr(:,2))];
l1=m2-m1;
mFlux=mean(int(:,2));
int(:,2)=int(:,2)-(a0+a1*int(:,1));

dlambda=int(l1+1,1)-int(1,1);

plot(obr(:,1),obr(:,2),'g-',obr(:,1),obr(:,2),'rx',zz2,zz1,'b-',zz3,zz1,'b-')
pause
do
    an=input('Change the boundary of intervals? Press a for yes, n for no. (a/n) or omit (v): ','s');
    # Zmenit meze intervalu? (a/n) ci vynechat (v)
#until (an=='v')|(an=='a')|(an=='n')|(an=='V')|(an=='A')|(an=='N')

if (an=='a')|(an=='A')
    mez1=input('integration from: ');  # integrace od:
    mez2=input('                to: ');  # do
endif
```

```
until (an=='v')|(an=='n')|(an=='V')|(an=='N')

if (an!='v')&(an!='V')

if hodnota=="k"
   for k1=1:l1
       if (int(k1,2)>=0)&(int(k1+1,2)>=0)
          EW=EW+(int(k1+1,1)-int(k1,1))*(int(k1,2)+int(k1+1,2))/2;
       endif

       if (int(k1,2)>0)&(int(k1+1,2)<0)
          EW=EW+(-int(k1,2)*(int(k1,1)-int(k1+1,1))/(int(k1,2)-int(k1+1,2)))*int(k1,2)/2;
       endif

       if (int(k1,2)<0)&(int(k1+1,2)>0)
          EW=EW+(int(k1+1,1)-int(k1,1)+int(k1,2)*(int(k1,1)-int(k1+1,1))
          /(int(k1,2)-int(k1+1,2)))*int(k1+1,2)/2;
       endif
endfor

elseif hodnota=="v"
   for k1=1:l1
       EW=EW+(int(k1+1,1)-int(k1,1))*(int(k1,2)+int(k1+1,2))/2;
   endfor

elseif hodnota=="z"
       for k1=1:l1
       if (int(k1,2)<=0)&(int(k1+1,2)<=0)
          EW=EW+(int(k1+1,1)-int(k1,1))*(int(k1,2)+int(k1+1,2))/2;
       endif

       if (int(k1,2)<0)&(int(k1+1,2)>0)
          EW=EW+(-int(k1,2)*(int(k1,1)-int(k1+1,1))/(int(k1,2)-int(k1+1,2)))*
          *int(k1,2)/2;
       endif

       if (int(k1,2)>0)&(int(k1+1,2)<0)
          EW=EW+(int(k1+1,1)-int(k1,1)+int(k1,2)*(int(k1,1)-int(k1+1,1))\
          /(int(k1,2)-int(k1+1,2)))*int(k1+1,2)/2;
       endif
       endfor
endif

dis=sqrt(1+signal/mFlux)*(dlambda+EW)/S_N(k);
ekviv((k-kz),1)=JD(k); ekviv((k-kz),2)=-EW; ekviv((k-kz),3)=dis;
endif

endfor

fclose(fid);

#ulozeni vysledku
x=ekviv(:,1); y=ekviv(:,2); err=ekviv(:,3);
axis();
errorbar(x,y,err)

save sirka 'ekviv'
disp('the result is saved into the file sirka')    # vysledek ulozen do souboru sirka
```

Acknowledgements